**UNIVERSITY OF SOUTHAMPTON**

FACULTY OF PHYSICAL SCIENCES AND ENGINEERING

Optoelectronics Research Centre

# Novel approaches in manipulating, guiding, and generating THz and sub-THz fields

**Anagnostis Tsiatmas**

Thesis for the degree of Doctor of Philosophy

September 2013

UNIVERSITY OF SOUTHAMPTON

# ABSTRACT

FACULTY OF PHYSICAL SCIENCES AND ENGINEERING

OPTOELECTRONICS RESEARCH CENTRE

Doctor of Philosophy

## NOVEL APPROACHES IN MANIPULATING, GUIDING, AND GENERATING THz AND SUB-THz FIELDS

by Anagnostis Tsiatmas

This thesis serves to address the main challenges of the terahertz technology, providing new efficient ways of actively manipulating, guiding, and generating THz and sub-THz fields. This is accomplished by taking a truly interdisciplinary approach and exploiting the physics of superconductors, and the electrodynamics of metamaterial and plasmonic structures. Metamaterial arrays made of superconducting films are suggested for manipulating the THz radiations, while superconducting plasmonic waveguides are considered for achieving efficient propagation of THz waves. In addition, metamaterial arrays composed of bimetallic rings that exhibit both plasmonic and thermoelectric properties are investigated as a possible new source of THz radiation and strong magnetic fields.

I have demonstrated experimentally, for the first time, that high- and low-critical temperature superconducting metamaterials are able to show sub-radiant resonances of Fano type that can be controlled with temperature. Such metamaterial resonances show vanishing radiation losses, while superconductors have very low Ohmic losses. Thus, these structures offer an efficient way to actively manipulate sub-THz (and THz) fields.

I have reported on the first experimental realisation of the extraordinary transmission effect in periodically perforated superconducting films. I have shown that the level of transmission of sub-THz waves through these structures could be controlled with temperature near the superconducting transition point. The latter enabled to identify the role of the plasmonic excitations in the mechanism of extraordinary transmission.

I have shown that superconductors below their gap-frequency ($\sim$ several THz for high-temperature superconductors) are similar in behaviour to plasmonic metals at optical frequencies. Geometries of superconducting structures have been identified that support almost dispersionless propagation of plasmonic-like modes with frequencies up to several THz, exhibiting both extreme localisation and very low propagation losses.

Finally, I have theoretically demonstrated that metamaterial arrays composed of bimetallic gold-nickel nanorings, when illuminated by ultrafast optical pulses, support transient thermoelectric currents that lead to the generation of magnetic pulses of sub-picosecond duration, nanoscale localisation and peak amplitudes of the order of one Tesla. These results could facilitate the study of ultrafast nanoscale magnetic phenomena and have potential use in such applications as material characterisation and magnetic recording.

# Contents

# List of Figures

## DECLARATION OF AUTHORSHIP

I, Anagnostis Tsiatmas, declare that the thesis entitled "Novel approaches in manipulating, guiding, and generating THz and sub-THz fields" and the work presented in the thesis are both my own, and have been generated by me as the result of my own original research. I confirm that:

- this work was done wholly or mainly while in candidature for a research degree at this University;
- where any part of this thesis has previously been submitted for a degree or any other qualification at this University or any other institution, this has been clearly stated;
- where I have consulted the published work of others, this is always clearly attributed;
- where I have quoted from the work of others, the source is always given. With the exception of such quotations, this thesis is entirely my own work;
- I have acknowledged all main sources of help;
- where the thesis is based on work done by myself jointly with others, I have made clear exactly what was done by others and what I have contributed myself;
- parts of this work have been published as the journal papers and conference contributions listed in Appendix B.

Signed: _____

Date: _____

# Acknowledgements

"Give me a place to stand on, and I can move the earth" Archimedes said in 280 B.C. In our times this 'place', I believe, is education. Nothing is impossible for our society to accomplish, provided that we invest in the education of all its members. But education goes beyond technical knowledge, 'education' is more related to critical thinking, thorough examination of the facts, and reporting of the truth. It is the role of the teacher to educate the student and inculcate in him or her the patience that is necessary to understand reality. It is the mission of the teacher to provide the inspiration and guidance that will enable the transformation of the fragile ideas of the young researcher into solid visions, to feed the young researcher with motivation and love for science.

Personally, I consider myself very lucky to have been guided and supervised by Prof. Nikolay Zheludev, who not only gave me the opportunity to work on the fascinating field of metamaterials and plasmonics, but made me also aware of how cutting-edge research is usually conducted in this discipline. Without this knowledge it would have been difficult for me to realise that this was not my dream, and I should have pursued a path closer to my beliefs. For this reason, I am grateful to him.

I would like to warmly thank Dr. Vassili Fedotov, my second supervisor, who showed me how intriguing novel research is, and who had always the time to discuss with me and help me address the problems encountered throughout my research. Actually, without him it seems to me, now, that this thesis would never have been written.

In addition, it would be an omission not to thank Prof. Javier Garcia de Abajo

for all our theoretical discussions and his contributions in the research topics reported in this thesis. A big thanks goes also to Dr. Nikitas Papasimakis, for all the fruitful (scientific and not) discussions. I consider myself very lucky to have met with him.

I would also like to thank all the people that have helped with the experiments, and particularly J. Y. Ou (Bruce), for helping me with all the issues concerning the fabrication of superconducting samples, and spoiling me with the best coffee; Dr. Roger Buckingham for introducing me into the theory of superconductivity; Vassili Savinov for both the joyful and inspirational discussions and all his help. A thanks goes also to the other members of the group for the discussions and the great time together inside and outside the labs.

More importantly, I'm indebted to my mother, sister, and father for all their sacrifices. Just thanking them for their efforts and love all these years seems so insufficient. Last but not least, I am grateful to my girlfriend Zoe, who has not only managed to keep up with my constant whimpering and bad temper while I was writing this thesis, but also provided me with inspiration the moments I needed it the most.

Now at last, I feel relieved that this part of my life is over. Sorry from all those of you (and especially my friends) that you had to keep up with me constantly talking about this thesis.

Anagnostis Tsiatmas

The Netherlands, May 2013

# 1 Introduction

## 1.1 The THz Radiation

In our recent technological history there has been no other achievement contributing so greatly to all aspects of our daily life than gaining control of and exploiting the electromagnetic radiation. The importance of electromagnetic radiation is evident given the plethora of applications, ranging from the generation and the distribution of power at frequencies as low as few tens of Hz to medical diagnostics and therapy beyond $3x10^{16}$Hz using X- and gamma rays, with the bulk of the electromagnetic spectrum exploited most notably for information transfer, communications, imaging, and sensing. In Fig. 1.1 an artistic illustration of several electromagnetic spectral regions of scientific and technological interest together with examples of possible applications at these frequencies is given.

Intriguingly, the spectral band between the microwave and optical frequencies, known as the terahertz radiation, still remains scientifically and technologically mostly unexploited. Following the most common convention, the terahertz band is defined as the range of frequencies from 0.3 to 10THz, while the frequency range from 0.075 to 0.3THz corresponds to sub-THz radiation or millimetre waves [1]. For the sake of brevity, in this thesis, the term "terahertz" (or "THz" for short) will refer to the spectral range from 0.075 to 10THz, unless otherwise specified.

Terahertz radiation has a number of uniquely attractive qualities. Initially, THz radiation is non-ionizing, meaning its photons are not energetic enough to knock electrons off atoms and molecules in human tissues; an effect that could trigger harmful

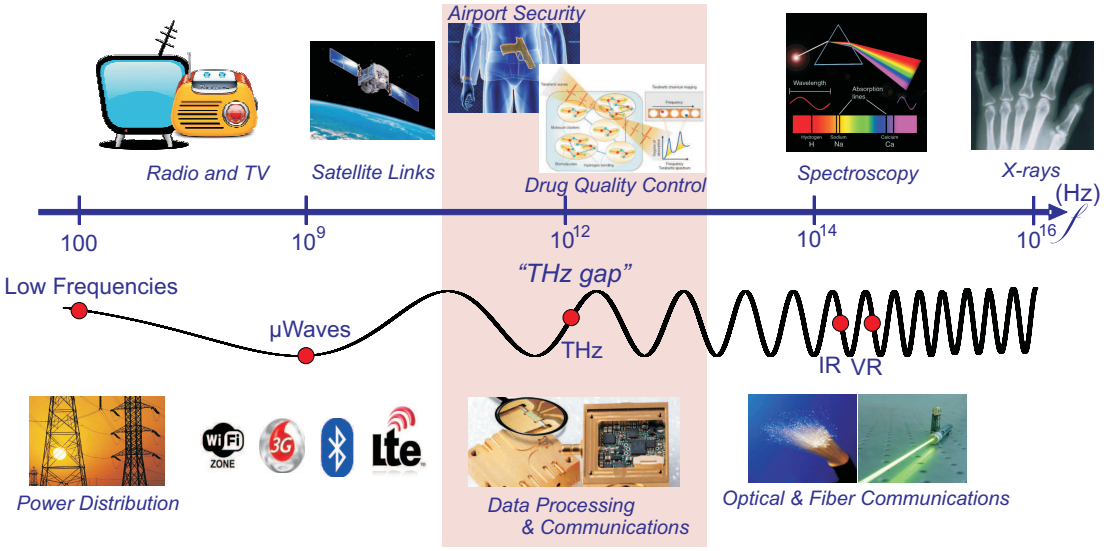


**Figure 1.1:** *An artistic illustration of the electromagnetic spectrum. Several spectral regions of scientific and technological interest are illustrated together with examples of possible applications at these frequencies.*

chemical reactions if it happened. On the other hand, the photons of these frequencies lie in crucial energetic and time scales for performing spectroscopy and can be used in studies of condensed matter physics and nanoscale structures [2]. Such a property is of immediate use in the detection of illegal or lethal substances (e.g., anthrax). Furthermore, at these wavelengths radiation can pass through many objects that are opaque to optical waves as well as yield extremely high-resolution images compared to microwave radiation [3]. Such a feature is very desirable for baggage inspection in airports [4, 5], or drug quality testing, e.g., checking the width of a pill coating to ensure that the drug will reach the desired target before it is dissolved [4]. But most importantly, THz waves can act as communication carriers able to offer much larger modulation bandwidths compared to the microwaves. In this sense, THz waves can lead to the enhancement of the information capacity provided in data processing and transmission systems operating at these frequencies.

Traditionally, THz radiation has been exploited by astronomers for investigating the chemical composition of the interstellar media and planetary atmospheres using earth-based and spacestation-based remote sensing. Given that 98 percent of the photons released after the Big Bang reside in the spectral range from microwaves to far-infrared frequencies, THz spectroscopy seems an essential tool for observing and studying the

early Universe [3]. However, systems sensing terahertz radiation for scientific purposes differ significantly from most other applications that generation, propagation, and control of THz waves is necessary. Especially generation of THz radiation is hard, since common electronic sources perform inefficiently above a few hundred GHz, while conventional laser sources are not available at the THz band, due to the unavailability of suitable semiconductors [6]. In addition, most of today's sources are very power inefficient, lacking tunability and portability, and are rather specialized for a specific application [3]. Another challenge in the exploitation of the THz is related to their high atmospheric path losses, since many particles absorb, refract, and scatter terahertz radiation, rendering these waves improper for long-range free-space applications [6]. Meanwhile, efficient waveguiding of THz is very desired for many of the applications presented above, such as imaging, sensing, and data processing. Although efforts for efficient waveguiding have been presented [7, 8], simultaneous efficient and dispersionless propagation remains a challenge. Finally, the size of the devices operating in the THz domain is crucial. In this aspect, THz devices resemble their photonic counterparts and require for their operation structures with physical dimensions comparable in size to their wavelength. This is attributed to the diffraction limitation of THz fields [9].

This thesis serves to address the main challenges of the terahertz technology, providing new efficient ways of actively manipulating, guiding, and generating THz fields. That has become possible to achieve by adopting a truly interdisciplinary approach, which exploited the exotic electrodynamics of metamaterials and the intriguing physics of superconductors coupled with plasmonic and thermoelectric phenomena in nanostructures.

Since both metamaterials and plasmonics are relatively new fields of research, the rest of the chapter will act as a brief introduction to these fields, explaining their relevance and importance to the subject of this thesis and providing a superficial overview of the existing approaches to handling and generating terahertz fields. In particular, Section 1.3 covers the manipulation of THz radiation and introduces the notion of metamaterials, Section 1.4 deals with the guiding of THz radiation and introduces the field of plasmonics, while Section 1.5 is dedicated to the sources of THz radiation. The chapter concludes with Section 1.6, which contains a brief outline of the rest of the thesis.

## 1.2 Manipulating THz Radiation

The lack of natural materials that can interact efficiently with magnetic or electric fields of THz waves substantially hinders the adoption of this frequency range for scientific investigation and practical applications. The range of devices required for the manipulation of the THz radiation includes modulators, filters, absorbers, beam splitters, polarizers, etc. However, this frequency range signifies the transition from the validity of the classical theory for the description of electron transport to the quantum domain behaviour, posing huge difficulties in the design of the required terahertz components.

One of the possible solutions is based on the use of antennas and transmission lines, which are commonly exploited for the manipulation of electromagnetic fields at radio and microwave frequencies. For the efficient radiation/scattering of THz waves by means of a single radiating element several approaches exist [1, 6, 10, 11]. However, the fabrication accuracy and the radiation efficiency, both of which depend on the materials chosen, challenge the applicability of these methods. Metals have small skin depths at these frequencies, which leads to high Ohmic losses and degrades the performance of antennas and transmission lines. The same problem equally applies to the design of other THz components, such as filters and modulators. Here, semiconductor-based devices such as low-temperature (LT) GaAs photoconductive modulators present a viable alternative [10].

Let us examine, for instance, two characteristic cases of THz-radiation modulation by utilizing semiconductor-based approaches. In the first case, the response of the semiconductor is controlled through an external optical field. The modulation of THz radiation by optically excited free electrons in a semiconductor was first demonstrated in [12] with the use of a mixed type I/type II GaAs/AlAs multiple quantum well structure. For electron densities $\sim 10^{11}\text{cm}^{-2}$ per quantum well at a temperature of 40K in a 20-period structure, the intensity of a transmitted THz beam (extending from 0.2 to 1THz) decreases by 40%. Clearly, optical excitation and cryogenic-temperature operation are major drawbacks for any practical THz modulator. As a more viable approach, the carrier concentration in semiconductors can be changed by electric injection or depletion of charge carriers. A room-temperature, electrically controlled THz modulator that includes a two-dimensional electron gas (2DEG) whose density is controlled by an

externally applied gate voltage is presented in [13]. More precisely, the use of 2DEGs in semiconductors has proven useful for the control of THz waves, in particular, with architectures similar to the high electron mobility transistor (HEMT). A HEMT is a field effect transistor which utilizes 2DEGs at the heterojunction of a highly doped donor supply semiconductor (typically AlGaAs) and a pristine undoped semiconductor (usually GaAs). In this way, the HEMT avoids carrier scattering which arises in heavily doped semiconductors, as the donated carriers lie in the quantum well at the interface. Such a structure of a HEMT-like device, is shown in Fig. 1.2(a). In this particular structure, the 2DEG is confined at the interface between the undoped 1-$\mu$m-thick GaAs layer and the undoped $Al_{0.3}Ga_{0.7}As$ spacer layer. A 50-nm-thick silicon doped layer grown on top of the 7-nm-thick undoped $Al_{0.3}Ga_{0.7}As$ spacer provides the electrons for the 2DEG. The 2DEG of only few nanometers thick that is concentrated near the GaAs/AlGaAs surface can be depleted by the application of a negative gate voltage which induces an increase of the transmittance through the device. Fig. 1.2(b) shows the time trace of the modulation signal for different applied gate voltages. At a gate voltage of $-10$ V, the amplitude transmittance of the THz pulse increased by 3% over the spectral range from 0.1 to 2 THz. As expected, the modulation depth of the reported device is fairly small since the 2DEG has a thickness of only a few nanometers. Recently, novel approaches for modulating and filtering the THz radiation have appeared that include the use of micro-electro-mechanical (MEM) systems [14], carbon nanotubes [15], or graphene [16, 17].

The surge of interest in the THz domain coincided with the emergence of the field of metamaterials. Metamaterials are artificial composite media structured on a size scale smaller than the wavelength of external stimuli, which are able to offer unprecedented control over electromagnetic (EM) waves [18]. Whereas conventional materials derive their electromagnetic characteristics from the properties of atoms and molecules, metamaterials relay on the design of the artificial atoms they are composed of, known as meta-atoms. By tailoring the sizes and shapes of the meta-atoms, we can engineer metamaterials with resonances in the THz range, allowing them to act as signal processing units for the propagating waves. A wide range of devices can be designed this way, including among others modulators and filters for the THz radiation [17, 19–21].

In fact, the ability to engineer the response of the metamaterials in the desired

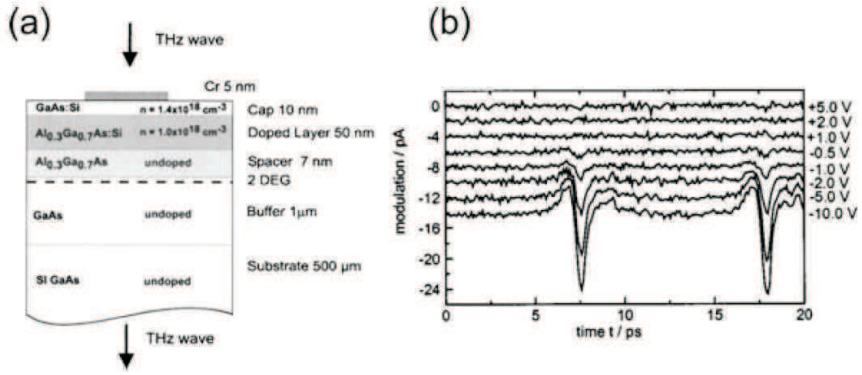


**Figure 1.2:** *(a) Epitaxial structure of an electrically driven, room-temperature THz wave modulator. The modulator is similar to high electron mobility transistors (HEMTs). (b) Time trace of the modulation signal for different gate voltages. A maximum modulation of 3% was observed over a frequency range from* 0.1 *to* 2 *THz [13].*

frequency range and tailor their electromagnetic properties on demand renders metamaterials one of the corner stones of the emerging THz technology. The first metamaterial designs targeting the THz gap appeared back in 2004 [22]. Initially, metamaterials were made to interact with either the electric [23] or the magnetic component [22,24] of terahertz waves, but later simultaneous electric and magnetic responses in THz metamaterials were also demonstrated [25]. Fig. 1.3 (a) and (b) show single and double Split-Ring Resonators (SRRs) optimised for operation in the THz region [19,24], while in Fig. 1.3(c) a ring-wire unit-cell of a THz negative refractive-index metamaterial is illustrated. These designs offered the functionalities of passive THz components such as filters and sensors operating at specific frequencies defined by the patterning of the metamaterial structure. The parameters of the metamaterial designs including the size and the shape of the meta-atom, the periodicity of the lattice, and the thickness of the layers of metals and dielectrics that form the structure were defined by the time of fabrication and remained fixed.

Implementing dynamic control and tunability of the metamaterial response later-on opened the way towards active THz components [26], such as modulators and switches [27]. A number of active THz metamaterials have been already demonstrated, exploiting various control schemes including light [28], voltage [21], or concepts such as MEMs in the design [29]. For instance, in [20] all-electronic THz switching and modulation operating at room temperature have been accomplished by the use of a hybrid

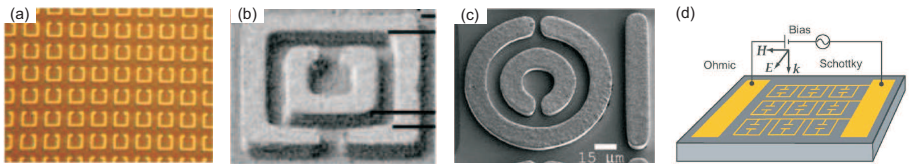


**Figure 1.3:** *(a) and (b) Split Ring Resonators (SRRs) optimised for operation in the THz region. From [24] and [19]. (c) Negative-index metamaterial from a ring-wire structure for operation in the THz [25]. (d) Electrically controlled THz modulator: biasing through an external electric circuit the array of SRRs that also create Schottky contacts with the substrate, allows the modulation of the incoming electromagnetic wave [20].*

of a metamaterial and a Schottky diode structure (see Fig. 1.3(d)). In this design, electric ring resonators are patterned to form a square array with wires as inter-unit cell connections. Thus the entire metamaterial array can function as a grid for biasing of the underlying semiconductor. Such a metamaterial can be fabricated on top of a $2\mu$m thick epitaxial n-doped GaAs layer with the electron density of $2 \times 10^{16}\text{cm}^{-3}$ grown on a supported SI-GaAs wafer. The metal-semiconductor interface forms a Schottky diode permitting depletion underneath the metamaterial. The carrier density can be actively controlled by applying a voltage bias between the metal and the substrate. Thus, such a metamaterial device can be used for the modulation of THz waves, as the conductivity of the substrate changes and subsequently switches the resonance of the metamaterial. At zero applied bias, the resonance response is damped due to the lossy conductive n-doped GaAs region. However, a reverse voltage bias is sufficient to deplete the lossy carriers such that the metamaterial resonance is re-established. With this device an intensity transmission modulation over 50% can be achieved in the THz regime [20]. Furthermore, appropriate metamaterial structures able to act as very efficient filters were shown [30]. In addition, the demonstration of metamaterials with broadband resonant behaviour led to the design of THz absorbers [31]. Despite the reported advancements, the field of THz metamaterials remains in its infancy, so yet more interesting THz metamaterial-based devices able to result in real-life applications are expected.

Metamaterials usually incorporate structured metals, thus they suffer from dissipative losses as the size of their metallic elements shrinks to meet the THz frequencies requirements [32]. As part of this thesis, we considered replacing metals with superconductors. The ability of superconductors to show zero DC resistance below their

critical temperature, and very low AC resistance compared to normal metals creates an interesting opportunity to dramatically reduce losses in metamaterial structures in the THz range. Furthermore, superconducting state is known to be sensitive to various external stimuli, such as light, electrical current, magnetic field and temperature, thus naturally providing ways of tuning and controlling the response of the metamaterial structures. We also note that superconductors alone being macroscopically quantum solid-state systems exhibit very intriguing physics, and thus exploiting superconductor phenomena in our work should open a direct gateway towards quantum metamaterials.

The main contributions of this thesis in the field of metamaterial-based manipulation of THz radiation (see Chapter 3) are the development and demonstration of superconducting metamaterials made of low-$T_c$ superconductor Nb and high-$T_c$ superconductor YBCO, which show sharp resonances in the sub-THz domain (millimeter waves), the first demonstration of temperature control of a Fano resonance in a superconducting metamaterial, and the first experimental realisation of the extraordinary transmission effect in a periodically perforated superconducting film. Also the first attempt to develop and experimentally demonstrate a quantum superconducting metamaterial was made.

## 1.3 Guiding THz Radiation

In the previous section, we briefly discussed how terahertz fields can be manipulated using devices that are designed for this frequency regime and what are the drawbacks of these devices. Serious difficulties also limit the number of available methods for guiding terahertz fields. Unlike the available low loss optical fibers for the near-IR wavelengths, THz waveguiding solutions based on bare metal wires [7], hollow-glass metallic waveguides (Fig. 1.4(a)) [33], and photonic crystal fibers (Fig. 1.4(b)) [34] are characterized by a fairly sizeable attenuation, typically in the $0.01 - 0.03$ cm$^{-1}$ range [1]. Losses in metallic waveguides operating at THz frequencies are attributed to the finite conductivity of metals and in dielectric waveguides to the high absorption of the dielectrics commonly used. Moreover, such waveguiding systems suffer from strong dispersion of the supported modes [7]. An approach based on a parallel-plate copper waveguiding structure, yielding almost dispersionless propagation of THz waves,

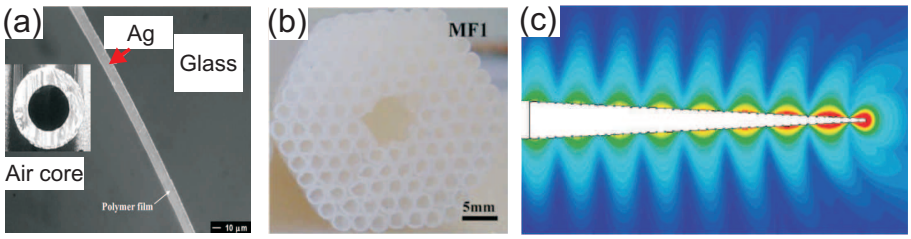


**Figure 1.4:** *Different structures able to provide terahertz waveguiding. (a) A hollow-core glass waveguide with inner coating of Ag. The inset shows the full cross section. [33]. (b) An air-core microstructure fiber [34]. (c) Calculated electric field distribution in superfocusing of a terahertz wave with the use of a spoof-plasmon cone waveguide [36].*

was proposed in [35], but the losses issue remains. Therefore, it seems unlikely that conventional waveguiding solutions will be utilized for the propagation of THz waves.

Long-distance free-space propagation of THz waves seems to be also impossible due to high propagation-losses. The main factor responsible for the attenuation here is attributed to the atmosphere, which absorbs, refracts, and scatters terahertz waves [1]. Nevertheless, exploiting THz frequencies potentially offers much higher information capacity (i.e., the maximum transmission rate allowed in a communication system) in comparison to microwaves due to the larger modulation bandwidth that is provided in THz frequencies. Therefore, THz waves can be used for the transfer of data in information-processing circuits or in guiding of high resolution THz imaging signals from the detectors to the processing units. Such applications would require waveguiding solutions with extreme sub-wavelength confinement of the guided THz modes.

The last requirement renders conventional THz waveguiding structures useless, since they are diffraction limited [9]. Recently, the field of plasmonics emerged as a promising new device technology that aims to exploit the unique optical properties of metallic nanostructures and enable routing and active control of electromagnetic waves at the nanoscale [37, 38]. Actually, surface plasmon polaritons (SPPs) are electromagnetic waves coupled to collective oscillations of the conducting electrons that propagate along the interface between a conductor (usually a metal) and a dielectric [39]. The surge of interest in this field is related mainly to the ability of SPPs to concentrate light beyond the diffraction limit [40]. Their subwavelength localisation emerges in the range just below the plasma frequency of the conductors used, which in the case of noble metals such as Au, Ag, etc. corresponds to the visible light frequencies. Owing to these

unique properties of plasmons, the plasmonic technology is believed to bridge the gap between electronics and photonics, enabling hybrid data processing chips with nanoscale circuitry that can operate at optical frequencies [40]. In this way, plasmonics create the opportunity to combine the size of electronics and the speed of dielectric photonics, thus enhancing the merging between these technologies. However, there are two main drawbacks of plasmonics that remain to be solved before this technology can be adopted for real-life applications, namely, high losses associated with the utilization of metals at optical frequencies and the dispersive nature of SPP waves.

In the last decade, researchers have demonstrated artificial SPP modes at frequencies that lay outside the optical part of the spectrum. The first ground-breaking work reporting the existence of low-frequency SPP modes is commonly associated with a letter published in Science by John Pendry [41], who termed these modes as "spoof plasmons" and showed that they appear along structured metallic surfaces. It is fair to mention at this point that the concept of such bounded electromagnetic modes had been introduced several decades before but had not been related to plasmons. For example, the idea of using surface corrugations in the radio and microwaves domains had been discussed by Collins [42] back in the 1960s, with a number of experimental demonstrations involving frequencies up to THz domain reported soon afterwards [43].

Terahertz waveguiding in the form of spoof plasmons on corrugated wires was shown to achieve high localisation of the propagating mode near the surface of the wire [44]. Similar experiments with corrugated wires demonstrated the ability to achieve high sub-wavelength resolution in imaging with THz fields; an effect that is known as superfocusing [36, 45] (Fig. 1.4(c)). Nevertheless, this enhancement of the localisation of the THz waves compared to conventional waveguides still comes at the cost of increased dissipation losses and strong dispersion of the guided modes.

In this thesis (see Chapter 4), we identified superconductors as intrinsically plasmonic media and showed that for certain waveguide geometries virtually dispersionless plasmonic modes could be supported at the THz frequencies and below, exhibiting extreme localisation and very low propagation losses. This work, thus, introduced the new field of superconducting plasmonics, which can find applications in high-rate data processing circuits, enabling brute force speed enhancement of two to three orders of magnitude compared to the state-of-the-art technology of today. The latter could be

considered as an intermediate step from conventional analog and digital electronics towards long-awaited all-optical circuits.

## 1.4 Generating THz Radiation

The difficulty of generating THz fields has been perhaps the most prominent reason for keeping this part of the spectrum outside scientific investigation and commercial applications for many years. As we have mentioned in Section 1.1, conventional electronic devices seize operating efficiently when we move in frequency above a few hundreds of GHz, while natural materials start showing a response resulting from intraband transitions not buried in thermal noise and having energies corresponding to the THz frequencies only when the far-IR region is approached.

Most of the existing THz sources usually have very low efficiencies in terms of generating THz radiation and cannot achieve useful output power levels (e.g., above the range of 1W), being also too bulky for most intended applications. From an economics perspective, low efficiency and large dimensions of THz generators are translated into increased cost, while the tunability of the output frequency (i.e., the ability to tune the frequency of the generated THz radiation) is an even harder goal to achieve.

An interesting review of various methods of THz fields generation is presented in [46], while here we just summarize a few widespread ways of achieving this. Some of the most common approaches for the generation of THz waves are based on using optoelectronic generation methods. There are a number of options for converting beat frequencies from visible/near-IR laser beams to THz radiation, including photodetection methods, cw photomixing, and, of course, time-domain THz generation [47].

One of the oldest methods utilizes photoconductive materials such as low temperature GaAs [10, 11]. This method is extensively used in THz time-domain spectroscopy (THz-TDS) [48]. The photoconductive surface acts as a fast switch connected to a metallic (e.g., golden) THz antenna, as it is shown in Fig. 1.5(a). When the unilluminated structure is biased with a constant voltage, no current flows in the device, since there are virtually no optical induced charge carriers in the photoconductive switch. Upon illumination with a short optical pulse ($<$ 100fs), for example from a mode-locked Ti:sapphire laser, the photoconductive switch closes (becomes highly con-

ductive), leading to a brief surge of current in the antenna structure, which induces a freely propagating THz electromagnetic wave. The frequency content of such a wave spans roughly from 0.1 to 2.5THz.

Rather than using optical sources and mixing down the frequency to access the THz range, one could start from the microwave frequencies and exploit the reversed process, reaching the THz spectral range by frequency multiplication. Usually, Schottky diodes are used as microwave frequency multipliers [49]. This method yields frequencies of up to 500GHz[1].

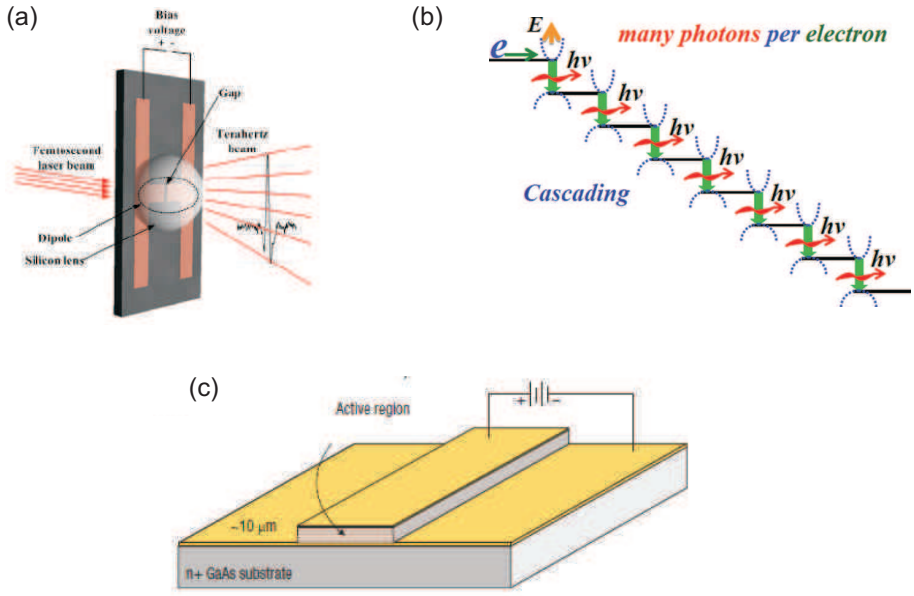


**Figure 1.5:** *(a) A photoconductive surface connected with an antenna that allows the generation and the transmission of THz waves [10]. (b) In Quantum-Cascade Lasers (QCLs), once an electron undergoes an intersubband transition and emitts a photon in one period of the superlattice, it can tunnel into the next period of the structure where another photon can be emitted. This process in which a single electron causes the emission of multiple photons as it propagates through the QCL structure justifies the name cascade and makes a quantum efficiency of greater than unity possible. (c) A waveguide structure of a QCL [50].*

Perhaps the most important discovery regarding the THz generation up to now has been the use of Quantum-Cascade Lasers (QCLs) at the THz frequencies [2], previously operating only in the IR range. Terahertz quantum-cascade lasers can now deliver milliwatts or more of continuous-wave coherent radiation throughout most of the terahertz range −more precisely covering the spectral regime between millimetre and infrared

[1]This was the way we used for generating the millimetre waves in the experiments involving superconducting structures reported in this thesis.

wavelengths. In essence, the QCL is a semiconductor source based on the engineering of electronic wavefunctions on a nanometer scale. The optical transition, which is injection pumped through resonant electron tunneling, occurs between the conduction subbands created by quantum confinement in a semiconductor heterostructure. More precisely, a QCL comprises a periodic series of thin layers of varying material composition forming a superlattice. The superlattice introduces a varying electric potential across the length of the device, meaning that there is a varying probability of electrons occupying different positions over the length of the device. This is referred to as one-dimensional multiple quantum well confinement and leads to the splitting of the band of permitted energies into a number of discrete electronic subbands. By suitable design of the layer thicknesses it is possible to engineer a population inversion between two subbands in the system which is required in order to achieve laser emission. Since the position of the energy levels in the system is primarily determined by the layer thicknesses and not the material, it is possible to tune the emission wavelength of QCLs over a wide range (from a few microns to well above 100$\mu$m) in the same material system. Additionally, in QCLs, once an electron has undergone an intersubband transition and emitted a photon in one period of the superlattice, it can tunnel into the next period of the structure where another photon can be emitted (see Fig. 1.5(b)). This process in which a single electron causes the emission of multiple photons as it propagates through the QCL structure gives rise to the name cascade and makes a quantum efficiency of greater than unity possible. This increased quantum efficiency can result in high output power levels. Usually in a quantum cascade laser, the mentioned quantum well structure is embedded in a waveguide, and the laser resonator is mostly of Distributed-Bragg-Reflector (DBR) or Distributed-Feedback (DFB) type (see Fig. 1.5(c)). There are also external-cavity QCLs, where a wavelength tuning element such as a diffraction grating is part of the resonator. Electrical control of the diffraction grating offers a degree of tunability of the emitted THz-radiation wavelength [51].

An extensive analysis of the operation principles behind the QCLs can be found in [50]. Since this is beyond the scope of this thesis it will not be discussed further here. The intention of the author is just to give a picture of the rather complicated environment of THz sources classified based on the targeted frequencies and their way of operation, which is conceptually better illustrated in Fig. 1.6.

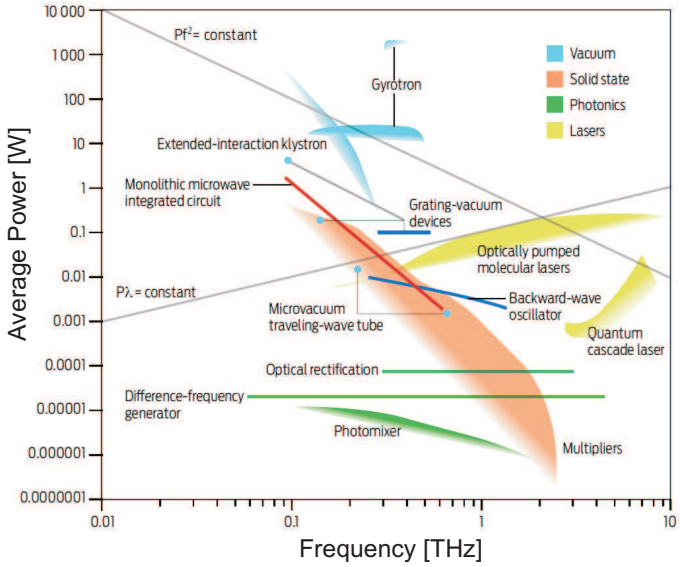


**Figure 1.6:** *Different kinds of technologies for the generation of THz waves, classified according to their frequencies of operation and average power of the transmitted waves [3].*

An important sub-area of THz sources covers the methods of generating magnetic fields. The ability to create strong magnetic pulses in this frequency region is important for applications in magnetic data recording and time-domain THz magnetic spectroscopy (which is required in fundamental solid-state physics research). As far as the magnetic recording technology is concerned, the demand to achieve higher densities of the recorded bits significantly reduces the size of the bit-domains in the magnetic medium and requires harder magnetic materials, which reduces the effect of thermal fluctuations on the stability of the stored information and improves the reliability of the storage device. Correspondingly, strong magnetic fields with very small localization areas are required to achieve efficient recording in such conditions. With the exception of high intensity accelerator-based electron sources [52], there are not many tools available that allow the direct generation of magnetic fields and probe magnetization at the nanoscale with ultrafast temporal dynamics.

In this thesis, we theoretically demonstrate for the first time (see Chapter 5) optically induced generation of Tesla magnetic pulses with ultrafast temporal dynamics and nanoscale localization using metamaterials. We introduce the design of metamaterial plasmonic resonators utilizing thermoelectric materials and show that appropriate nanoscale bimetallic rings can act as Tesla-scale magnetic field generators, through an

interplay between the optically driven transient Peltier-Seebeck effect [53] and their lowest-order dipole plasmon resonance. Our work also shows that Ohmic losses, usually perceived as a drawback in metamaterials research, can form an efficient energy transform mechanism that could be useful.

## 1.5 Thesis Overview

In this chapter a brief insight in the motivation behind the work reported in this thesis was given along with the introduction of some of the most important concepts exploited by the present research. The chapter also discussed the role and importance of our work from the perspective of both science and applications of THz radiation, and gave a brief account of the most important achievements in the domains of manipulating, guiding, and generating THz fields. Additionally, the areas of THz research to which this thesis contributes the most are highlighted. The reader should now be ready to proceed to the actual work in the following chapters.

Chapter 2 gives a detailed description of the methods and techniques used for obtaining the main results reported in this thesis. Those include spectroscopy, free-space transmission and reflection characterisation in the sub-THz (millimetre-wave) part of the spectrum, computational modeling, analytical derivations, and methods recruited to fabricate the superconducting samples and achieve their cryogenic cooling.

In Chapter 3 starts the main body of this thesis work. There, the manipulation of sub-THz waves is shown by exploiting metamaterials made of superconductors. The chapter starts by introducing the fields of metamaterials in general and superconducting metamaterials in particular. Experimental results obtained for various superconducting metamaterials are presented together with a theoretical model to explain their response. The first demonstration of controlling Fano resonances with temperature is reported along with the study of the influence of temperature change on the extraordinary transmission effect exhibited by a thin-film superconducting hole array.

Chapter 4 describes our work on THz waveguiding, which exploits superconducting plasmons. The chapter starts with the formal introduction to the field of plasmonics research. The theory of propagating plasmon modes is given and a connection is made with circuit theory. Such treatment offers a comprehensive description of the plasmonic

propagation phenomenon and provides a deeper insight into its hybrid nature. Based on the theory presented, the plasmonic nature of superconductors is revealed. The chapter ends with the introduction of the field of superconducting plasmonics, and the demonstration of certain geometries in which superconductors are capable of supporting low-loss dispersionless plasmon waves with extreme confinement. Possible practical applications are also discussed.

Chapter 5 deals with the optical generation of Tesla magnetic pulses localised at the nanoscale utilizing the thermoelectric effect in bi-metallic metamaterials. The chapter starts with a brief theory of thermoelectric effects. Then, the design and study of a metamaterial structure made of bimetallic rings of Gold (Au) and Nickel (Ni) is presented. The chapter discusses the results describing Tesla-scale magnetic fields localised in the nano-rings with sub-ps temporal dynamics, and concludes with the importance of this effect for several practical applications.

Chapter 6 summarizes the main results of this thesis and offers suggestions for further work in the future, while in Appendix A the reader can find a useful introduction to the theory of superconductivity.

# 2 Methods

This chapter gives a detailed description of the methods and techniques used for obtaining the main results of the thesis. Those include spectroscopy, free-space transmission and reflection characterisation in the sub-THz (millimetre-wave) part of the spectrum, computational modeling, analytical derivations, and methods recruited to fabricate the superconducting samples and achieve their cryogenic cooling.

## 2.1 Millimetre-wave Spectroscopy

Spectroscopy is the study of the interaction between matter and radiated energy as a function of frequency [54]. In optical spectroscopy, which is, perhaps, the most well known, to extract information regarding the response of matter under examination to light waves, the transmitted and/or reflected radiation is measured when a light wave of known intensity is incident on its surface. Also, the absorption spectrum of a material can be measured, which in combination with the transmittance and reflectance can lead to the estimation of the complex refractive index. The same concepts apply to microwave and millimetre-wave frequency domains [55].

At millimetre-wave frequencies, light sources and lasers are replaced with electronic analogues (mixers and oscillators), while the electromagnetic waves are radiated and received by antennas. A vector network analyser (VNA) is an instrument used for the characterisation of networks or devices operating in this spectral range, by comparing the amplitudes and the phases of the transmitted and received signals at its ports. Our experimental setup was based on an Agilent PNA-X 5242 A vector network analyser, which was equipped with two millimetre-wave sources able to drive electrical voltages

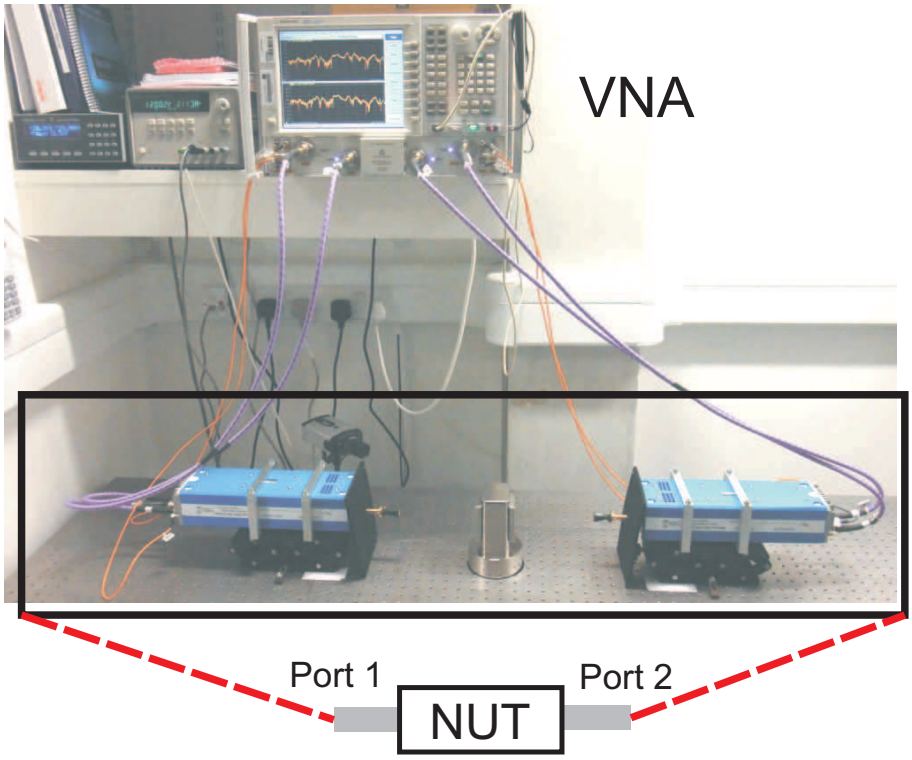


**Figure 2.1:** *The experimental setup extending from the output of Port 1 of the VNA to the input of Port 2 constitutes a two-port network, which is called network under test (NUT).*

with frequencies between 75GHz and 110GHz. Since our interest was in free-space measurements, the sources were connected to two linearly polarised horn antennas.

A part of the experimental setup, shown in Fig. 2.1, which includes the coaxial feed-cables, the millimetre-wave heads, and the antennas can be considered as a two-port network, referred here as network under test (NUT). This network can be characterised in terms of reflection and transmission coefficients associated with its ports. The power of transmitted and reflected radiation is obtained by measuring simultaneously the amplitude and the phase of input and output voltage signals at the ports of the network.

In fact, the complete description of the reflection and transmission coefficients, as well as the intrinsic losses or gain of the two-port network, can be obtained by the S-parameters description [55]. A two-port network is characterised by four S parameters, namely $S_{11}$, $S_{12}$, $S_{21}$, and $S_{22}$. The first number of the index corresponds to the port on which the signal is applied, while the second number to the port from which the signal emerges. For example, $S_{21}$ is a measure of the signal coming out of port 1 relative to the millimetre wave stimulus entering port 2. $S_{11}$ and $S_{22}$ represent reflection

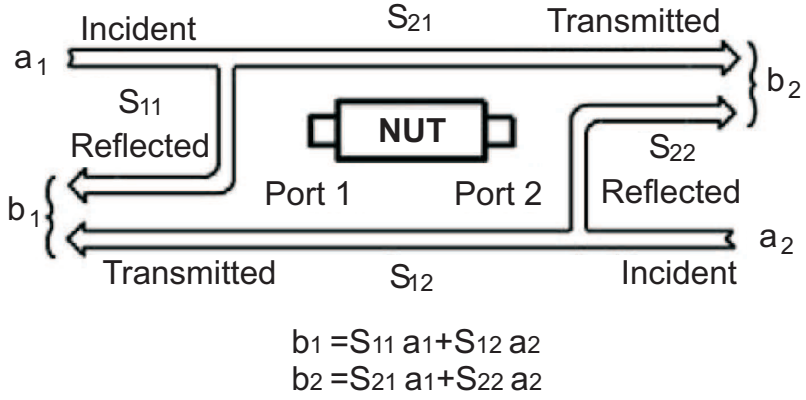


**Figure 2.2:** *A graphical illustration of the S-matrix representation of a two-port network.*

coefficients measured at ports 1 and 2 respectively. These coefficients are calculated as the ratio between the complex voltage levels of the signals that enter and leave the NUT through the same port (see Fig. 2.2). Assuming that the voltage levels of the signals propagating from the VNA towards the ports 1 and 2 of the NUT are denoted as $a_1$ and $a_2$ respectively, while the ones propagating from the ports of the examined network to the VNA as $b_1$ and $b_2$, we have:

$$\begin{pmatrix} b_1 \\ b_2 \end{pmatrix} = \begin{pmatrix} S_{11} & S_{12} \\ S_{21} & S_{22} \end{pmatrix} \begin{pmatrix} a_1 \\ a_2 \end{pmatrix}. \tag{2.1}$$

The physical interpretation of the S-matrix can also be derived immediately from the matrix equation (2.1). When no input is assumed for port 2 ($a_2 = 0$), $S_{11} = \frac{b_1}{a_1}$, and $S_{11}$ is the reflection coefficient associated with port 1, while $S_{21} = \frac{b_2}{a_1}$ is the transmission coefficient from port 1 to port 2 (as illustrated in Fig. 2.2).

An alternative description of a two-port network is based on the transmission (ABCD) matrix. In contrast to the S-matrix, which involves only voltages, it relates both voltage and current levels at the network's ports. The transmission matrix has

the following components:

$$A = \frac{V_2}{V_1}|_{I_1=0}, \tag{2.2}$$

$$B = \frac{V_2}{I_1}|_{V_1=0}, \tag{2.3}$$

$$C = -\frac{I_2}{V_1}|_{I_1=0}, \tag{2.4}$$

$$D = -\frac{I_2}{I_1}|_{V_1=0}, \tag{2.5}$$

which lead to the matrix representation:

$$\begin{pmatrix} V_2 \\ I_2 \end{pmatrix} = \begin{pmatrix} A & B \\ C & D \end{pmatrix} \begin{pmatrix} V_1 \\ -I_1 \end{pmatrix}. \tag{2.6}$$

The use of the ABCD-matrix description is convenient when two-port networks are cascaded. In this case, the resulting total two-port network has an ABCD matrix which is simply the multiplication product of the ABCD matrices of its components. The ABCD-matrix representation was used in the calibration procedure of our setup.

## 2.2 The Cooling Methods

In some of the experiments reported in this thesis superconducting materials were involved. Of course, handling superconductors required cryogenic cooling, which was achieved through the use of cryostats.

A cryostat is a device which is used to maintain very low temperatures (typically below $-150°$C) of the samples mounted within its volume. The low temperatures are achieved and maintained by a variety of different refrigeration methods, the most common of which rely on the use of liquid nitrogen (N) or liquid helium (He). A cryostat is usually assembled into a vessel, similar in construction to a vacuum flask or Dewar. Based on the refrigeration method cryostats can be distinguished in four categories: closed-cycle, continuous-flow, bath, and multistage.

For our experiments, initially, a continuous-flow liquid nitrogen cryostat was used. Cryostats of this category are cooled by liquid nitrogen (which is the cryogen) from a storage dewar. As the cryogen boils within the cryostat, it is continuously replenished

by a steady flow from the storage dewar. Temperature control of the sample within the cryostat is performed by controlling both the flow rate of cryogen into the cryostat and the heat generated by a resistor placed nearby the sample. This heating resistor is controlled by a proportional-integral-derivative (PID) temperature control loop. The length of time over which the cooling may be maintained is dictated by the volume of the storage dewar. In our case, that was in the range of several hours, which was adequate for performing our experiments. A photograph of the cryostat used in the experiments with the PID control loop and the dewar of liquid nitrogen is shown in Fig. 2.3(a).

Since the liquid nitrogen cryostat measurements could be performed only down to 77K, this device was limited in use for experiments involving only samples made of high-temperature superconductor YBCO. For the experiments involving niobium (Nb) a closed-cycle cryostat with liquid helium as a cryogen had to be exploited. Such cryostats include a chamber through which cold helium vapour is pumped. An external mechanical refrigerator extracts the warmer helium exhaust vapour, which is cooled and recycled. Closed-cycle systems consume a relatively large amount of electrical power, but need not be refilled with helium and can run continuously for a very long time (extending to thousands of hours of operation). Samples may be cooled by attaching them to a metallic cold-finger, which is inside a vacuum chamber and in thermal contact with the helium vapour chamber. The temperature is controlled by a PID control loop, which defines the heat released by a resistor attached to the cold-finger. A photo of this system is depicted in Fig. 2.3(b). Using this system temperatures as low as 6.9K could be achieved.

At this point we have to mention that for frequencies above 75GHz the free-space wavelength of electromagnetic radiation is smaller than 4mm, which implies that the size of our superconducting samples could be of the order of just a few square centimetres (as we show in Chapter 3). That allowed us to use conventional compact optical cryostats while conducting free-space measurements, with the millimetre-wave antennas and the rest of measuring apparatus placed outside the cryostats (see next section for more details).

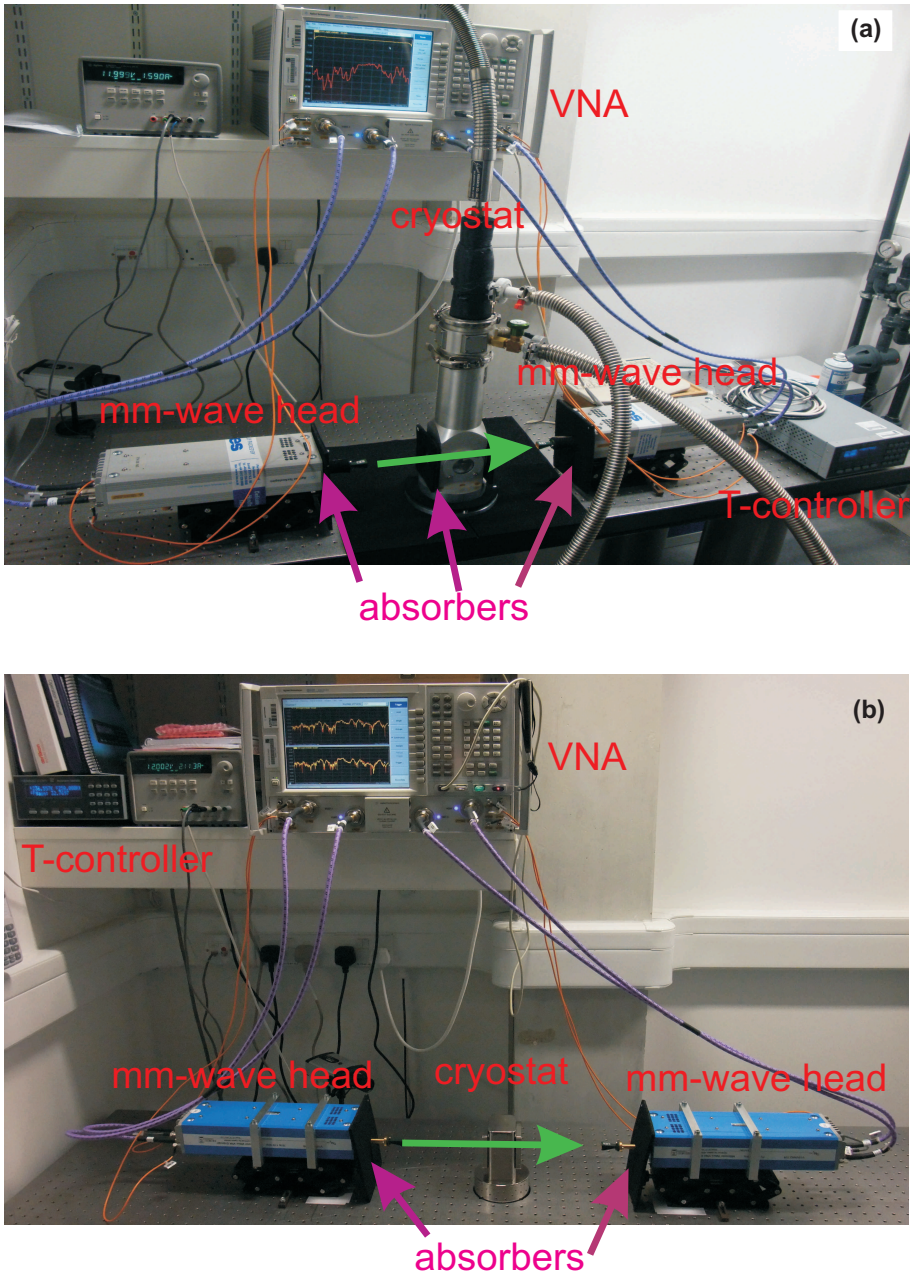


**Figure 2.3:** *(a) The experimental setup with a liquid nitrogen cryostat between the two millimetre-wave heads. (b) The same setup with a closed-cycle liquid helium cryostat in the middle.*

## 2.3 Experimental Setup

In millimetre waves the wavelength is adequately small compared to the microwaves to lead to very directional beams. This is directly implied by the Friis equation, which shows that free-space propagation losses, under ideal conditions, are proportional to the ratio of the radiation wavelength to the separation distance of the antennas squared [56]. In essence, the smaller the wavelength of the radiation, the smaller is the opening of the radiation wavefront (higher directionality). Thus, the link suffers from small propagation losses. In addition, the directivity of the millimetre-wave emitted radiation is further enhanced by the use of highly directional horn antennas. Therefore, the volume of the first Fresnel zone is made adequately small and interference to the received radiation from reflections or scattering from objects within this zone can be controlled and suppressed [57]. This behaviour implies that for measurements in this range no anechoic chamber is necessary. Nevertheless, reflecting surfaces of objects inside the Fresnel zone should have anti-reflecting coating, to minimise their influence.

All experiments were conducted using Flann Microwave WG27 high-gain horn antennas optimized for the operation in the 75GHz to 110GHz range of frequencies. The horn antennas had the diameter of 75mm and focused radiation to a spot size of 25mm at a distance of 460mm. Transmission and reflection measurements were performed by placing samples inside the cryostat, which was installed between the horn antennas and at the focal distance. The corresponding S-parameters were measured with the vector network analyzer Agilent N5242A PNA-X. The temperature was monitored and controlled with a PID control loop in the temperature range between 7K and 300 K. Achieving cryogenic temperatures required very low pressures of the order of $10^{-7}$mbars inside the volume of the cryostat, which were maintained using a turbo vacuum pump. In the case of experiments with the liquid nitrogen cryostat, since the windows area was smaller than the millimetre-wave beam opening, to suppress reflections from the cryostat located inside the Fresnel zone of the antennas, its metallic surfaces were covered with absorbing material optimized for millimetre radiation. However, since only the initial (and limited in number) experiments were performed using this cryostat, for the rest of the text we focus on the experimental setup involving the liquid helium cryostat. For this setup, the size-area of the windows was adequate to avoid scattering

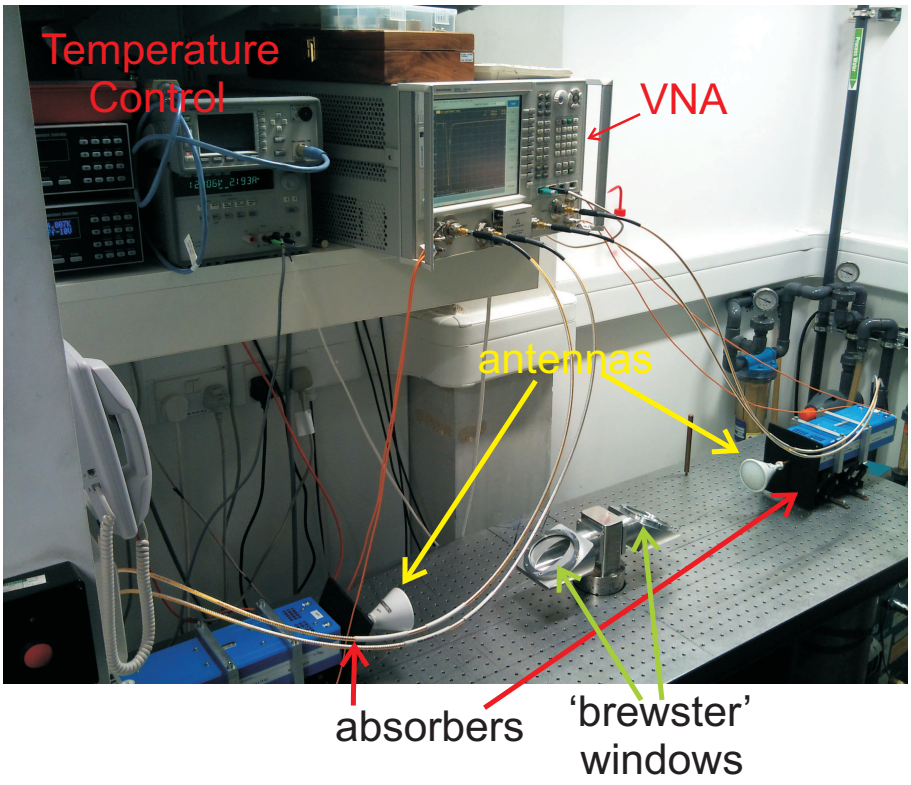


**Figure 2.4:** *The experimental setup with the closed-cycle liquid helium cryostat, which has its windows at the Brewster angle with respect to the direction of the incident wave.*

from their metallic surroundings. Therefore, in this case no absorbers had to be used around the cryostat's windows. Fig. 2.4 shows the final experimental setup used.

In our experiments the measured response of the samples placed inside the cryostat was affected by a number of setup-related factors, including the response of the vector network analyser itself, the millimetre-wave heads and the coaxial cables, the antennas and their feeding waveguides, as well as the scattering from the fixture of the cryostat. To eliminate those factors several steps had to be taken.

First, a two-port error correction procedure was applied [58], which minimized the VNA's main systematic errors related to (i) directivity, (ii) crosstalk, (iii) source impedance mismatch, (iv) load impedance mismatch, (v) reflection tracking, and (vi) transmission tracking. Below, we briefly describe this calibration procedure [59].

If we remove the antennas and the cryostat, then we can think of the rest (which includes the millimetre-wave heads with the output waveguides and the coaxial cables connecting the heads to ports 1 and 2) as the NUT. In addition, we can regard the

VNA as an ideal (error-free) device with two error boxes connected between its ports and the NUT (Fig. 2.5). Assuming that the scattering matrices of the error boxes have the form:

$$E_A = \begin{pmatrix} a_{00} & a_{01} \\ a_{10} & a_{11} \end{pmatrix}, \quad \text{and} \tag{2.7}$$

$$E_B = \begin{pmatrix} b_{00} & b_{01} \\ b_{10} & b_{11} \end{pmatrix}, \tag{2.8}$$

the transmission matrix of the NUT, $T_{\mathrm{NUT}}$, can be related to the measured transmission matrix $T_m$ by [58]:

$$T_{\mathrm{NUT}} = \frac{b_{01}}{a_{01}} A^{-1} T_m B, \tag{2.9}$$

where the $A$ and $B$ matrices are given by:

$$A = \frac{1}{a_{01}a_{10}} \begin{pmatrix} -|E_A| & a_{00} \\ -a_{11} & 1 \end{pmatrix} \tag{2.10}$$

$$B = \frac{1}{b_{01}b_{10}} \begin{pmatrix} 1 & -b_{11} \\ b_{00} & -|E_B| \end{pmatrix}. \tag{2.11}$$

By connecting three calibration standards (NUTs with known responses) between the error boxes of the ideal VNA, the components of the $A$ and $B$ matrices can be estimated. An extra measurement of one of the standards connecting both ports is required to estimate the proportionality term $\frac{b_{01}}{a_{01}}$. In our case, these calibration standards included a direct waveguide connection (short circuit), a waveguide with a block with a metallic plate (open circuit), and a $\lambda/4$ waveguide section.

The procedure presented above corrects most of the errors introduced by the electronics and coaxial/waveguide interconnects. However, this procedure cannot eliminate the errors induced in free-space by the antennas and the rest of the setup components placed between them, with the cryostat providing the most significant contribution. These errors include interference of the transmitted and reflected fields with fields scattered at the edges of the samples and at the fixture supporting the sample in the

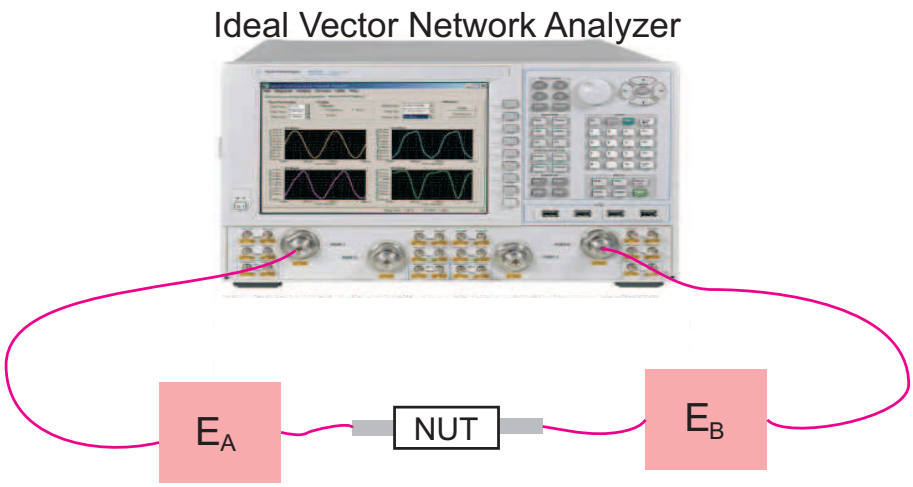


**Figure 2.5:** *For calibrating the VNA we can regard it as an error-free (ideal) device with two error boxes connected between its ports and the NUT.*

cryostat, multiple reflections between the antennas and between the antennas and the sample as well as multiple reflections between the windows of the cryostat. The procedures of eliminating these errors are detailed in the remainder of the present section.

Although the easiest way of reducing the parasitic scattering at the sample edges could be, perhaps, to make the area of the samples larger than the cross-section of the millimetre-wave beam (typically more than 1200mm$^2$), cooling samples of that size down to cryogenic temperatures would be very challenging, if not impractical. Also, the fairly standard method of the gated reflect line calibration [58] could not be applied here because of the insufficient accuracy in repositioning the samples during the calibration process (which required mounting and demounting the cryostat itself). Our solution was to place an aluminium-foil screen inside the cryostat, so that no radiation could pass around the samples towards its output window. The thickness of the aluminium foil was several times larger than its skin depth at millimetre-wave frequencies, which guaranteed no radiation leakage.

As it was mentioned earlier, the largest source of errors during the free-space measurements was the cryostat itself. It could practically accommodate only the samples, having no room for hosting the antennas. To maintain proper vacuum inside the cryostat and thermal insulation from the outside environment, its transparent glass windows had to be made several millimetres thick, which inevitably affected the propagation of millimetre-wave radiation. In particular, that led to the appearance of several resonant

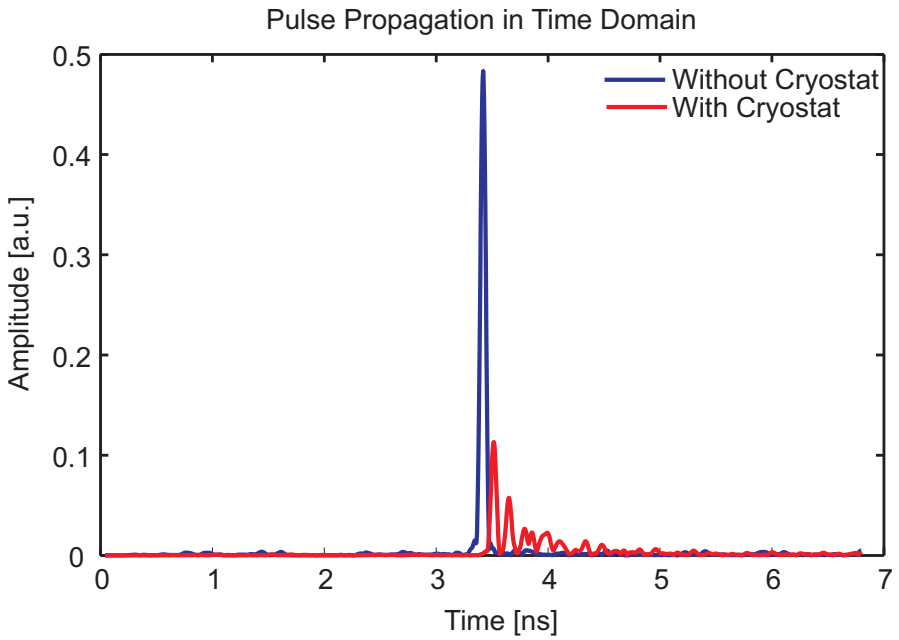


**Figure 2.6:** *A pulse in time domain consisting of spectral components in the range from* $75\,GHz$ *up to* $110\,GHz$ *(a) without the cryostat and (b) with the cryostat between the antennas.*

cavity modes created between the surfaces of the two windows as well as in the bulk of each window. The effect of these modes is illustrated in Fig. 2.6, which shows the response of the NUT in the time domain. In the absence of the cryostat, it corresponds to a 200ps pulse containing all spectral components and propagating between the antennas (blue line). The multiple interference produced by the cryostat cavities delays the arrival of this pulse and, more importantly, leads to the appearance of several strong echo pulses that muddle the response (red line). In order to resolve this issue we had to place the windows at the Brewster's angle with respect to the direction of incidence, as shown in Fig. 2.4. According to the Fresnel equations, an electromagnetic wave with $p$ polarization (electric field polarised in the same plane as the incident ray and the surface normal) will not be reflected by an interface between two media, if the angle of incidence is [60]:

$$\theta_B = \arctan\left(\frac{n_2}{n_1}\right), \tag{2.12}$$

where $n_1$ is the refractive index of the initial medium through which the light propagates (the "incident medium"), and $n_2$ is the index of the other medium. This equation is known as the Brewster's law, and the angle it defines is the Brewster's angle [60]. In our

case the two media are air with $n_1 = 1$ and glass with $n_2 = 1.95$, and the corresponding Brewster angle is 63°. Although tilting the cryostat windows at Brewster angle limited the polarization state of the waves entering and leaving the cryostat to p-polarization, it enabled to significantly reduce the effect of the cavity modes on the free-space response of our samples, while the polarization state interacting with the samples could be controlled by simply rotating the latter inside the cryostat. The measured pulse in time-domain with the cryostat in the case of Brewster angle windows resembled the pulse without the cryostat plotted with the blue curve in Fig. 2.6 plus a few remaining but attenuated echo pulses.

To account for any remaining errors the response of the samples was normalised against the empty cryostat. Meanwhile, the delayed copies of the transmitted pulse (echoes) due to multiple reflections from the antennas' apertures were easy to filter out in the time-domain given the sufficiently large separation between the antennas and the samples. The small-amplitude mechanical vibrations resulting from the pump of the cryostat weren't observed to cause any problems in the measurements (probably due to the large surface area of the sample and the incident plane-wave field used as excitation).

## 2.4 Analytical and Computational Modeling

Analytical modeling and numerical simulations play a crucial role as tools for designing samples and interpreting real-life experiments. In addition, these methods are important on their own, resembling in many ways thought-experiments which can deal with complex effects from various fields of physics, including interactions between electromagnetics, optics, heat transfer, mechanics, etc.

### 2.4.1 Analytical Modeling

Analytical calculations provide perhaps the most intuitive way of understanding an effect and gaining physical insight into its nature. In this thesis such analytic treatment is provided for many of the considered effects. In most of the cases, however, it forms a part of a much broader theoretical analysis and hence is presented in each chapter on a case-by-case basis. In particular, theoretical models have been built for describing

the superconducting metamaterials, the superconducting plasmonic structures and the thermoelectric metamaterials. Despite their importance in building intuition for the effects involved, most of such models cannot be used to describe complex geometries. In these cases, we had to resort to computational methods, which could handle not only the complexity of the geometries but also account for a number of different effects at the same time.

### 2.4.2 The Finite Element Method for Computational Modeling

Many physical phenomena such as elastic deformations, heat transfer, flow of liquids, propagation of electromagnetic waves, etc. can be expressed by the governing differential equations and their corresponding boundary conditions.

One of the most commonly used computational methods for finding approximate solutions to partial differential equations (PDEs) or systems of PDEs as well as (although less often) integral equations [61], commonly encountered in boundary value problems, is the finite element method (FEM). In simple terms, the FEM encompasses all the methods for connecting many simple element equations over many small sub-domains, named finite elements, which can be solved in relation to each other in order to approximate a more complex equation over a larger domain. The solution's approach is based on eliminating the spatial derivatives in the PDEs. This happens by approximating the PDEs with a system of algebraic equations for steady state problems or a system of ordinarily differential equations (ODEs) for transient problems. These systems of algebraic equations are linear, if the underlying PDEs are linear, and they are solved using numerical linear algebra methods [62]. In the case of ordinary differential equations that arise in transient problems, numerical-integration standard techniques are used, such as the Euler's method or the Runge-Kutta method [62].

The finite element method originated from problems in civil and aeronautical engineering and is a special case of the more general Galerkin method [61]. It can be traced back to the work of Alexander Hrennikoff and Richard Courant [63]. In its today's form, though, the method gathered momentum in the 1960s and '70s at the University of Stuttgart through the work of John Argyris and at Berkeley through the work of Ray W. Clough for use in the civil engineering discipline [64]. Since then, the FEM has been widely accepted in various other fields of science and engineering. Fur-

thermore, during the last decades, the elimination of spurious results –solutions of the approximating equations that are not satisfying the initial equation– together with the wide availability of much more powerful computation machines equipped with ample amounts of fast random-access memory (RAM) allowed the method to find applications in the field of electromagnetics, especially, in cases that simulations in the frequency domain are required.

When solving PDEs numerically, the primary challenge lies into approximating the precise solutions of the PDEs while remaining numerically stable. This last remark means that errors in the approximation of the initial values and of the intermediate results of the numerical calculations (since most of the these methods are iterative) do not accumulate in every step. If that was the case, the error between the final numerical output and the actual solution of the PDEs would be unacceptably large. The FEM is proven to be a good choice for solving PDEs in a number of challenging cases, namely when the PDEs are defined over domains with complex geometries, the size or location of a domain changes (e.g., moving boundaries), the desired precision changes over the entire domain (e.g., the ac current distribution in conducting materials is required with higher accuracy near the surface of the materials compared to their bulk), or the anticipated solution lacks smoothness. These advantages determined the choice of the FEM as the main method for computational modelling presented in this thesis.

Below we briefly describe the finite element method, with the aim to show its applicability to the electromagnetic problems we faced in this thesis. A more in depth treatment of the topic could be found in [61].

Consider a geometric space $\Omega$, and a partial differential equation (PDE), describing the physical phenomenon we want to investigate, defined within this space along with conditions at the boundary $\partial\Omega$. Then, the PDE can be written in the form:

$$L\phi - f = 0, \tag{2.13}$$

where $L$ is a linear differential operator embodying the physical properties of the system which determine the response $\phi$ in every point of $\Omega$, when the excitation $f$ is applied. The first step using the FEM is to discretize the domain $\Omega$. In essence, $\Omega$ is partitioned

into small units of a simple shape. This process is called meshing and hence the units of simple shape are the meshing elements. In this way, $\phi$ can be approximated by a linear sum of basis functions $N_i$ at discrete locations indexed by $i$, chosen from a linearly independent set, and weighted with values $\phi_i$. Therefore:

$$\phi \approx \tilde{\phi} = \sum_i N_i \phi_i. \tag{2.14}$$

By doing so, the response $\phi$ can be described by a finite number of parameters, denoted as $\phi_i$ for each of the basis functions $N_i$, which are the so-called degrees of freedom. We assume a total of $l$ degrees of freedom. The basis functions $N_i$ depend on the shape of the mesh elements and usually assume one of a few basic shapes (e.g., straight lines in 1D, triangles in 2D, etc.). Then, we define a residual $R$ between the approximate and the exact solutions of the differential equation:

$$R = L\sum_i N_i\phi_i - f - (L\phi - f) = L\sum_i N_i\phi_i - f - 0 = L\sum_i N_i\phi_i - f. \tag{2.15}$$

An efficient method to create a discretized version of the PDEs is through the minimization of the residual $R$. This can happen by choosing weighting functions $W_j$ such that, in some sense, the average value of $R$ over $\Omega$ is minimized. That is:

$$\min_{W_j}\left[\int_\Omega W_j R \mathrm{d}\Omega\right], \quad \text{for } j = 1, 2, .., l, \tag{2.16}$$

with the number of weight functions $W_j$ exactly equal to the degrees of freedom assumed. Thus, we derive the following linear system of equations:

$$K\dot{\Phi} = F, \tag{2.17}$$

with $K_{ji} = \int_\Omega W_j L N_i$, $\Phi_i = \phi_i$, and $F_j = \int_\Omega W_j f$. In the Galerkin method, upon which the FEM is based [65], the minimization of the error leads to the following weight functions:

$$W_i = \frac{\partial\tilde{\phi}}{\partial\phi_i} = N_i. \tag{2.18}$$

Note that $W_i$ are then identical to the original basis functions $N_i$. Note also that, after this step, the system of Eq. (2.17) can be solved with well established methods of linear

algebra.

In the case of electromagnetics, the FEM is applied to the wave equation for the electric (or the magnetic) field in the frequency domain, which is to be solved in $\Omega$ (which is defined by the geometry of the problem at hand):

$$\nabla \times \frac{1}{\mu_r} \nabla \times \mathbf{E} - k_0^2 \varepsilon_r \mathbf{E} = j k_0 Z_0 \mathbf{J}, \tag{2.19}$$

with the conditions $\hat{n} \times \mathbf{E} = 0$ and $\hat{n} \times \nabla \times \mathbf{E} = \mathbf{N}$ applied on the disjoint boundaries of elements in $\Omega$ or its outer surface $\partial\Omega$. Here, $\hat{n}$ is a unitary vector normal to the boundary surface and $\mathbf{N}$ corresponds to any existing surface currents. Furthermore, depending on the problem investigated, other conditions might also apply at other boundaries of the relevant structures. The convention assumed for the propagation of the wave is of the form $\exp(j(kz - \omega t))$, where $k_0 = \omega/c$, $\varepsilon_r$ and $\mu_r$ are the relative permittivity and the relative permeability tensors respectively, and $Z_0 = \sqrt{\mu_0/\varepsilon_0}$ is the free-space wave impedance.

As we have briefly described for the general case, we have to discretize the Eq. (2.19) in order to reduce the infinite number of degrees of freedom to a finite number. This is necessary so that a finite-memory machine can treat and solve the problem numerically. Therefore, the domain $\Omega$ has to be divided into a finite number of smaller domains called elements and approximated by standard geometrical shapes. For two-dimensional geometries the elements of choice are often triangles, while for three-dimensional geometries tetrahedra are normally used as elements. The "art" of simulating is to achieve the desired accuracy using the smallest number of degrees of freedom possible. However, the degrees of freedom of the chosen discretization of domain $\Omega$ should be adequate for the approximating solution to converge to the actual solution of the PDEs everywhere in $\Omega$. This convergence is achieved when the solution does not further increase in accuracy significantly as the number of elements is increased.

Once discretization has taken place, the values of $\mathbf{E}$ are calculated in the vertices of each element, while the solution at all other points of each element is estimated through interpolation using the basis functions $N_i$. Usually linear interpolating functions are employed, although higher order polynomials or even vector bases could be used [66]. Using bases of the latter type is more appealing as it is known to minimize spurious

errors [65]. Following this approach, within each element $e$, $\mathbf{E}$ can be approximated as [66]:

$$\mathbf{E}^e(x,y,z) = \sum_{i=1}^{m} \mathbf{N}_i^e(x,y,z) E_i^e, \tag{2.20}$$

where $\mathbf{N}_i^e(x,y,z)$ is the vector basis function and $E_i^e$ is the tangential component of the electric field at edge $i$ of element $e$ with $m$ nodes. Hence, summing over all element edges, excluding only those at $\partial\Omega$ where the tangential component of $\mathbf{E}$ vanishes, the electric field over the entire domain $\Omega$ is calculated:

$$\mathbf{E} = \sum_{i=1}^{l} \mathbf{E}_l^e(x,y,z), \tag{2.21}$$

where $l$ is the number of elements over the entire domain. At this stage Eq. (2.19) is multiplied by the weighting functions $W$ and integrated over the entire domain $\Omega$ [66]:

$$\int\int\int_V [(\nabla \times \mathbf{W})\mu_r^{-1}(\nabla \times \mathbf{E}) - k_0^2 \mathbf{W}\varepsilon_r \mathbf{E}]dV =$$
$$= \int\int_{\partial\Omega} \hat{n}[\mathbf{W} \times (\mu_r^{-1}\nabla \times \mathbf{E})]d\mathbf{S} + \int\int\int_V jk_0 Z_0 \mathbf{W}\mathbf{J}dV. \tag{2.22}$$

Now, the boundary conditions can be directly introduced into the problem. This can happen by separating the surface integral of Eq. (2.22) into different components, each one corresponding to a different boundary for which the desired condition can be applied. Finally, substituting Eq. (2.18) in Eq. (2.22) for the weighting functions $W_j$, the following linear system of equations emerges:

$$K\dot{E} = b, \tag{2.23}$$

where $K$ is the so-called stiffness matrix and $b$ is the vector of excitations given by:

$$K_{ij} = \int\int\int_V [(\nabla \times \mathbf{N}_j)\mu_r^{-1}(\nabla \times \mathbf{N}_i) - k_0^2 \mathbf{N}_j \varepsilon_r \mathbf{N}_i]dV - \int\int_{\partial\Omega} \hat{n}[\mathbf{N}_j \times (\mu_r^{-1}\nabla \times \mathbf{N}_i)]d\mathbf{S} \tag{2.24}$$

and

$$b_j = \int\int\int_V jk_0 Z_0 \mathbf{N}_j \mathbf{J}dV. \tag{2.25}$$

The choice of appropriate boundary conditions is crucial for achieving accurate results. Perfect Electric Conductor (PEC) conditions and Scattering Boundary Conditions (SBCs) [55] or Perfectly Matched Layers (PMLs) [66] were commonly used to simplify our models. In the case of the PEC condition, as the name itself implies, the surface is assumed to be a perfect conductor on which the tangential component of the electric field is set to zero. On the other hand, PMLs and SBCs are used to create computationally the impression of wave propagation into infinite space. In some cases of superconducting layers, more sophisticated boundary conditions had to be used to model their behaviour, since superconducting nanometre-thin layers can be proven to be different from PEC. These boundary conditions for the case of superconducting surfaces are described in Chapter 3.

As we mentioned in the beginning of this section, equations describing heat transfer as well as magnetostatic and electrostatic field distributions can be treated by the FEM. These equations had to be taken into account while describing the thermo-magnetic effect in metamaterials and are described in depth in Chapter 5. Most of the PDE-type problems considered in this thesis were solved numerically using the commercial package Comsol Multiphysics 3.5. This package provided a convenient graphical user interface for specifying the geometry of the problems, generating the mesh, and calculating the numerical solution.

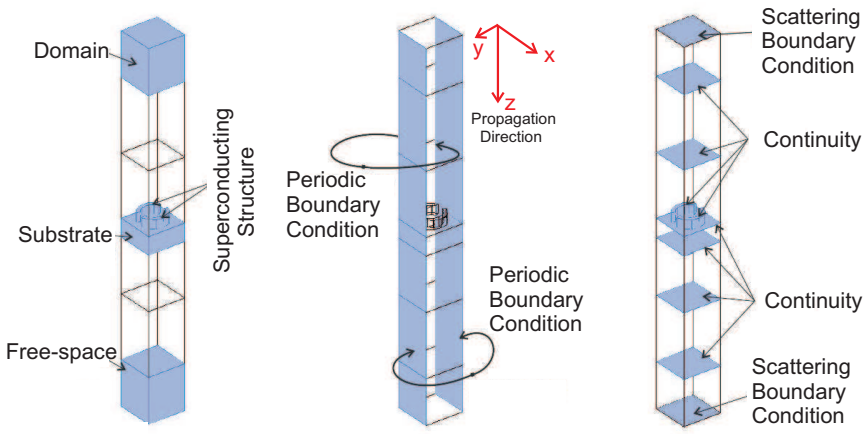


**Figure 2.7:** *A model used in FEM simulations for metamaterial structures showing the geometry involved and the boundary conditions used. The figure is inspired by [59].*

The FEM-model of a metamaterial, which is almost universally used across this thesis (excluding the work on modelling plasmon propagation reported in Chapter 4) is presented in Fig. 2.7. This model describes the interaction of a plane electromagnetic wave with a periodic metamaterial array, which is represented by a single unit cell. The incident wave is considered to propagate along the positive z-axis, while the metamaterial extends in the xy plane. In order to simulate the open space termination, the top and bottom boundaries in the xy plane are set to scattering boundaries, which are transparent to incident plane waves. This specific type of boundary condition is transparent for incident plane waves of any angle. For these boundaries to be perfectly transparent without inducing any reflections of the incident wave back, it is important to represent open boundaries. Finally, by employing periodic boundary conditions (PBCs) only a single unit cell of the metamaterial structure is required in order to simulate an infinite periodic array. For obtaining the transmission spectra the calculated field was sampled at a distance of two wavelengths (corresponding to the minimum frequency) from the metamaterial array and over an area equal to the unit-cell size.

There are two types of errors introduced by the FEM numerical approach. First, the nature of computational techniques is such that the estimated solution is an approximation to the actual solution of the PDEs. Therefore, inherently, there is an error between the numerical and the actual solutions. This error depends on the number and the shape of the elements used as well as the geometry of the structure. By properly choosing the shape of the elements and their number we can minimise this type of error and efficiently solve our examined problem. In all simulations reported in this thesis, the number of elements used was such that the estimated solution did not change more than 1% by doubling the number of elements. In some cases needed, simulations were conducted with higher accuracy. Second, the calculations were conducted using fixed-point arithmetic [67]. The errors introduced by fixed-point arithmetic, however, were always much smaller than dictated by the required accuracy. Correspondingly, no further actions were taken to minimise these errors further.

## 2.5 Fabrication of Samples

Superconducting samples were fabricated from commercially available thin films of yttrium-barium-copper-oxide (bought from Theva Ltd.), known as YBCO, and niobium (bought from StarCryo Ltd.) using a standard photolithography technique. These films had typically thicknesses of 100nm to 300nm and were deposited onto sapphire substrates with thicknesses of 0.5mm or 1mm. The films were initially cleaned and then spin-coated with an appropriate photoresist. Depending on the thickness of the resist layer required and the percentage of the superconducting material to be etched, either SU8 or S1813 were used. More precisely, SU8 (S1813) was used in cases that only a small (the largest) part of the film had to be etched. To transfer the sample pattern onto a superconducting film, the photoresist layer was first exposed through an appropriate photomask to UV light for a certain duration of time. The time of the exposure depends on the photoresist used and the power density of the lamp (for us 15mW/cm$^2$) and in our case was $\sim$ 7.4s for S1813 of a thickness of 1.35$\mu$m (corresponding to an absorbed energy density of 110mJ/cm$^2$) and $\sim$ 5.3s for SU8 of 2$\mu$m thickness (corresponding to an absorbed energy density of 80mJ/cm$^2$). Then, by placing the photoresist-covered sample into MIF (PM-acetate) for approximately 1min the (non) exposed parts of the S1813 (SU8) layer were removed and the (complimentary) structure of the photomask emerged on the photoresist's layer. Finally, a dry etching technique was applied to remove the parts of the superconducting film not covered by the photoresist.

Dry etching was accomplished with ion beam milling. In simple terms, ion beam milling can be described as an atomic sand blaster. In place of actual grains of sand, sub-micron ion particles are accelerated and bombard the surface of the target-sample, which is mounted on a rotating table inside a vacuum chamber [68]. Although, the resist protects the underlying material during the etching process (which in our case lasted typically 50mins for Nb and 22mins for YBCO), everything that is exposed to ion beam will be removed in the course of the process, including the photoresist. The key however is that the photoresist layer because of its thickness and etching rate (which can be lower than that of the targeted material) is adequate to protect the parts of the sample covered by it. So when the process is complete, these parts remain unaffected, defining the required pattern. The sample is finalised by removing the remaining photoresist

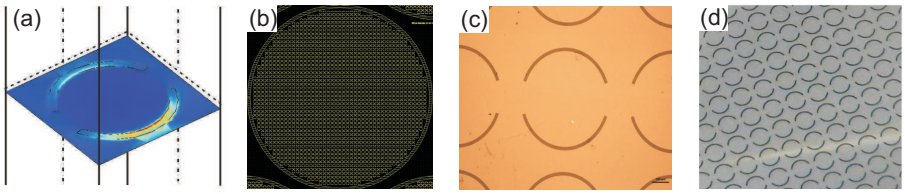


**Figure 2.8:** *Different stages in the design of a metamaterial sample: (a) simulating the structure in Comsol, (b) creating a photomask with the relevant metamaterial array, (c) characterising the sample during the fabrication process with an optical microscope, and (d) a photo of the actual fabricated sample.*

by placing the sample in ultrasonic bath with acetone several times for 15 mins each, followed by 15mins in IPO, and 15mins in distilled water.

It has to be stated that at every stage of the process described above, several characterization tools were used to assess the quality of the structure being fabricated. Those included a mechanical surface profiler for fast initial characterisation of the sample, which was able to produce a 2-Dimensional cross-section of the surface along a specific direction. Additional accurate measurements were conducted with a 3-Dimensional Surface Profiler able to recreate 3D maps of the sample's surface. Especially the 3-Dimensional Profiler was a Zescope Profiler able to characterise surfaces with vertical scanning interference microscopy [69]. This technique offers the capability to measure micro-surface map height variations to within 0.01nm repeatability, which is comparable to high-end optical profilometers. ZeScope's measurements capture up to 1.3 million points of surface detail; this is amongst the highest spatial sampling rate of any standard optical profilometer. Using ZeScope allowed us to perform 3D mapping of our samples with unprecedented accuracy.

## 2.6 Testing the Validity of a Hypothesis

Up to this point, we have discussed about experimental equipment and procedures, theoretical methods, and numerical experiments as well as fabrication and characterization techniques. All these topics are not independent, but rather form different stages of the hypothesis testing procedure, which is the driving force that underlies research

in physics.

It is with these thoughts in mind that the work reported in this thesis was conducted. Initially, we tested whether it is possible to show an effect by using a specific structure. Many times a valid model of the structure had to be created that accounted for all its relevant properties. Then, simulations played a central role in defining a suggested structure design. Once a design was reached, such that with certain confidence the desired effect could be shown, the structure was fabricated and measured. As a result, either the initial hypothesis was validated (which was the desired outcome) or information was extracted that was used to improve the model considered. These improvements were then reflected on new designs. All the steps were repeated until solid understanding was acquired. In some of the cases, simple analytic models that provide qualitative understanding were also produced. The various steps of this procedure are reflected on the sample design illustrated in Fig. 2.8, ranging from a simulation of a metamaterial unit-cell and the design of a photomask for the fabrication of superconducting samples to the characterisation of the produced samples.

It has to be stated, though, that compromises exist in every step. The fabricated structure might differ from the idealised theoretical model and a trade off had to be made between what was desired and what was possible to fabricate. Luckily, experiments sometimes offered us the ability to "trick" our uncertainty about specific parameters by experimenting several times with different structure designs.

# 3

# Manipulating THz Radiation

In this chapter, our approach regarding the manipulation of THz waves is presented. As we have mentioned in the introductory chapter, the lack of natural materials that are able to interact efficiently with the electric or magnetic components of THz waves poses a great obstacle in THz-radiation investigation and exploitation. The emergence of the field of metamaterials came in time to offer ways to interact with these waves, leading to many potential devices, ranging from antenna designs to filters, absorbers, and modulators.

The approach presented here is based on using superconductors as the ultimate low-loss conducting component of our metamaterial structures. More precisely, this chapter examines the possibility of superconductors to have a significant contribution in the field of metamaterials, since they offer the potential both for a dramatic reduction of losses and for active control of the metamaterials' response. We believe that the unique properties of superconductors, emanating from their macroscopic quantum nature, could add a new dimension to the concept of metamaterials, substantially expanding the range of their functionality and applications.

The chapter starts with a brief introduction to the topics of metamaterials, in general, and superconducting metamaterials, in particular, and continues with presenting the results on metamaterial designs and hole array structures patterned on niobium (Nb) and high temperature yttrium-barium-copper-oxide (YBCO) superconductors.

## 3.1 Introduction to Metamaterials

Metamaterials are artificial composite media structured on a size scale smaller than the wavelength of the external stimulus radiation. Whereas conventional materials derive their electromagnetic characteristics from the properties of atoms and molecules, metamaterials enable us to design our own "atoms" (so-called meta-atoms), offering virtually unlimited control over the electromagnetic waves they interact with.

To illustrate how metamaterials respond to electromagnetic (EM) waves better, we first examine the natural atoms that are combined in lattices in order to form matter. The atoms in a lattice can be seen as a collection of small resonators, with specific resonant frequencies and damping factors. The response of a natural material to an incident wave is defined by the collective (i.e., volume-averaged) response of all such 'atomic' resonators excited by the wave [70, 71] (see Fig. 3.1(a)). However, the limited choice of existing atoms forming the natural materials provides a restricted amount of options for the materials' responses to the excitation waves (e.g., the refractive index is always non-negative). Interestingly, an electromagnetic wave is "short-sighted", in the sense that it is unable to resolve objects in distances separated by less than a fraction of its wavelength (i.e., the diffraction limit). This diffraction-limited behaviour of the wave enables us to structure the response of a material to the incident radiation by designing its effective atoms, the size and shape of which depend on the targeted frequency region and the desired response, as shown conceptually in Fig. 3.1(b). The design of these structural units is limited only by our imagination and our fabrication capabilities, which gives metamaterials the potential to open a gateway to exotic electromagnetic properties and functionality unattainable in naturally occurring materials. The latter is reflected by the word 'meta', which in Greek means 'beyond', implying that metamaterials take us further than natural materials would allow.

Metamaterials can be considered as the next generation of artificially structured media, such as photonic crystals [73] or frequency selective surfaces [74]. However, in contrast to the latter media, metamaterials are usually non-diffracting, since their meta-atoms are placed in a periodic lattice with sub-wavelength distances. Hence, as far as the excitation wave is concerned, in most of the cases, metamaterials can be considered as homogeneous media described by the effective electric permittivity

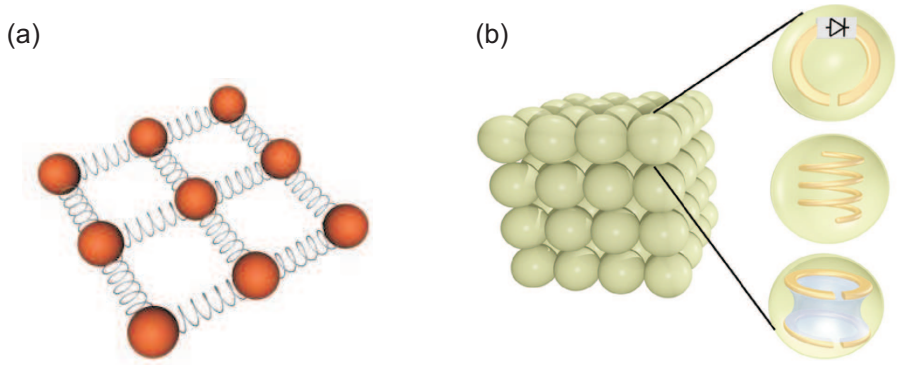


**Figure 3.1:** *Artistic illustrations. (a) Atoms combined in a lattice that forms matter could be seen as a collection of small resonators that interact with each other (not necessarily coherently). (b) In a metamaterial, we can design our own atoms -EM resonators- controlling the effective response of the artificial crystal to the incident radiation [72].*

$\varepsilon$ and the magnetic permeability $\mu$. Both $\varepsilon$ and $\mu$ are controlled by the size and the geometry of the meta-atoms, and the properties of the constituent materials. The first metamaterials were, perhaps, two-dimensional and three-dimensional arrays of metallic rods responding to microwave radiation as homogeneous materials with index of refraction less than one [75] or negative effective electric permittivity [76].

The surge of interest in the field of metamaterials was triggered by a paper published by Sir John Pendry [77], in which he proposed how to build materials with artificial magnetic response based on an old idea by Hardy and Whitehead: the use of split ring resonators (SRRs) [78] as a special type of meta-atoms. This work led to media able to show magnetic resonances at frequencies ranging from microwaves up to the optical part of the spectrum [79]. It was very soon afterwards that David Smith and his colleagues fabricated and experimented with a metamaterial formed by arrays of metallic wires and split ring resonators (Fig. 3.2(a)), which was able to show simultaneously both negative magnetic permeability and electric permittivity [80]. This work was accepted by the scientific community both with sceptism and great enthusiasm, since it was paving the way towards engineering materials that can show negative refractive indices, a property first considered in the theoretic work of Veselago back in 1968 [81]. In 2001, such an artificial negative-index material was indeed designed and successfully tested in the microwave region [82].

Demonstrating negative indices of refraction had very interesting implications for the field of optics: Pendry in 2000 [83] proved that a slab of a medium with the

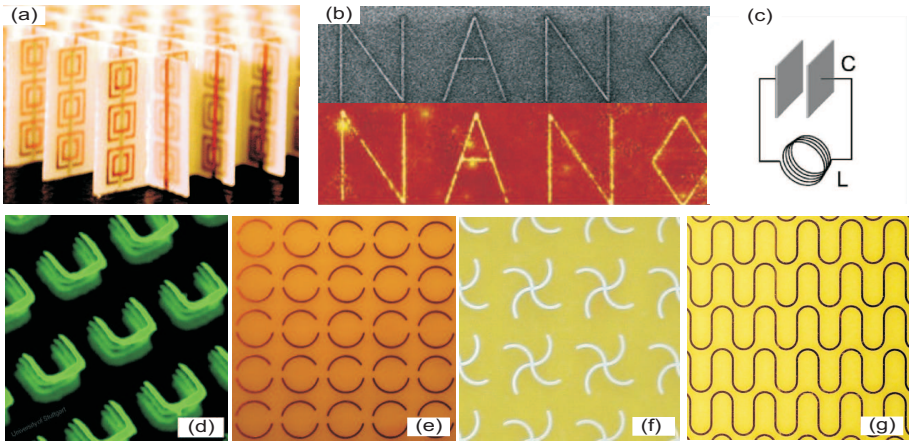


**Figure 3.2:** *First (a) negative-index metamaterial [82] and (b) demonstration of super-resolution [87]. (c) Equivalent LC circuit for Split Ring Resonators (SRRs). Metamaterial arrays of various different meta-atoms such as (d) single and (e) double SRRs, (f) crosses, and (g) fishnets.*

refractive index equal to -1 can act as a perfect lens. Such a lens is not limited by diffraction (Fig. 3.2(b)), thus, it allows light to focus on arbitrarily small spots. In addition, researchers realised that their ability to create materials with any combination of effective parameters $\varepsilon$ and $\mu$ allowed them to guide electromagnetic waves in a predefined root, thoughts that led to the field of transformation optics [84,85]. It would be hard to dispute that the biggest dream of the metamaterials community in the field of transformation optics is the realisation of an electromagnetic cloaking device [86]. While many of the first results on negative refraction, superlensing, and transformation optics were obtained in the microwave regime, the interest started moving towards achieving similar effects at higher frequencies, i.e., in the infrared and visible parts of the EM spectrum. Already, there have been several reported approaches on how to achieve, e.g., materials with refractive indices equal to -1 and electromagnetic cloaking devices at optical frequencies [87, 88].

Up to now, the effort placed to experimentally verify the theoretically predicted effects gave a large boost to the development of the field of metamaterials, given their immense importance for many technological areas such as imaging, lithography, microwaves and optics industry, and data storage. Most importantly, though, as the field of metamaterials became more mature, the scientific community turned its attention towards broader applications of the field's achievements, covering the areas

of communications, information processing, and sensing. Such applications required the development of active metamaterials, next generation artificial media with electromagnetic properties that can be controlled dynamically. Consequently, switchable and amplifying metamaterials, and even highly nonlinear and quantum ones [18] have been engineered through hybridizing the fabric of the metamaterial structures with carbon nanotubes [89], graphene [90], phase change materials [91] or micro-electro-mechanical (MEMs) elements [92]. These works are excellent examples of how metamaterials can serve applications for which current solutions are either inefficient or non existent and help to transform the field of metamaterials from the state of pure academic research to an application-driven field. Actually, this thesis aims to aid this transformation by proposing efficient metamaterial solutions for manipulating sub-THz (millimetre-waves) and THz radiation.

## 3.2 Challenges and Prior-Art in Metamaterials

The exotic and often dramatic physics predicted for metamaterials is underpinned by the resonant nature of their response and, therefore, achieving strong resonances (i.e., resonances with high-quality factors) is essential in order to make metamaterials performance efficient. However, losses are one of the most fundamental problems in these structures, since they can damp or even completely extinguish the metamaterials' resonant response. This problem can be so big that losses are often pointed out as the main reason for the commercial inapplicability of metamaterials. Thus, reduction of losses is the first great challenge that we have to resolve and is necessary in order to achieve high-quality resonances. The second challenge is related to the dynamic control of metamaterials' response. Achieving tunability in metamaterial structures is of great importance in order to enable the use of these structures in active devices. In this section, we will discuss each one of these two challenges in greater detail.

We start by examining the issue of losses in metamaterials. As stated earlier, the metamaterial resonant response is determined by the behaviour of the meta-atoms, the most common types of which are split ring resonators (SRRs), fishnet structures, cut wires, etc. [77,93,94]. Fig. 3.2(c) shows an electric analogue of an SRR, while Fig. 3.2(d-g) present different types of meta-atoms that show resonant behaviour. More precisely,

Fig. 3.2(d) shows a metamaterial array of modified SRRs for operation in the optical regime, Fig. 3.2(e) a metamaterial array of rings with two splits, Fig. 3.2(f) a metamaterial array of crosses as meta-atoms, and Fig. 3.2(g) a fishnet metamaterial structure. Although in some cases the resonant response of metamaterials can be enhanced (or modified) by the interaction between the meta-atoms [95], their characteristics are mainly controlled by the dielectric properties of the constituent materials and the geometry of the meta-atoms. Thus, the first serious limitation comes from the fact that the constituent materials (metals especially) have intrinsic losses which tend to increase as the frequency of the metamaterial's resonance shifts from the microwave towards the optical part of the spectrum. In the case of metals, this happens because they exhibit resistance to oscillating electrical currents (Ohmic losses), which becomes stronger at frequencies approaching the visible part of the spectrum. In addition, a second limitation is imposed by the geometry of the meta-atoms. The resonant elements of the metamaterial array, depending on their geometry, can be strongly coupled to free space and, therefore, suffer from significant radiation losses, known also as scattering losses.

In order to present efficient ways to deal with the losses issue in metamaterials, let us start by focusing on the most celebrated example of a meta-atom, which is the metallic split-ring resonator (SRR) [77, 78] and its variations presented in Fig. 3.3. Since the meta-atom size is much smaller than the wavelength (i.e., when we are in the electrostatic region), an SRR is just a small LC circuit formed by an inductance L and a capacitance C. Indeed, the ring corresponds to one winding of a coil (the inductance), while the split of the ring produces a capacitor. Such a circuit becomes resonant at a frequency of $f_{\text{res}} = \frac{1}{2\pi\sqrt{LC}}$. For instance, Fig. 3.3(a) shows an array of SRRs optimised for operation in optical frequencies, while Fig. 3.3(b) presents the LC circuit analogue of the SRR meta-atom [79]. However, resonances' quality-factors (Q-factors), which is the resonant frequency over the width of the resonance and expresses the ability of a resonator to store energy, demonstrated by conventional SRRs are often limited to small values at frequencies higher than a few GHz. This happens since in arrays of SRRs at these frequencies both Ohmic and scattering losses are high. Therefore, the Q-factor of the resonance can be enhanced by reducing Ohmic losses, scattering losses, or both.

We start with the reduction of scattering (radiation) losses that can happen through

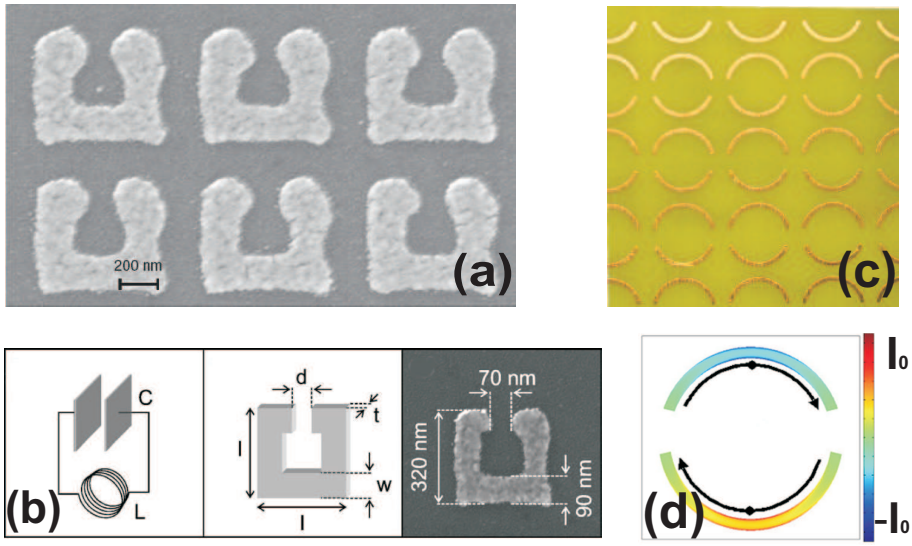


**Figure 3.3:** *(a) Photonic SRRs [79]. (b) LC circuit analogue of an SRR meta-atom [79]. (c) Microwave metamaterial array of ASRs [96]. (d) Current distribution in ASR at trapped mode resonance. The currents in the two parts of the ring have opposite phase.*

changing the geometry of the ring. In larger meta-atom designs, where the electrical length of the conducting features is comparable to a fraction of the wavelength of the excitation, we can talk about geometrical resonances [97]. In the case of meta-atoms with conducting elements of these sizes, each conducting element can support a standing wave of surface current bounded to it, when its length is equal to a multiple half of the wavelength of the surface mode[1]. Such a behaviour qualifies meta-atoms as electromagnetic resonators.

Previous work of our group, has showed that achieving high-Q resonances by minimizing scattering losses is possible when meta-atoms with geometrical resonances are used. This is possible by introducing certain small asymmetries in the shape of the meta-atoms that can lead to the design of asymmetric split rings (ASRs) [96]. Such a design is depicted in Fig. 3.3(c). Each ring has two equal splits dividing them into pairs of arcs of different length. The structural asymmetry can lead to the excitation of the antisymmetric current mode in the two arcs of the ring (see Fig. 3.3(d)). More precisely, the arcs have closely spaced resonant frequencies due to the small difference in their length. Since the phase of the current oscillations near the resonance changes rapidly, it becomes possible to achieve 180° phase mismatch between the current modes

[1]Note that these standing current waves are actually weak plasmonic modes (see Chapter 4).

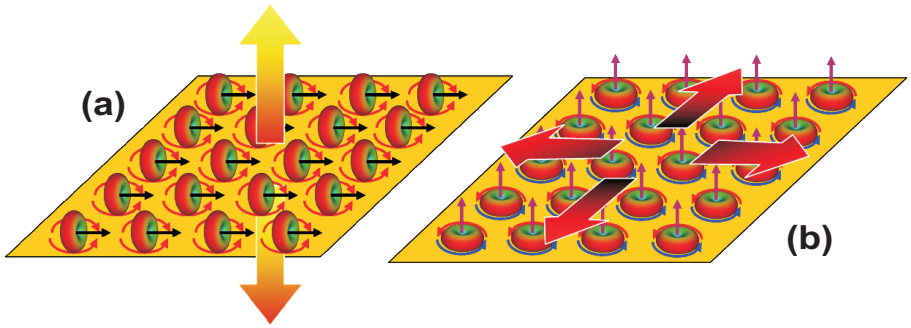


**Figure 3.4:** *(a) When the two arcs of the split ring are of equal length, a symmetric current configuration is supported. A symmetric current mode in ASR arrays leads to strong scattering and subsequent radiation losses as a result of constructive interference between the radiation of the two arcs. Thus, a low-Q dipole resonance is formed. (b) If the symmetry of the split-ring is broken by introducing a difference in the arc length, an anti-symmetric current configuration becomes accessible. The counter-propagating currents radiate fields that interfere destructively, eliminating scattering. Due to the small difference in the arc lengths, a weak only electric dipole is excited. In addition, the strong magnetic dipole mode formed due to the antisymmetric current configuration leads to no scattering outside the plane of the array, resulting in high-Q trapped mode resonances.*

excited in each arc in between their very-close resonant frequencies. Thus, an antisymmetric mode is formed by standing current waves in the short and long arcs oscillating with opposite phases.

In the case of arcs of equal length a symmetric current configuration is supported that leads to strong scattering as a result of the constructive interference between the radiation emitted by each arc (see Fig. 3.4(a)). However, the antisymmetric current mode that can be established in the case of arcs of almost equal lengths allows the radiated waves to interfere destructively, leading to a very weak electric dipole scattering in the far field (see Fig 3.4(b)). This is because, in reality, the antiphase currents always have slightly different amplitudes due to the difference in the arc lengths, which leads to a small but finite amount of radiation losses. Furthermore, the antiphase current mode corresponds to a magnetic-dipole moment oriented normal to the plane of the array. In a regular array, all such dipole moments oscillate in phase and can scatter only in the plane of the array, effectively trapping the radiation in the form of surface waves (Fig. 3.4(b)). As a consequence, this resonant current mode (which is termed trapped mode) exhibits vanishing radiation losses and can lead to a very sharp Fano-type resonance.

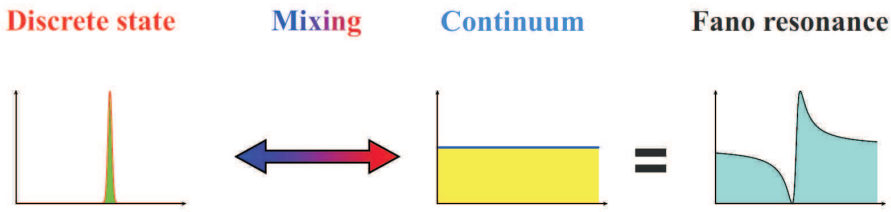


**Figure 3.5:** *Illustration of the Fano resonance as a superposition of the Lorentzian line shape of the discrete level resonance with a flat continuous background process [98].*

In physics, a Fano resonance is a type of resonant scattering phenomenon that gives rise to an asymmetric line-shape. Actually, a Fano resonance is created due to the interference between a background and a resonant scattering process resulting in an asymmetric line-shape. It is named after the Italian physicist Ugo Fano who gave a theoretical explanation for the appearing sharp asymmetric peaks in the absorption spectra of noble gases firstly observed by Beutler. Thus, the explanation of the Fano line-shape initially appeared in the context of inelastic electron scattering by helium and autoionization (i.e., a process by which atoms spontaneously emit one of the shell electrons, thus going from a state with charge $Z$ to a state with charge $Z+1$). An incident electron doubly excites a helium atom to the 2s2p state. Subsequently, the doubly excited atom spontaneously decays by ejecting one of the excited electrons. Fano showed that interference between the amplitude of simply scattering the incident electron and the amplitude of scattering via autoionization creates an asymmetric scattering line-shape around the autoionization energy with a line-width very close to the inverse of the autoionization lifetime. Following Fano's discovery, there have been a great number of studies devoted to Fano resonances in various quantum systems, such as quantum dots, nanowires and tunnel junctions. For an interesting perspective on Fano resonances we refer the reader to a recent review [98]. In general, the microscopic origin of the Fano resonance arises from the constructive and destructive interference of a narrow discrete resonance with a broad spectral line or continuum, as shown in Fig. 3.5. This leads the Fano resonance, in contrast to a Lorentzian resonance, to exhibit a distinctly asymmetric shape with the following functional form [99]:

$$I \propto \frac{(F\gamma + \omega - \omega_0)^2}{(\omega - \omega_0)^2 + \gamma^2}, \tag{3.1}$$

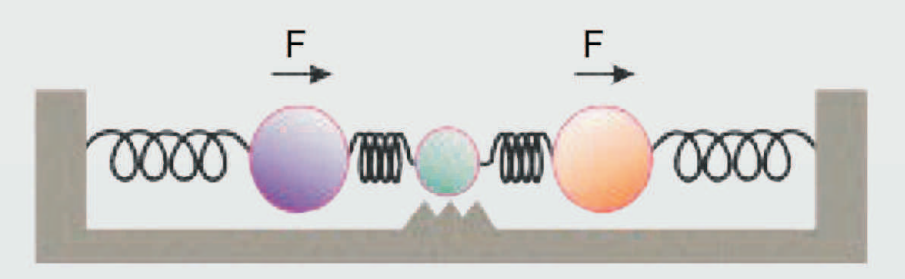


**Figure 3.6:** *Mechanical analogue of the ASR metamaterial. Each arc of the ring is represented by a large mass oscillator coupled to a small-mass, which is subject to friction corresponding to scattering losses. At a narrow frequency range, the large masses oscillate with opposite phases leaving the small mass immobile, hence reducing dissipation [100].*

where $I$ is the spectral response of a system and $\omega_0$ and $\gamma$ are standard parameters that denote the position and width of the resonance, respectively; F is the so-called Fano parameter, which describes the degree of asymmetry. The Fano resonance was initially regarded as a feature entirely specific to quantum systems. However, wavefunction interference phenomena are also ubiquitous in coupled resonating systems in classical physics [99].

In ASRs, the interference between the two resonant modes (the strong non-radiating magnetic-dipole moment and the weak radiating electric-dipole moment) leads to the typical asymmetric line-shape of the Fano resonance. Therefore, in the absence of Ohmic dissipation, scattering (radiation losses) is the only loss mechanism. According to a mechanical analog of the asymmetrically split-ring metamaterial suggested by V.A. Fedotov, each arc is represented by a large-mass oscillator coupled to a small-mass, which is subject to friction corresponding to scattering losses (see Fig. 3.6). At a narrow frequency range, the large masses oscillate with opposite phases leaving the small mass immobile, hence reducing dissipation [100]. Therefore, it becomes clear, through the presented theory, that minimization of the residual scattering losses and maximization of the Q-factor can be achieved in metamaterial arrays of ASRs by minimizing the asymmetry between the arcs of each ring which results in a weaker remaining electric-dipole radiation. However, a slight asymmetry should always exist between the arcs of each ring in order to allow the excitation of this mode on the ASR array by the incident EM wave (i.e., on a ring of symmetric arcs such a mode is not radiating, and thus, it cannot be excited by an incident electromagnetic field).

However, as the frequency increases above a few GHz, Ohmic losses of metals cannot be neglected and become a problem even in the millimetre-wave and THz parts of the spectrum. At millimetre-wave frequencies, one should also take into account the dissipation losses in the dielectric substrate and/or superstrate of the structure. Considering the problem of dissipation losses, the solutions often proposed include more elaborate designs of meta-atoms [101], hybridizing metamaterial fabric with gain media such as quantum dots [102], or the search for new low-loss materials among metallic alloys and conductive metal oxides [103], as well as the use of metals at cryogenic temperatures [104].

Apart from resolving the losses issue, active control of the metamaterial resonances is of great importance as well. In order to engineer metamaterials with the necessary functionality so that they can be used in active photonic devices, we should be in ability to tune and modulate their response. Designing a metamaterial that shows resonant behaviour at a specific frequency is feasible and sometimes trivial, but controlling its properties dynamically is challenging. This can be achieved by changing the shape or size of the meta-atoms or the dielectric properties of the constituent materials. Changing the shape/size of meta-atoms requires structural deformation of the latter by applying an external stimulus such as current [105, 106] or by changing the temperature [92], while changing the dielectric constant of the constituent materials is also possible through engaging phase-change [91], piezoelectric [107], or Kerr (e.g., with the use of liquid crystals) phenomena [108]. Another option is to take advantage of the strong optical nonlinearity of graphene layers [90] or fullerenes [89] integrated into the metamaterial structure, or by introducing these nonlinearities locally in the form of lumped circuit elements such as diodes or varactors in the metamaterial arrays [109]. The extent of spectral shift, amplitude and speed of modulation depends on the approach used.

Our approach to the development of metamaterials for the millemetre-wave and THz parts of the spectrum is based on replacing metals with superconductors, which allows us to address both the challenge of losses and of dynamic control of our structures.

## 3.3 Our Work in the Frame of Superconducting Metamaterial Research

The first superconducting[2] metamaterials were demonstrated in 2005 by the group of Steven Anlage [110]. They were composed of arrays of double-SRRs made from yttrium-barium-copper-oxide (YBCO) and niobium (Nb) films and were designed to operate in the waveguide environment at microwave frequencies. Fig. 3.7(b) and (c) show such a metamaterial array of double SRRs made of Nb film and a meta-atom structure of this array, respectively. Although the reported measurements suffered from strong noise and showed multiple resonances due to imperfections in the fabrication of the superconducting rings, those first demonstrations confirmed that higher resonance quality factors could in principle be achieved through the reduction of the surface resistance in superconductors compared to metals such as copper (see Fig. 3.7(a)). Furthermore, temperature was identified as a one of the possible means of controlling the response of such metamaterials. In a later experiment reported by the same group in 2007 [111], the possibility of tuning the resonance of the superconducting metamaterials via DC and RF magnetic fields was clearly shown. Both the quality factor of the metamaterial resonance and its frequency were affected by the applied field. The control of the metamaterial response could also be achieved by illuminating the superconducting structure with optical pulses [112] or by applying a DC current. The latter has been shown recently by Savinov et al. in [113]. The fact that the surface resistance of a superconductor can be readily altered by various types of external stimuli, makes the superconducting metamaterials very attractive for practical applications as active device components [114].

Furthermore, the quantum state of superconductors, which is described by a macroscopically coherent-phase wavefunction, gives rise to quantum interference and tunneling effects. Theoretical work has shown that due to quantum interference and tunneling effects in certain cases the electromagnetic response of SRRs can become quantized [116]. More precisely, RF superconducting quantum interference devices (SQUIDs), which consist of a superconducting ring interrupted by a Josephson Junction (JJ), are essentially quantum analogues of SRRs. When driven by an AC magnetic

[2] At this point, we encourage the reader without basic knowledge of superconductivity theory to refer to Appendix B for a brief introduction.

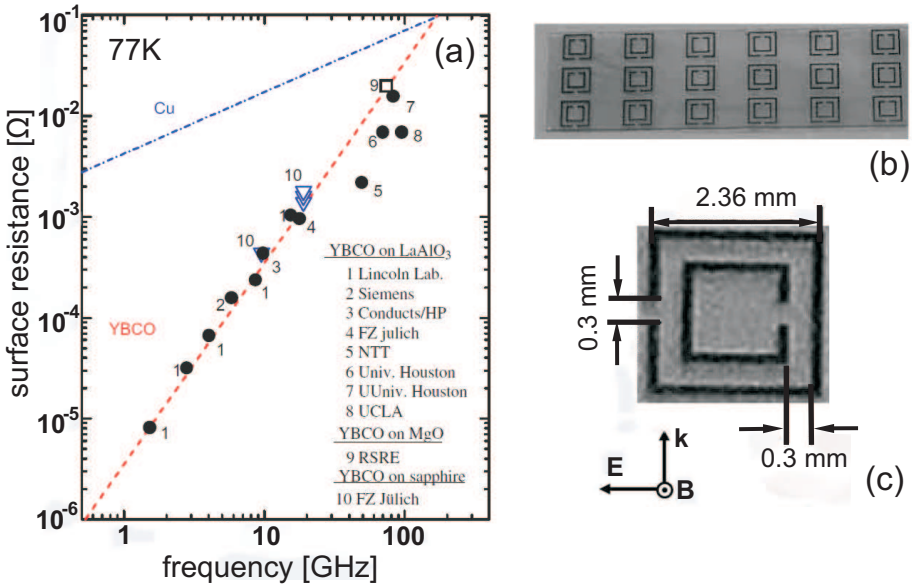


**Figure 3.7:** *(a) Surface resistance of YBCO films as a function of frequency measured by different research groups. Surface resistance of copper is plotted for comparison [115]. (b) Photo of the first superconducting metamaterial, an array of double SRRs made from YBCO film for operation at microwave frequencies around 10GHz. (c) A close-up view and the dimensions of the double SRR meta-atom [110].*

field, the induced supercurrents around the rings are determined by the JJ through the nonlinear Josephson relations [116]. Therefore, such systems exhibit very strong nonlinear behavior, including even chaotic effects, which implies that superconductors, in general, and Josephson Junctions, in particular, are ideal constituents of tunable meta-atoms due to the strong dependence of their inductance on magnetic field and temperature [117]. Such metamaterial structures offer the potential for use in extra sensitive sensors and quantum information-processing systems.

Our group was the first to develop and fabricate free-space superconducting metamaterials, the response of which has been measured in the sub-THz regime. These measurements have resulted in the demonstration of sharp Fano resonances in the sub-THz domain with metamaterial arrays consisting of ASRs made from high-$T_c$ YBCO films. The existence of the Fano resonances reveals also that patterning superconductors on a microscale does not affect their low-resistance (i.e, the superconducting) state. Furthermore, the ability to control efficiently these resonances with temperature was confirmed [118]. In addition, we were the first to report on the study of extraordinary transmission through an array of subwavelength holes made in a high-

$T_c$ superconductor film [119]. These pieces of our work are presented in the following sections of this chapter. Metamaterials and hole arrays made from low-$T_c$ Nb films were fabricated and measured as well. Finally, several attempts have been made to realise and experimentally verify the feasibility of SQUID metamaterials. Although these last experiments were inconclusive, they eventually led to the idea of a different type of quantum metamaterials exploiting the flux exclusion property of superconducting rings, as was recently proposed by Savinov et al. in [120].

Several other works on superconducting split ring metamaterials [121], [104] and rectangular hole arrays made in YBCO [122] with operating frequencies in the low-THz regime have followed. In essence, they all have confirmed the effect of switching the metamaterial resonance upon transition to the superconducting state and the enhancement of extraordinary transmission effect below the critical temperature.

Unfortunately, superconducting state is not energetically allowed at frequencies higher than several THz, since the interaction with photons provides electrons with enough energy to destroy their pairing (i.e., the Cooper pairs) and move them to the conduction band (refer to Appendix A). As a consequence, the existing superconductors cannot be used for designing low-loss infrared and visible-light metamaterials and alternative approaches should be sought by the researchers working in those domains.

## 3.4 Fano Resonances in Superconducting Metamaterials

We start with the presentation of the results on the first experimental study of free-space transmission through millimetre-wave (sub-THz) superconducting metamaterials.

A natural point to begin our study seems to be the examination of the response of an array of split ring resonators (SRRs). The SRRs have an inner radius of 92$\mu$m and an outer radius of 100$\mu$m, with a gap-size of 8$\mu$m and were made from a 300nm-thick niobium film. The film was deposited on a 0.5mm-thick circular sapphire substrate with a diameter of 30mm. The period of the array was 240$\mu$m. Fig. 3.8 (b) and (c) show a microscope image of a section of the array and a close-up view of a single Nb SRR, respectively.

The transmission spectrum of this metamaterial is shown in Fig. 3.8(a). Above its transition temperature ($T_c$), which is 9.2K, Nb behaves as a normal metal, suffering

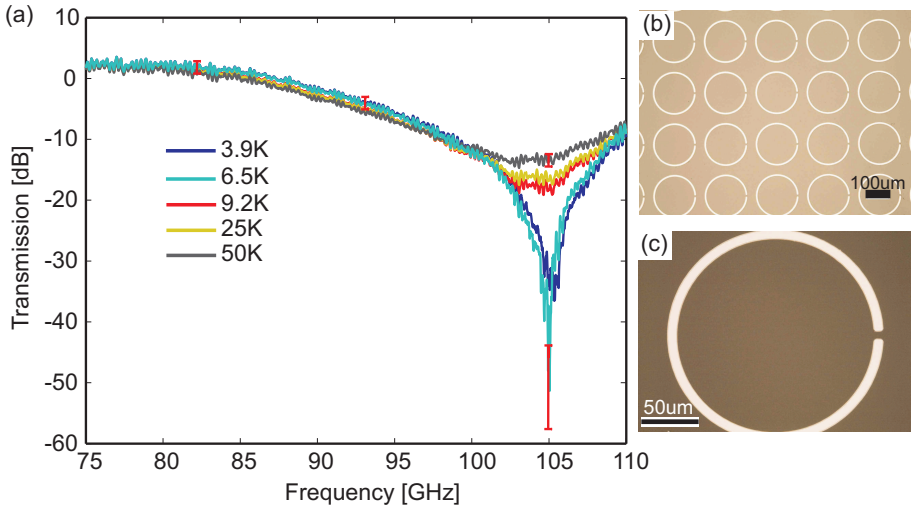


**Figure 3.8:** *(a) Measured transmission spectrum of a metamaterial formed by an array of Nb SRRs. The resonance of the structure at* $105\,GHz$ *is strongly enhanced below* $T_c = 9.2K$*. Red error-bars indicate the uncertainty level in the measurements. (b) A microscope image of a section of the array. (c) A close-up view of a single Nb SRR.*

from Ohmic losses created by the scattering of its electrons with the lattice and the impurities in there. The high Ohmic losses are the reason why there is only a very weak resonant behaviour shown in the transmission spectrum of the metamaterial structure for this temperature region. Upon transition to the superconducting state (below 9.2K), the Ohmic losses become significantly reduced, as Nb tends towards becoming an ideal conductor. The resonance of the structure at the frequency of 105 GHz becomes more pronounced, revealing a clear resonant response of the metamaterial SRR array. As the temperature decreases, the resonance also shifts towards higher frequencies. Similar results have been reported in [110], but there the measurements of the SRR arrays were conducted inside waveguides.

We have to note that the appearance of small-amplitude high-frequency ripples on the measured transmission spectra is the result of a systematic error in our experimental procedure. In Section 2.3 we have described in detail our experimental setup and the actions taken to minimize the errors involved in the measurements. Most importantly, due to the presence of reflecting surfaces (e.g., the windows of the cryostat) inside the first Fresnel zone of the propagating millimetre-wave radiation, multiple cavity modes are created leading to strong echo pulses that muddle the measured signal of the response of the sample. In Section 2.3 we have described the actions taken to

significantly attenuate these echo pulses (e.g., placing the windows of the cryostat at the Brewster angle). To further minimise the impact of the remaining echo pulses on our measurements we have applied filtering in the time-domain. In essence, the latter is equivalent to keeping only the main pulse that propagates through the sample and discarding all subsequent delayed pulses (which result from remaining cavity modes). However, this approach filters out also energy of the main signal that arrives with significant delay. Therefore, while we would like to filter out completely the echo pulses, such a choice would imply that a significant amount of power of the main signal would have to be discarded as well. As a result we have to accept a small error induced from the echo pulses, that results in the appearance of the small-amplitude high-frequency ripples in the measured data. In addition, calculations of the thermal noise level in the vector network analyser with a value of the IF filter at 100Hz (i.e., an averaging filter) place this value at $-87$dBm. Thus, thermal noise is not affecting our measured spectra since the received signal power was of the order of $-50$dBm to $-60$dBm in the worst conditions in all the conducted experiments. Therefore, the main source of uncertainty was the systematic error resulting from the remaining echo pulses. The magnitude of this error was calculated from the peak-to-peak amplitude of the observed ripples in the measured spectra. The impact of this error on the measured transmission spectrum of the Nb SRR array is shown with red error-bars for some representative data-points in Fig. 3.8(a) and its standard deviation ranges from 0.01 to 0.1 in linear scale for the normalised transmission spectrum shown in the same figure. Of the same order was the impact of this error in all the subsequent conducted measurements reported in this thesis. Finally, we need to mention that the measured spectra have a resolution of 21.8MHz, corresponding to 1601 equidistant measurement-points in the frequency range from 75GHz to 110GHz.

While by using superconductors the Ohmic losses are low, an array of SRRs is unable to achieve high-quality resonances. As we have seen in Section 3.2, in the electrostatic regime, the split-rings at the resonance-frequency act as LC resonators and suffer from large portions of radiation energy losses due to their strong coupling with the surrounding environment. In addition, due to their deep sub-wavelength size, SRRs are unable to provide large-volume confinement of electromagnetic fields, which is necessary to attain high-Q resonances. Therefore, the energy storage capacity of

each of these resonators is low despite the reduced Ohmic losses, leading to overall low-quality resonances. For example, the Q-factor of the resonance at $f_0 = 105$GHz for the Nb SRR metamaterial is below 15. However, achieving Q-factors typical for normal metamaterials made of metals (i.e., with Q$\sim$ 15) is no good, since that negates the the extra effort of fabricating these metamaterials with low-loss superconductors. We should not forget that a significant part of the motivation behind this work is the low-loss nature of superconductors compared to metals in the sub-THz range.

In order to achieve high quality resonances, we need to use a meta-atom design that is both larger in size and less strongly coupled to the surrounding space. The latter property will lower the radiation losses and, thus, enhance the lifetime of the resonant mode in the metamaterial structure. A meta-atom in the form of an asymmetrically split ring (ASR) appears to have both of the required properties, supporting the formation of Fano-type resonances, as we have already explained in Section 3.2.

Metamaterials exhibiting Fano resonances have recently attracted considerable attention owing to very sharp phase dispersion accompanying those resonances. The latter together with strong resonant response make such metamaterials ideally suited for slow-light [100,123,124], sensor [125], nonlinear [89], and switching [91] applications. Such resonances, as was explained, appear as a result of interaction between a high- and a low-quality excitation mode leading to asymmetric line profiles. In ASRs, for example, the antisymmetric current mode corresponding to a non-radiating magnetic dipole excitation couples to a strongly radiating and, therefore, low-Q electric dipole mode [96]. The lifetime of such a mode and the quality factor of the corresponding Fano resonance is controlled by the asymmetry of the splitting and in absence of dissipative losses can be made infinitely high. Therefore controlling Joule losses in real metamaterial systems is imperative for achieving ultra-sharp resonant response. The use of superconductors in this case, in principle, offers a practical way of completely eliminating Joule losses and even provides by far much greater temperature control over dissipation than in metals.

For manufacturing our superconducting metamaterial structures we purchased from Theva Ltd. 330nm-thick YBCO films deposited on 1mm-thick sapphire substrates via an intermediate 40nm-thick buffer layer of cerium dioxide ($CeO_2$). The maximum thickness of the YBCO film is defined by the thermal expansion mismatch between

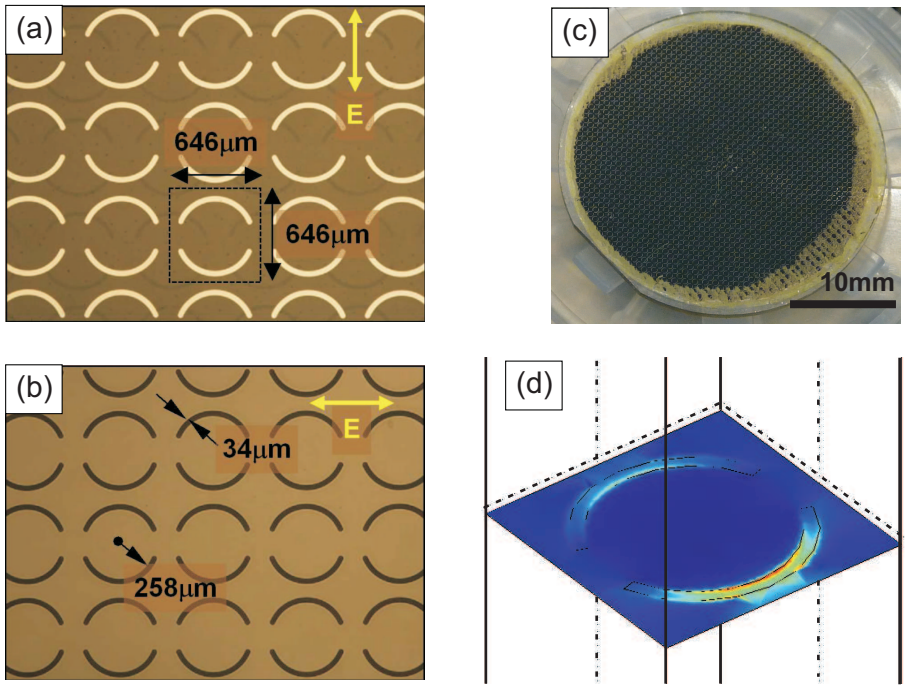


**Figure 3.9:** *Metamaterial arrays of ASRs made of YBCO: (a) Negative and (b) positive forms. (c) A photograph of the negative-form of the ASR metamaterial sample used in the experiments. (d) Modelling result for the current distribution resonantly induced in the positive-form of the ASR unit cell.*

the film and the substrate. Thicker films tend to relax stresses by cracking. These cuprate films become superconducting below a critical temperature $T_c \approx 88$K and are characterised by relatively large porosity with an average lateral size of the pores of about $1\mu$m. Due to enhanced vortex pinning (refer to Appendix A), such porous YBCO films have typically low surface resistance ($R_s(77\text{K}, 10\text{GHz}) < 300\mu\Omega$), and can support large critical currents ($J_c(77\text{K}) > 3\text{MA/cm}^2$), which makes them suitable for applications in high-Q microwave devices.

We studied both positive and negative forms of the asymmetrically split ring metamaterial, which were formed by square arrays of correspondingly circular wires and slits (apertures made in the cuprate film), as shown in Fig. 3.9(a) and (b). Each unit cell of the metamaterial arrays had the size of $646\mu\text{m}\times646\mu\text{m}$ and contained one pair of circular elements with the arc lengths corresponding to 140 and 142 degrees forming an ASR with the radius of $258\mu$m. Both positive and negative forms of the split ring resonators were wet-etched in the cuprate films following resist patterning with the use of e-beam lithography by our collaborators at the Rutherford Appleton Laboratory. The meta-

material arrays were 28mm in diameter and contained 1400 ASRs. Fig. 3.9(c) shows a photograph of the positive ASR metamaterial used for the conducted measurements.

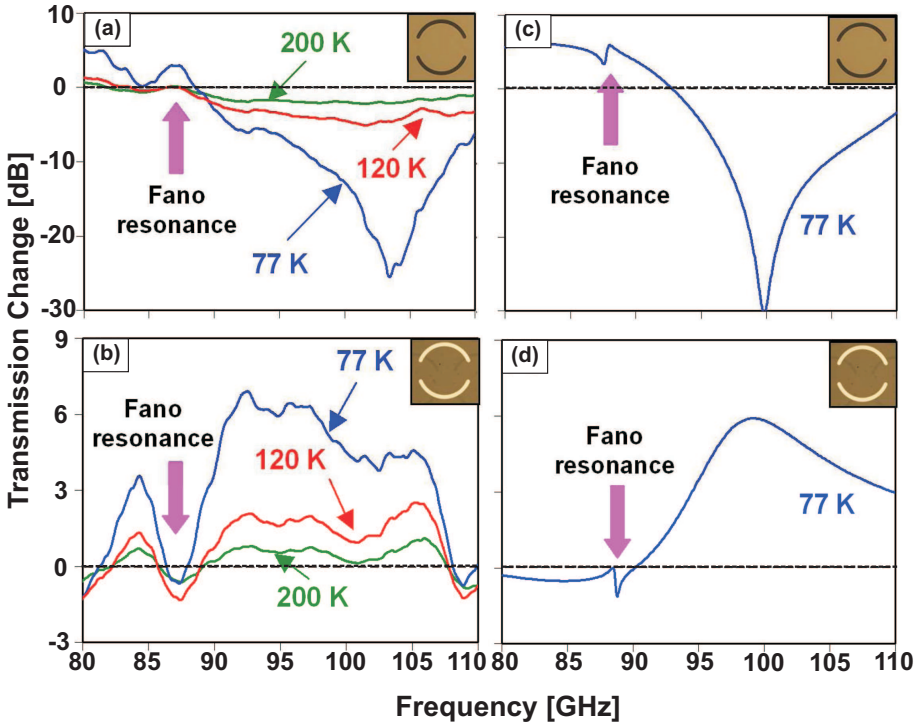


**Figure 3.10:** *Changes in transmission spectra of YBCO ASR metamaterial arrays relative to their room temperature state. Experimentally measured data -(a) and (b)- and simulation results -(c) and (d)- for positive and negative metamaterial designs, respectively.*

Transmission spectra of the cuprate metamaterials were measured in the $80 - 110$ GHz range of frequencies at temperatures above and below $T_c$ using the vector network analyser Agilent PNA-X 5242A and linearly polarised horn antennas. Free-space measurements were performed with the samples placed in the liquid nitrogen flow optical cryostat located between the antennas (for more details refer to Chapter 2). The frequency resolution was 21.8MHz corresponding to 1601 frequency-points between 75GHz and 110GHz. The polarisation of the incident wave was set parallel to the split for positive split rings and perpendicular to the split in the case of negative split rings, as indicated in Fig. 3.8(a) and (b), which was required for the excitation of the Fano resonances.

The results of the transmission measurements are presented in Fig. 3.10(a) and (b), where we plotted changes in the transmission spectra of the metamaterials with decreasing temperature (down to 77K) relative to their room temperature state. The mea-

sured changes clearly indicate the appearance of the Fano resonances at around 87GHz, which become substantially stronger as the YBCO film becomes superconducting. In the case of positive asymmetrically split ring metamaterial the resonance emerges as a peak in the transmission change spectrum corresponding to increased transmission (metamaterial-induced transparency [100]), while the complimentary (negative) version of the structure shows a pronounced dip corresponding to resonantly suppressed transmission, which fully agrees with the Babinet principle. Also, at frequencies away from this resonance, the complimentary metamaterial structures show gradual increase of the transmission levels with temperature for the negative structure and decrease of the transmission levels with temperature for the positive structure with the changes becoming most pronounced upon superconducting phase transition. The latter is illustrated in Fig. 3.11 for the case of negative metamaterial, where we plotted its temperature-induced transmission change observed at 84GHz. Similar to the case of the Nb SRR array, ripples of high-amplitude and high-frequency induced a systematic-error of standard deviation approximately equal to 1.0 for the normalised transmission in linear scale. The higher standard deviation of the systematic-error here compared to the SRR Nb reported measurements is attributed to the fact that the ASR metamaterial measurements were conducted with the liquid nitrogen cryostat for which no Brewster-angled windows were used (see also Section 2.3). The effect of the ripples was averaged-out by applying a moving-average filtering function of 100 points, which allowed the main trend of the response to show-up more clearly.

Apart from the experimental measurements, we have also conducted simulations of the metamaterials' response to sub-THz fields. In order to simulate a superconducting metamaterial we had to model the behaviour of a superconductor subjected to AC electromagnetic fields as a function of temperature and frequency. For this reason, we have used the two-fluid model (see Appendix A). Within the description of this model, the electrodynamics of a superconductor at nonzero temperature is determined by the existence of the two non-interacting currents; the current of purely inertial motion of Cooper pairs of electrons in the superconducting state, which we call supercurrent, and the current of normal electrons encountering scattering processes (for more details refer to Appendix A). Incorporating these currents in the derivation of the Drude model for the estimation of the relative permittivity for a frequency well-below the

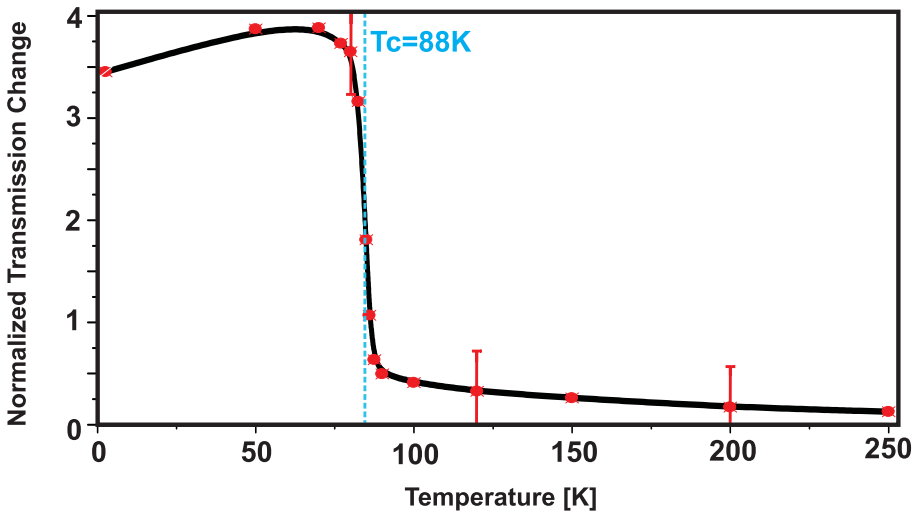


**Figure 3.11:** *Change of transmission measured at 84GHz as a function of temperature for negative superconducting YBCO metamaterial, relative to its room temperature state. Experimental data are presented by red dots, while black curve shows the trend and red error-bars indicate the uncertainty level in the measurements for some representative data-points.*

superconductor's gap frequency $2\Delta/\hbar$, where $\hbar$ is Planck's constant and $\Delta$ the necessary energy to break superconductivity, we have from classical theory (see Appendix A):

$$\varepsilon = \varepsilon' + j\varepsilon'' = 1 - \frac{\omega_s^2}{\omega^2} - \frac{\omega_n^2\tau^2}{\omega^2\tau^2+1} - j\frac{\omega_n^2\tau}{\omega(\omega^2\tau^2+1)}. \tag{3.2}$$

In the above equation, the second term represents the contribution of the non-dissipating supercurrent with plasma frequency $\omega_s = \sqrt{n_s e^2/m\varepsilon_0} = c/\lambda_L$, where $\lambda_L$ is the London penetration depth, $n_s$ the density of supercurrent carriers, $m$ the effective mass of the electrons, and $\varepsilon_0$ the dielectric constant in free-space. The third and the fourth terms account for the normal electron plasma with frequency $\omega_n = \sqrt{n_n e^2/m\varepsilon_0}$, with $n_n$ the normal electron density and $\tau$ their relaxation time. The ratio between the two densities $n_n$ and $n_s$ is defined through the empirical Gorter-Casimir relations, expressed by Eq. (A.25-26).

To get a feasible computational model for simulating our experiment with the commercial 3D FEM full-vector Maxwell equation solver Comsol Multiphysics, we followed the approach of modeling the YBCO layer as a surface impedance layer on top of the 1mm-thick sapphire layer. This approach was followed since the thickness of YBCO film (330nm) was many orders of magnitude smaller than the other dimensions of fea-

tures in the metamaterial simulation model and did not allow the film to be modelled as a separate material layer on its own. In microwave network theory the concept of surface impedance [55] is used to model a material with specific electric conductivity $\sigma$, permittivity $\varepsilon$, and magnetic permeability $\mu_0$. The surface impedance of a material with such parameters is $Z_s = \sqrt{\mu_0/\varepsilon\varepsilon_0}$. Therefore, having estimated, through the two-fluid Drude model, the permittivity of the YBCO film, we can estimate its surface impedance. It should be noted, however, that the thickness of the YBCO film is of the order of the London penetration depth, which implies that there is a small but existing radiation leakage through the film, introducing some error in describing the layer using the surface impedance boundary condition.

The values of the model parameters we used were $\lambda_L(0) = 150$nm, $T_c = 88$K, and $\varepsilon_{\text{sub}} = 10.4 - j0.004$ as the relative permittivity of the sapphire substrate. The temperature dependence for $\tau$ that decreases from $9.276 \times 10^{-12}$s (at 10K) to $1.047 \times 10^{-14}$s (at 300K) had been derived from published experimental data [126, 127].

The results of our simulations, which we present in Fig. 3.9(d) and Fig. 3.10(c) and (d) for the case of liquid nitrogen temperature, appear to be in a good qualitative agreement with the measured data and show the main features of the metamaterial response. Each metamaterial structure was modeled as a single unit cell subjected to periodic boundary conditions in the lateral dimensions (for more details refer to Chapter 2), which, given the size of the arrays, appears to be a good approximation for this type of metamaterials [128]. The simulations predict the appearance of the Fano resonance at around 87GHz, as shown, for instance, by the appearance of the antisymmetric current configuration established on the ring for the positive ASR metamaterial in Fig. 3.9(d). Although the position of the Fano resonances had been very well predicted by our model, the agreement between the simulated and experimental data was only qualitative. For instance, the amplitude and the width at the Fano resonance differ significantly in the case of both the negative and positive ASR metamaterial. The most pronounced difference is observed in the case of the negative ASR metamaterial at the transmission peak around 100GHz. While in the simulation a specific peak is observed, this is very broad and not so clearly pronounced in the measured transmission spectrum. We believe that the discrepancy can be attributed to the limitations of the surface impedance boundary condition approach mentioned above as well as to

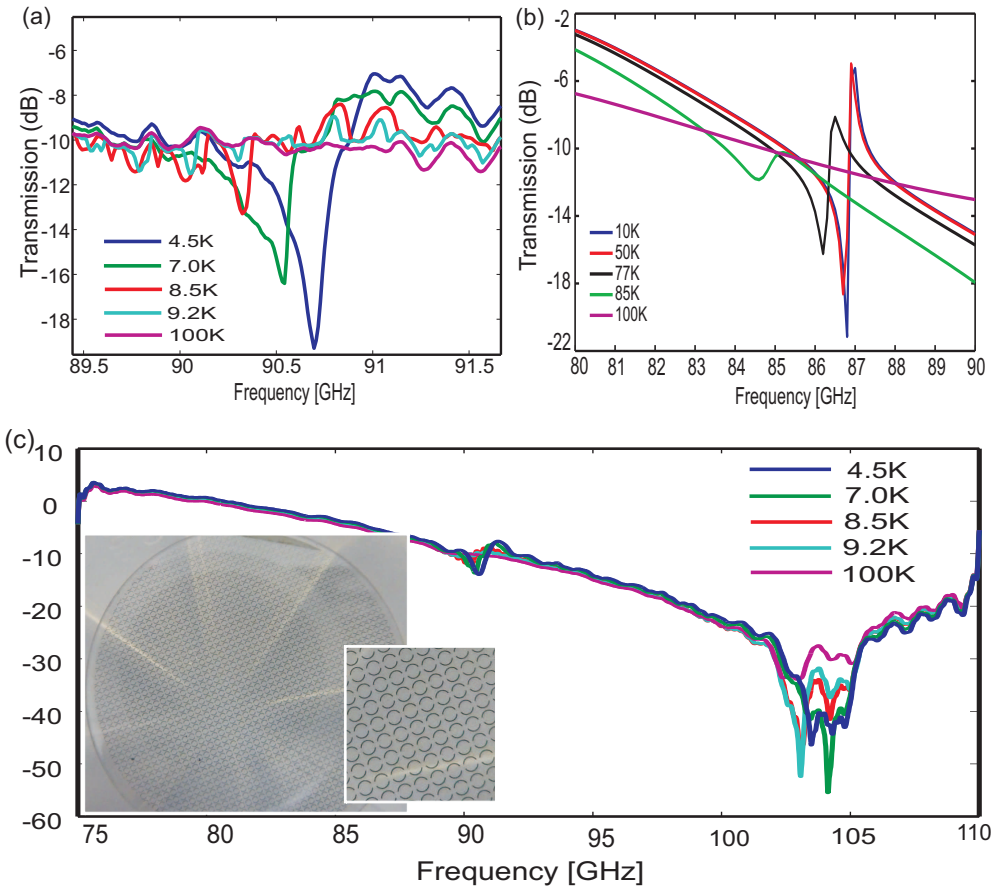


**Figure 3.12:** *(a) Experimentally measured transmission spectra of a Nb ASR metamaterial showing the development of its Fano-type resonance at various temperatures. (b) Transmission spectra measured at various temperatures above and below $T_c$ for the Nb ASR metamaterial array. The inset shows the photograph of the metamaterial. (c) Simulated transmission spectra of an YBCO ASR metamaterial (with the design parameters identical to that of Nb metamaterial) showing the development of its Fano-type resonance at various temperatures.*

the uncertainty involved in retrieving exact modeling parameters for high-$T_c$ superconducting films based on the available data in the literature. Also, photolithographic microstructuring of the YBCO films was likely to alter the superconducting state by affecting the films' porosity, and, therefore, could be another factor related to the discrepancy between experimental and simulated data. Finally, in the case of the negative ASR metamaterial structure a fabrication error has affected the measurements, leading probably to the observation of broader resonances.

We repeated those experiments with a positive-form metamaterial array of Nb ASRs. For fabricating this metamaterial structure we used a Nb film of 300nm thick-

ness deposited on 0.5mm-thick sapphire substrate. We periodically patterned the film using an ASR design, with the same parameters as reported for YBCO, except for the arc lengths, which were chosen to be 140 and 144 degrees respectively. Fig. 3.12(a) and (c) present the measured transmission spectra at various temperatures above and below $T_c = 9.2$K for this metamaterial. Upon superconducting transition we saw the formation of a weak Fano resonance, which was becoming more pronounced as the temperature decreased further. In addition, the resonance moved towards higher frequencies. This behavior is similar in trend to our simulation results (see Fig. 3.12(b)) for the Fano resonance formation of the YBCO ASR metamaterial as a function of temperature. Note that we just compare their trends, which should be similar since the macroscopic electromagnetic model is the same for both superconductors[3]. The observed blue-shifting should indicate a change in the real part of the permittivity of the superconductor, since losses have almost vanished in very low temperatures. This behaviour corresponds to a changing kinetic inductance for the superconductors and, in essence, points out to a possibility of exploiting superconductors as plasmonic media. The latter will be discussed in the next section.

In conclusion, we have demonstrated that structuring of YBCO and Nb films with metamaterial patterns preserve their essential superconducting properties that allows treatment of such structures as being made of low-loss conductors. We have provided the first experimental demonstration of Fano resonances in superconducting metamaterials made of cuprate YBCO and elemental Nb films and operating in the sub-THz range of frequencies between 75 and 110GHz. The strength of the resonances is controlled with temperature and increases dramatically as the temperature of the metamaterials drops below the critical point. At frequencies away from the Fano resonance, the complementary forms of the cuprate structures show a behaviour consistent with the Babinet principle. In particular, for frequencies higher than the Fano-resonance frequency the negative structure shows a gradual increase of transmission as a function of temperature, while the positive structure shows a gradual decrease of transmission as a function of temperature. In general, we expect that similar results apply to superconducting metamaterials operating at the THz domain, up to the gap frequency of the relevant superconductor. Therefore, our findings indicate that superconducting

[3]In this thesis we haven't conducted any simulations involving Nb superconductors.

metamaterials could form the bases of narrow-line THz and sub-THz tunable spectral filters for various security and sensor applications.

## 3.5 Extraordinary Transmission through Superconducting Hole Arrays

In 1944 Bethe, as part of his pioneering theoretical work [129], had calculated that the reduction in the intensity transmitted through a single hole of radius $r$, made in a thin perfect conductor screen, should be inversely proportional to $(r/\lambda)^4$ for wavelengths $\lambda >> r$. However, in 1998, Ebbesen was the first to observe very sharp peaks in the transmission spectra of arrays of sub-wavelength holes made in thin metallic films at optical frequencies [130] with the transmission efficiency at those maxima exceeding multifold the predictions allowed by the theoretical work of Bethe. This discrepancy between the predictions of Bethe and the experimental measurements obtained by Ebbesen brought a lot of attention on the field of extraordinary transmission, as it became known, and gave rise to many discussions regarding its nature. Since then, the extraordinary transmission phenomenon was seen in periodic [131] and quasi-periodic [132–134] arrays of holes in plasmonic metals [135,136], and in perfect conductors [137] that cannot support surface plasmons. These observations have stimulated a broad discussion on the role of dynamical diffraction, surface plasmons, and other evanescent waves and their interaction with Bragg peaks in the reciprocal space of the array in the effect [138,139].

Superconductors constitute a convenient platform for studying the effect of extraordinary transmission, since their electromagnetic properties can be switched from that of a lossy typical metal (normal state) to an ideal conductor (as $T \to 0$) (for more details refer to Appendix A). In between, they can appear as plasmonic materials[4], due to the negative real part of their permittivity and their low losses. Therefore, their dielectric properties can be dynamically changed through temperature, in order to emulate the different types of materials that have been used for the structures with hole arrays involved in studies of extraordinary transmission. Accessing these different regimes of

[4]The plasmonic nature of superconductors is going to be discussed in depth in the following chapter and interested readers are encouraged to refer there for a better understanding.

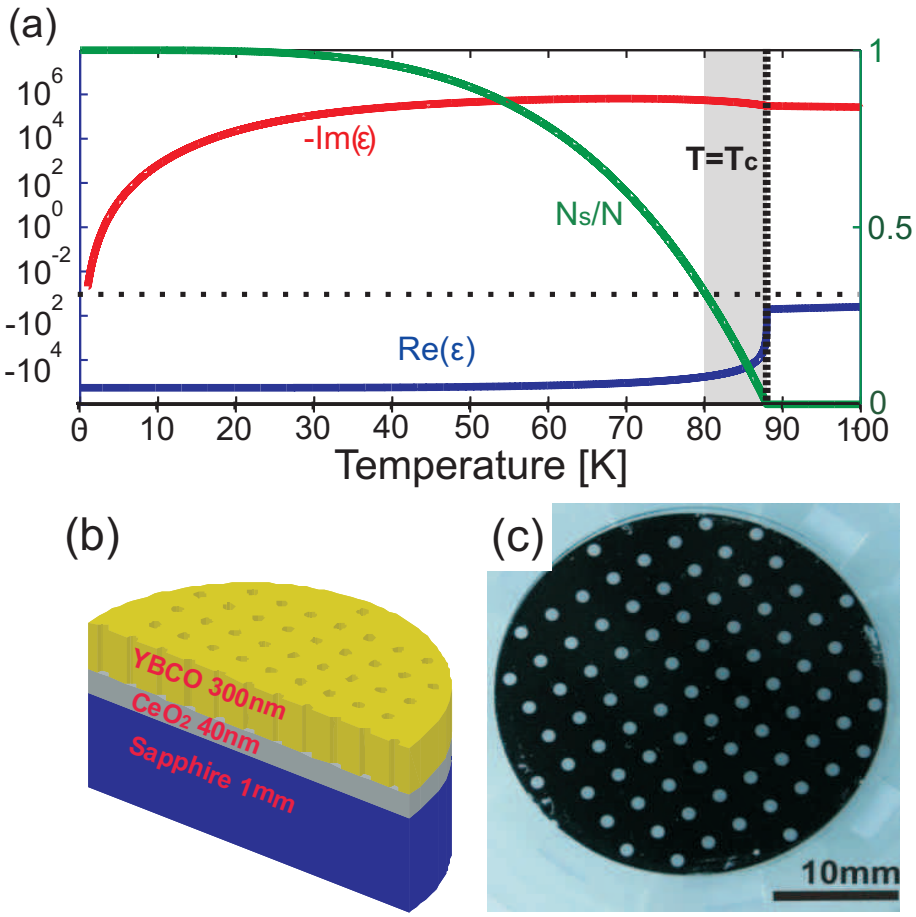


**Figure 3.13:** *(a) Theoretically estimated real (blue) and imaginary (red) parts of the relative permittivity of YBCO at 75 GHz as a function of temperature. The estimated density (green) of superconducting electrons Ns relative to the total density of electrons N is also shown as a function of temperature at the same frequency. (b) A cross-section of the sample's structure. (c) A photograph of the sample used in the experiments.*

superconductors' behavior, can happen with our free-space measurements experimental setup equipped with a liquid helium cryostat in between the antennas that allows us to accurately control the temperature of the superconducting sample (for more details refer to Chapter 2).

According to the definition of Yablonovitch and co-workers, the plasmonic regime is characterized by the dominance of the kinetic inductance over the Ohmic resistance and the Faraday inductance of a material [140]. In the microwave to millimetre parts of the spectrum, and especially in properly structured superconductors, the Ohmic resistance below superconducting transition temperature is negligible and the kinetic inductance only competes with the Faraday inductance. The ratio between the two is

controlled by the geometry of the superconducting structure and the temperature. By changing the geometry we can alter the Faraday inductance of the structure [140], while the dependence on temperature is easily understood if we resort to the two-fluid Drude model of superconducting response, which was considered in the previous section. From Eq. (A.27) it is apparent that temperature influences both the real and imaginary parts of the permittivity of a superconductor, altering its dielectric properties, and through that both its kinetic inductance and its Ohmic resistance.

Let us examine the dependence of the dielectric behaviour of a superconductor on temperature a bit further. Fig. 3.13(a) shows how the density of superconducting carriers and the permittivity of the superconductor change as a function of temperature. According to the two-fluid model, all free electrons at zero temperature are in superconducting state, so that the density of normal electrons is $n_n = 0$. This corresponds to an ideal conductor. On the contrary, at the critical temperature $T_c$ and above no superconducting electrons exist, therefore, the density of superconducting electrons (Cooper pairs actually) is $n_s = 0$. This corresponds to the normal state, in which the superconductor is a lossy conductor at the sub-THz and THz regimes up to the gap frequency of the superconductor. At temperatures between 0 and $T_c$, Cooper pairs and normal electrons co-exist and their densities are described through the Gorter-Casimir formulas (Eq. (A.25-26)). The co-existence of normal and superconducting electron fluids (plasmas) can give rise to a plasmonic behaviour, which is more pronounced in the superconducting state close to $T_c$. Let us explain this remark a bit further. Just below $T_c$ is where the most drastic change occurs: the losses have significantly reduced, while the real part of permittivity is negative and remains high. Thus, the kinetic inductance dominates over the equivalent Ohmic resistance of the structure. However, the Faraday inductance of a superconducting planar surface remains high and comparable to the kinetic inductance, which based on Yablonovitch theory [140], implies that superconductors have the ability to support surface plasmon waves, but with poor localisation. To improve the localisation of the supported plasmonic mode structuring of the surface could be useful, e.g., by forming an array of holes in order to reduce the Faraday inductance. The effect of the hole array on extraordinary transmission is going to be discussed in this section.

Here, we report on the first experimental observation of extraordinary transmission

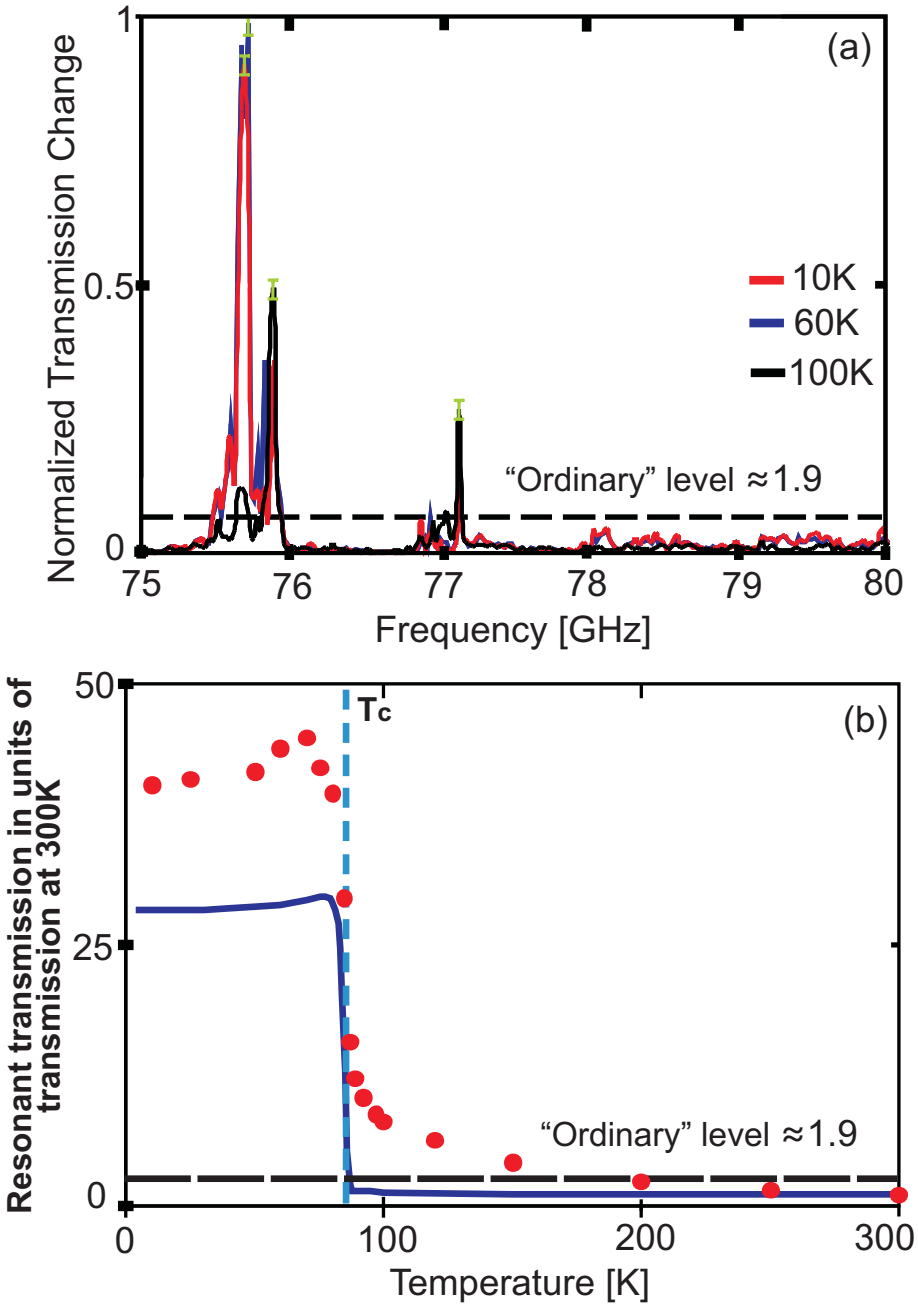


**Figure 3.14:** *Extraordinary transmission in YBCO hole array. (a) Spectra of the array's transmission change experimentally measured at three different temperatures relative to the transmission at* $300K$*. Green error-bars indicate the uncertainty due to the systematic errors induced by the experimental setup for some representative data-points. (b) Change in amplitude of the extraordinary transmission peak at* $75.7GHz$ *as a function of the sample's temperature. Red circles correspond to experimental data, while blue curve shows results of the simulation based on the two-fluid Drude model. The horizontal dashed line indicates the ordinary level of transmission calculated according to Bethe law.*

in a perforated superconducting film. The film was a 300nm-thick layer of high temperature superconductor YBCO deposited on a low-loss 1mm-thick sapphire substrate, via an intermediate $CeO_2$ buffer layer of 40nm and it was manufactured by Theva Ltd. It was perforated by etching holes with the diameter of 954$\mu$m and the period of 2.727mm, which rendered the structure non-diffracting at free space frequencies below 110GHz. The sample was 30mm in diameter and contained 81 holes. Fig. 3.13(b) and (c) show a schematic cross-section and a photograph of the sample used in the experiments, respectively. Transmission of the perforated cuprate film was measured under normal incidence at temperatures above and below its critical temperature $T_c = 88$K, in the frequency range of $75 - 110$GHz.

Fig. 3.14(a) shows sharp peaks of extraordinary transmission at frequencies between 75 and 80GHz, measured at three different temperatures; above (100K), near (60K) and well below (10K) the transition temperature. The systematic error resulting from the echo pulses due to the resonant modes in the cryostat, etc. (for more information on that refer to Section 3.4) is illustrated with the green error-bars for some representative datapoints in Fig. 3.14(a). The standard deviation of this systematic error was extracted from the peak-to-peak amplitude of the ripples in the measured data and was of the order of 0.02 for the normalised transmission. Although the magnitude of the systematic error implies that the exact transmission peak values might be slightly wrong, it does not affect the observed and reported trend of the effect. With increasing temperatures, the spectral position of the peaks shifts towards higher frequencies, while the peak amplitudes dramatically increase below $T_c$. Transmission reaches its maximum around 10K below the transition temperature and slowly decreases towards lower temperatures, as it is shown in Fig. 3.14(b).

We argue that the transmission dependence on temperature is directly reflected on the conductive properties of the material: transmission is low at high temperatures when the material can be described as a lossy metal, becomes maximum at temperatures just below the transition temperature $T_c$, and then slightly decreases, while remaining high, when the material can be considered an ideal conductor. This is because the origin of extraordinary transmission lies in the collective interaction among the holes, which depends on the conductive properties of the material. In essence, the flux of electromagnetic energy through a given hole depends on both the incident field

acting on it and the field induced by the distant holes. For the low-temperature ideal conductor state, when surface plasmons are strongly delocalised (refer to Section 4.1.2), interactions between the holes are mediated by scattered fields propagating as spherical waves $\sim \exp(jkR)/R$. Under normal incidence, this gives rise to intense narrow transmission peaks, where the wave vector $k$ is close to one of the reciprocal lattice vectors of the array. As the temperature increases, approaching $T_c$, the superconductor acts as a better plasmonic medium, which is reflected on the changes of its permittivity, which now permits higher constructive interference among the scattered fields from the holes, enhancing the interhole interactions. As a result, one also obtains narrow transmission peaks with their strength higher than in the low-temperature limit due to the smoother interhole interaction. This can qualitatively explain the rise in peak intensity for temperatures just below $T_c$, as seen in Fig. 3.14(b). Therefore, our experiment provides the direct evidence that the extraordinary transmission effect does not require surface plasmons to exist, but the enhancement of the plasmonic behaviour of the array can influence the effect.

In order to illustrate this argument, we have modeled the transmission through the superconducting sample using the two-fluid Drude model to describe the sample's dielectric properties. We have used the same method as described in the previous section, with the same parameter values. In spite of the simplicity, the model accurately predicts the main trends of spectral and temperature dependencies of transmission of the hole array in the superconducting film (see Fig. 3.14(b)). Such good corroboration between the experimental measurements and the prediction of the simple two-fluid model is particularly significant, since it indicates that the surface impedance approach may be efficiently used to describe superconducting metamaterial structures.

We verified our observations by conducting additional experimental measurements of a hole array with different perforation parameters. The holes had the diameter of 500$\mu$m and were made in a 330nm-thick YBCO film with the period of 1.5mm. A photograph of this sample is given as inset in Fig. 3.15(b). Similar to the previous case, the transmission measurements were conducted in the sub-THz frequency range of 75GHz to 110GHz with a spectral resolution of 21.8MHz. Fig. 3.15(a) shows the results for various temperatures above and below the superconducting transmission temperature. Green error-bars in Fig. 3.15(a) show the uncertainty existing in the measurements at a

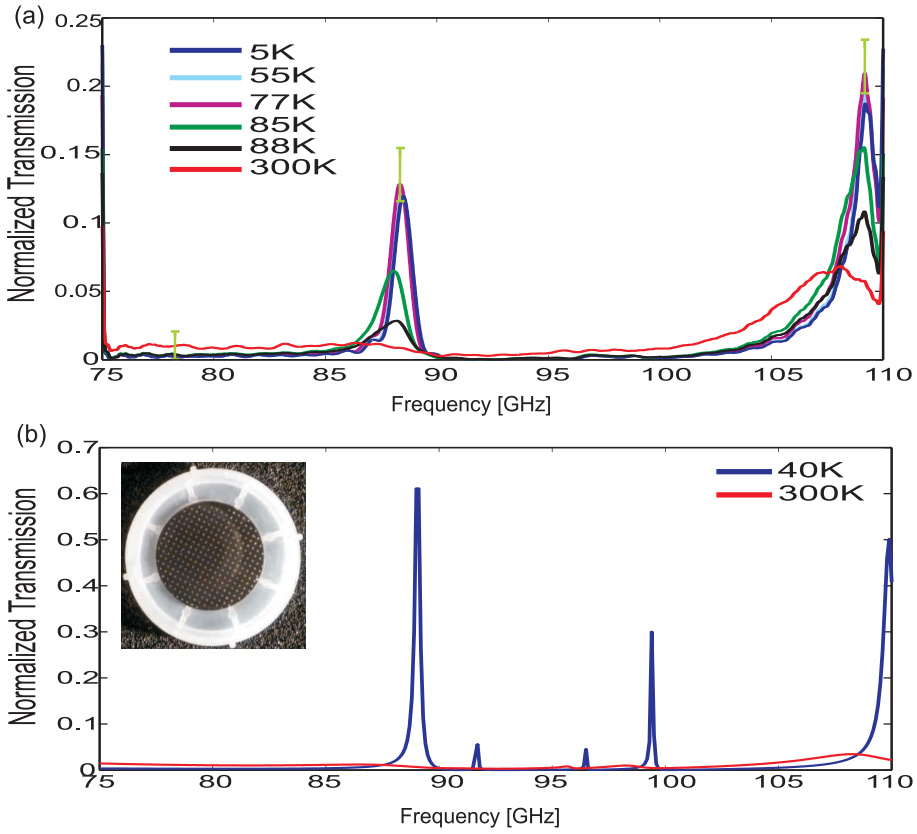


**Figure 3.15:** *Extraordinary transmission in YBCO hole array (hole diameter is 0.5mm and period of perforation is 1.5mm) (a) Transmission spectra of the array measured experimentally at various temperatures above and below $T_c$. Green error-bars indicate the uncertainty due to the systematic errors induced by the experimental setup for some representative data-points.(b) Transmission spectra of the array simulated for normal state and superconducting state. The inset shows a photo of the sample.*

few representative data-points. The standard deviation of the systematic error involved in the measurements was estimated around the value of 0.01 for the normalised transmission. The presented transmission spectrum has been low-pass filtered by applying a moving average function in order to remove the high-frequency ripples appearing due to the arrival of echo pulses (for more details refer to Section 3.4). Although this process does not reduce the uncertainty in the measured data, it helps us observe easier the main trends. As a result, however, the systematic error at the transmission peaks increases, since together with the filtering of the high-frequency ripples the steep transmission peaks are chopped off. This creates the asymmetric error-bar shapes at the two transmission peaks at 89GHz and 110GHz. The additional error resulting from the filtering process at these peaks was estimated around the value of 0.02. Fig. 3.15(a)

clearly shows a change in transmission for the resonance near 89GHz, corresponding to a 25-fold increase in the superconducting state compare to the lossy metal state. The tendency of the resonances to shift towards higher frequencies as the temperature decreases was apparent as well. The same trend, as reported earlier, is also observable here: maximum transmission enhancement did not occur at the lowest temperature, but at temperatures just below $T_c$.

We compared the experimental data with simulation results for the superconductor modelled both in the ideal conductor state (superconducting near zero temperature) and in the lossy metal state (normal state at 300K). We have to note that the response of the superconductor below the temperature of 55K remains essentially unchanged, as predicted both in the simulations and observed in the experiment (compare for example the measured data at 55K and 5K). The corroboration between the simulation and the experiment was quite good, since the simulation predicts the broad resonances around the 89GHz and the 110GHz. This, perhaps, can be attributed to the low spectral content of this hole array sample and its broad resonant features. However, the transmission peaks in the measured data are always lower in magnitude than predicted in simulations. In addition, the three very sharp resonances around 91GHz, 96GHz, and 99GHz appearing in the simulations could not be observed experimentally. This cannot be attributed to a poor spectral resolution, since the widths of these resonances are much larger (of the order of hundreds of MHz) than the spectral resolution of the measurements (21.8MHz). Furthermore, these resonances do not appear in additionally conducted measurements with higher spectral resolution (3201 points corresponding to a resolution of 10.9MHz) nor when less averaging is applied on the measured data. Most probably, the discrepancy between the measured and simulated data can be attributed to the higher losses exhibited in the fabricated sample compared to the estimated ones. Nevertheless, the experimental measurements and the simulations conducted confirm our previous claims.

Furthermore, we experimentally measured the complimentary structure of the hole array that we have just described. Thus, this structure was formed by an array of YBCO disks with the diameter of 500$\mu$m. All other dimensions were the same as in the previous experiment. A photograph of this sample is shown as inset in Fig. 3.16. The transmission spectra of that structure in the range from 75GHz to 110GHz for

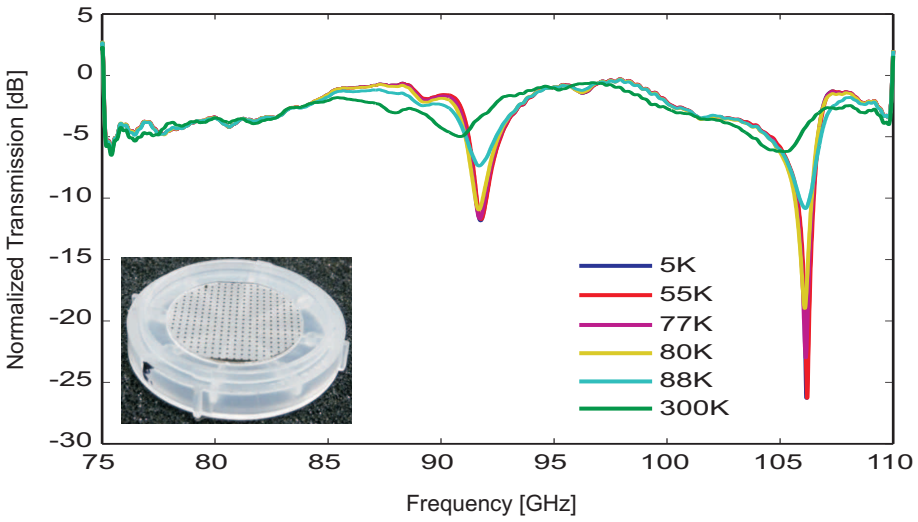


**Figure 3.16:** *Transmission spectra of an array of YBCO disks measured experimentally at various temperatures above and below $T_c$. The diameter of the disks is* 0.5*mm and the period of the array is* 1.5*mm. The inset shows a photo of the sample used in the experiment.*

temperatures above and below $T_c$ is shown in Fig. 3.16. We observe that there is a strong suppression of transmission around 91GHz and around 106GHz. This illustrates that even very simple structures can be used as efficient spectral filters of sub-THz and THz radiation, which even have the ability to adjust their response through temperature variation.

In summary, we observed an exceptionally strong manifestation of the extraordinary transmission effect in periodically perforated films of high-$T_c$ superconductors at millimetre wave frequencies. Although the effect of extraordinary transmission existed above the critical temperature of the superconductor, it achieved a maximum in the temperature range below the transition temperature, while remained strong at lower temperatures. The main features of the effect could be reproduced in the frame of the two-fluid Drude model, taking also into account the electromagnetic scattering produced by periodic perforations.

## 3.6 Towards Quantum Metamaterials

We demonstrated that metamaterials and structured surfaces fabricated from superconducting films benefit from their low Ohmic losses, and thus these structures pave the way towards the realisation of low-loss metamaterials exhibiting high Q-factor res-

onances accompanied by sharp-phase dispersion. The latter makes superconducting metamaterials one of the prime candidates for use in various sensor and switching applications. Nevertheless, the quantum nature and the associated nonlinear behaviour of superconductors have not been taken into account so far.

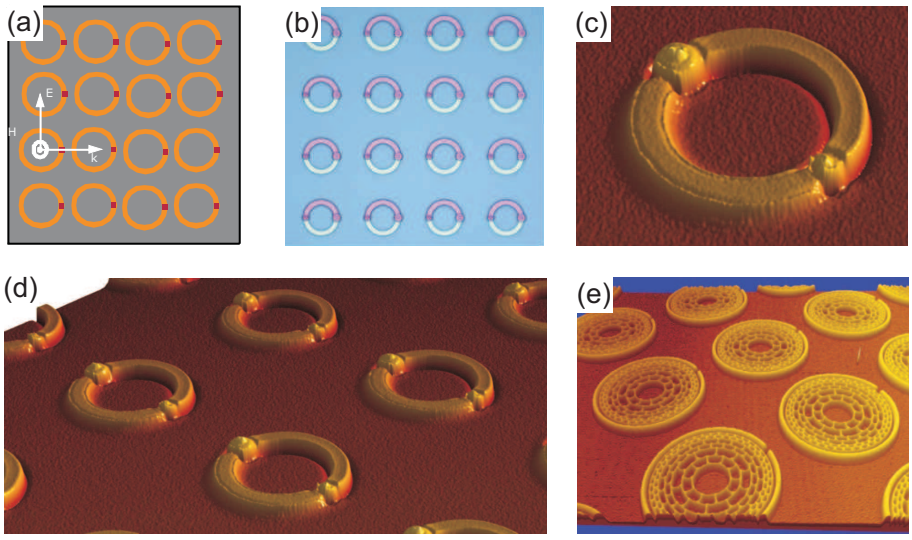


**Figure 3.17:** *(a) A schematic of a quantum metamaterial, an array of split-ring resonators, where the gaps have been replaced by Josephson Junctions (shown as red). (b) An optical microscope image of the fabricated metamaterial containing Josephson Junctions (Nb-$Al_2O_3$-Nb). (c) 3D surface map produced by the Zescope Profiler of a potential "quantum meta-atom" of the Josephson Junction metamaterial array (the Josephson Junction corresponds to the large joints seen on the image). Each unit cell of the Josephson Junction metamaterial has the size of* $60\mu m \times 60\mu m$ *while each ring has a linewidth of* $3\mu m$ *and an outer-diameter of* $33\mu m$*. (d) A larger 3D map of the same array and (e) a 3D map of the woodcut metamaterial array. Each unit cell of the woodcut metamaterial has the size of* $240\mu m \times 240\mu m$ *while each ring has a linewidth of* $8\mu m$ *and an outer-diameter of* $200\mu m$*.*

Several groups [116, 141] have theoretically proposed using the quantum properties of superconducting state to engineer and enhance the nonlinear response of sub-THz and THz metamaterials. All these suggestions resolve around the use of the so-called Josephson Junction (JJ). A JJ is formed between two superconductors coupled by a weak link. Such a weak link can consist of a thin insulating barrier, a short section of non-superconducting metal, or a physical constriction that weakens the superconductivity at the point of contact [142]. Interestingly, the relation between the supercurrent and the voltage across a JJ is highly nonlinear, thus, JJs can be used to enhance the intrinsic nonlinear nature of superconductors. The most representative example is that of an RF superconducting quantum interference device (SQUID), which consists

of a superconducting ring interrupted by a JJ, which naturally leads to the concept of Josephson Junction quantum metamaterials [116]. To realise such a metamaterial, we actually translate the classical system of a split ring resonator (SRR) into a truly quantum resonant system by replacing the gap of the SRRs with a JJ. The JJ-based SRRs trap magnetic flux within each ring, leading the magnetic flux threading through the ring ($\Phi$) to be governed by the nonlinear differential equation:

$$\frac{\partial^2\Phi}{\partial t^2} + \gamma\frac{\partial\Phi}{\partial t} + \beta\sin(2\pi\Phi) + \Phi = \Phi_{\text{ext}}, \tag{3.3}$$

where $\gamma$ represents the dissipation within the system, $\beta$ is related to the inductance and the critical current of the structure, and $\Phi_{\text{ext}}$ is the externally applied magnetic flux. It is easy to notice that the presence of the $\sin(2\pi\Phi)$ term in the equation above introduces the nonlinear behaviour in the response of the structure. Since each ring with a JJ has a current mode established that is highly sensitive to the externally applied magnetic flux, the resonant response (amplitude and spectral position of the resonance) of the metamaterial can be easily controlled by changing this externally applied magnetic field.

As we have seen, a metamaterial structure consists of an array of many meta-atoms. However, practical realization of large arrays of JJ-based superconducting metamaterials was and still is extremely challenging. We designed such a metamaterial structure that was later manufactured for us. Fig. 3.17 shows (a) a schematic of JJ-based metamaterial, (b) a microscope image of the fabricated JJ-based metamaterial, (c) a 3D surface map of a "quantum meta-atom", and (d) a 3D surface map of an array of JJ-based metamaterials. However, the experimental demonstration of quantum behavior using the JJ-based metamaterials had not been conclusive so far, probably, due to the fact that metamaterial arrays of JJs require extremely high levels of nanofabrication.

While our results with the JJ arrays were inconclusive, a new different approach to engineer quantum superconducting metamaterials was proposed by Savinov[5] [120]. This metamaterial does not contain Josephson Junctions and is simple to fabricate and scale into large arrays. The underlying idea is related to the coherent nature of the

[5]The author needs to point out that the work on flux exclusion metamaterials was mainly carried out by Savinov, while he was involved only in discussions and in their characterisation. This work is mainly presented here in order for the reader to have a complete view of the work on quantum metamaterials that has been conducted by our group.

macroscopic quantum state of carriers in a superconductor. This state dictates that the magnetic flux through a closed superconducting loop will be an integer multiple of the flux quantum $\Phi_0 = h/2e$, where $h$ is the Planck's constant and $e$ is the charge of the electron [142]. Therefore, these so-called flux-exclusion metamaterials exploit the magnetic flux quantization to achieve switching. Fig. 3.17(e) shows a 3D surface map of a woodcut array which acts as a flux-exclusion metamaterial. Flux-exclusion metamaterials manufactured from YBCO provided the first indication of the flux exclusion effect influencing the far-field electromagnetic response of a metamaterial array at millimetre-waves [120].

## 3.7 Epilogue

In this chapter, we have presented metamaterials made of high- and low-temperature superconductors YBCO and Nb. We have shown that metamaterial arrays of asymmetric split-ring resonators fabricated from both types of these superconductors are able to support strong Fano-type resonances, which are of particular practical interest due to their sharp-phase dispersion. The response of these metamaterials can be controlled by changing their temperature with the structure's Fano resonance appearing below the transition temperature of the superconductor, where Ohmic losses are considerably reduced compared to its normal state. Our results suggest the potential use of these structures in sensor, nonlinear, and switching applications in the sub-THz and THz regimes up the the gap-frequency of the relevant superconductor.

Furthermore, in the case of hole arrays, the experimental data show resonances of extraordinarily transmission, which dramatically increase when $T_c$ is reached. As the temperature is reduced below $T_c$, the transmission amplitude reduces slightly, while the resonances shift towards higher frequencies. The origin of this effect is in the collective interaction between the holes, which is affected by the tunable dielectric properties of the superconductor (i.e., among normal, ideal conductor, and plasmonic states).

# 4

# Guiding THz Radiation

THz waves due to their higher frequencies compared to radio and microwaves are able to offer very attractive information transmission rates (i.e., information capacity) and can also be used for high resolution THz imaging. These attractive qualities mark their potential use in the propagation of data signals in information-processing circuits and in guiding of imaging signals from sensors to processing units. However, THz waveguiding is generally limited by the dielectric and/or Ohmic losses and the high dispersion introduced by the waveguiding structures considered at these frequencies.

More importantly, data-transfer between compact processing units as well as in imaging devices is greatly favored by the localisation of the wave in deep-subwavelength volumes. This strong localisation of the THz modes beyond the diffraction limit can be achieved by adopting solutions from the field of plasmonics. But the cost for achieving high localisation levels is a significant increase in the attenuation and dispersion of the supported plasmonic modes compared to conventional waveguiding techniques, as a result of the enhanced interaction of these modes with the surrounding media [37].

In this chapter we exploit the possibility of using superconductors for the propagation of surface plasmon-polariton modes in the THz and sub-THz regions. We show that superconductors, due to their dominant kinetic inductance, are intriguing yet natural plasmonic media capable of supporting low-loss plasmonic modes with extreme confinement and dispersionless propagation.

The chapter starts by introducing the field of plasmonics, offering a unified theory covering both the true and the spoof plasmons. Then, the origin of the plasmonic response in the superconductors is explained, followed by the description of efficient

waveguiding structures supporting propagating superconducting plasmonic modes in the THz domain. The chapter concludes with the potential to use and actively control these structures in real-life devices in the near future.

## 4.1 The Field of Plasmonics

We briefly introduced the field of plasmonics in Chapter 1, where it was mentioned that surface plasmon polaritons (SPPs) are electromagnetic (EM) waves coupled to collective oscillations of the conduction electrons at interfaces between metals and dielectrics. More generally, it can be proven that SPPs can be excited at an interface between two media with dielectric functions of opposite signs. Such an interface is usually formed between a metal and a dielectric or air, but also interfaces between dielectrics and semiconducting or superconducting (as we will show) materials can support SPPs.

In a strict sense, polaritons are quasiparticles resulting from the coupling of electromagnetic waves with a quantised electric or magnetic dipole-carrying excitation. In the case we examine here, the polaritons are formed by the coupling of EM waves with plasmons, which are quasiparticles resulting from the quantization of plasma oscillations. In this process, surface plasmon-polaritons (SPPs) are formed when light-induced packets of electrical charges (such as electrons in metals) begin to collectively oscillate at the surface of metals in the frequency region below the bulk plasma frequency and remain coupled to the propagating EM wave which excited them. SPP modes have their amplitude reaching maximum at the interface between the conducting and the dielectric medium and exponentially decay away from the interface into the dielectric or the metallic regions (SPPs are evanescent waves).

The existence of propagating SPP modes has been known for decades [39]. However, the 'second birth' of SPPs and the recent rapid development of research in this area occurred when scientists realized that SPP modes in metallic nanostructures may lead to the localization of guided light signals far beyond the diffraction limit [40, 143]. The explosive growth of interest here has been driven by parallel advances in nanofabrication technologies as well as by high expectations of a wide range of potential applications in areas ranging from bio-chemical sensing to solar power generation.

The most common description of SPPs is based on the electromagnetic theory and

will be given below first. Then, we present a complimentary description based on a circuit-element analysis [140]. While the former is more intuitive in terms of description, the latter can highlight many of the unique plasmonic properties and provide criteria for the design of efficient plasmonic structures. Such a dual description combined with the physical mechanism that underlies the appearance of plasmon-polaritons constitutes a wide presentation of the physics involved in the propagation of SPP modes.

### 4.1.1 The Electromagnetic Description of SPP Modes

**SPPs at a single interface**

The most simple geometry that supports guiding of SPP waves is the interface between semi-infinite regions of a metal and a dielectric (similar to Fig. 4.1(a)). We start with the assumption that neither of the two regions introduces any losses and consider the Helmholtz wave-equation:

$$\nabla^2\mathbf{E} + k_0^2\varepsilon_r\mathbf{E} = 0, \tag{4.1}$$

where $k_0 = \omega/c$ is the wavenumber in vacuum, and $\varepsilon_r$ is the relative permittivity of the medium. In this particular geometry, permittivity is a function of only $y$ co-ordinate, therefore $\varepsilon = \varepsilon(y)$. The region corresponding to $y > 0$ has relative permittivity $\varepsilon_2$, while the region $y < 0$ has $\varepsilon_1$. At this point, we place no restriction for the values of $\varepsilon_1$ and $\varepsilon_2$. The interface between the two media corresponds to the plane $y = 0$, and if an evanescent wave propagates along this interface towards positive $z$ direction, it should have the following form:

$$\mathbf{E}(x, y, z) = \mathbf{E}(y)e^{-jk_{\mathrm{spp}}z}, \tag{4.2}$$

where $k_{\mathrm{spp}}$ is the propagation constant of the supported modes, corresponding in reality to the parallel component of the wave vector in the propagation direction. By substituting Eq. (4.2) in the Helmholtz equation we get:

$$\frac{\partial^2\mathbf{E}(y)}{\partial y^2} + (k_0^2\varepsilon_r - k_{\mathrm{spp}}^2)\mathbf{E}(y) = 0. \tag{4.3}$$

The equivalent equation for the magnetic field **H** can be derived the same way. Aiming to define the spatial profile and the dispersion equation of the supported modes, we

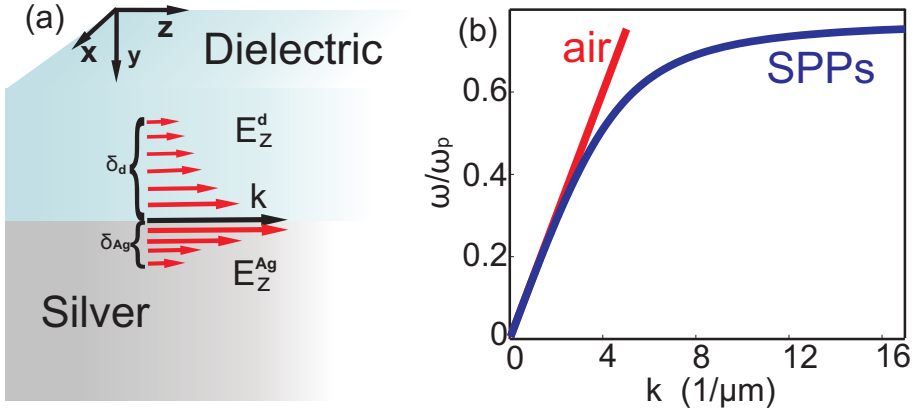


**Figure 4.1:** *(a) Distribution of the electric field $E_z$ component of the plasmonic surface state at an interface between a metal (silver here) and a dielectric. (b) The dispersion curve of an SPP mode (blue) in a silver-air single interface. Light line in air (red) is also shown.*

have to define the relations between the components of the electric and magnetic fields. These relations are derived directly from Maxwell equations. Assuming harmonic time-dependence, we have that $\partial/\partial t \equiv j\omega$ and we get:

$$\frac{\partial E_z}{\partial y} - \frac{\partial E_y}{\partial z} = -j\omega\mu_r\mu_0 H_x, \tag{4.4}$$

$$\frac{\partial E_x}{\partial z} - \frac{\partial E_z}{\partial x} = -j\omega\mu_r\mu_0 H_y, \tag{4.5}$$

$$\frac{\partial E_y}{\partial x} - \frac{\partial E_x}{\partial y} = -j\omega\mu_r\mu_0 H_z, \tag{4.6}$$

$$\frac{\partial H_z}{\partial y} - \frac{\partial H_y}{\partial z} = j\omega\varepsilon_r\varepsilon_0 E_x, \tag{4.7}$$

$$\frac{\partial H_x}{\partial z} - \frac{\partial H_z}{\partial x} = j\omega\varepsilon_r\varepsilon_0 E_y, \tag{4.8}$$

$$\frac{\partial H_y}{\partial x} - \frac{\partial H_x}{\partial y} = j\omega\varepsilon_r\varepsilon_0 E_z. \tag{4.9}$$

We consider propagation of the wave towards the positive direction of $z$-axis, therefore $\partial/\partial z \equiv -jk_{\text{spp}}$, while no variation is considered in $x$-direction ($\partial/\partial x \equiv 0$). Thus, Eq. (4.4-9) give[1]:

[1]In this analysis only non-magnetic materials are considered. Therefore, the relative magnetic permeability is taken equal to 1.

$$\frac{\partial E_z}{\partial y} + jk_{\text{spp}}E_y = -j\omega\mu_0 H_x, \tag{4.10}$$

$$k_{\text{spp}}E_x = \omega\mu_0 H_y, \tag{4.11}$$

$$-\frac{\partial E_x}{\partial y} = -j\omega\mu_0 H_z, \tag{4.12}$$

$$\frac{\partial H_z}{\partial y} + jk_{\text{spp}}H_y = j\omega\varepsilon_r\varepsilon_0 E_x, \tag{4.13}$$

$$k_{\text{spp}}H_x = -\omega\varepsilon_r\varepsilon_0 E_y, \tag{4.14}$$

$$-\frac{\partial H_x}{\partial y} = j\omega\varepsilon_r\varepsilon_0 E_z. \tag{4.15}$$

From the above equations it is easily seen that two groups of independent solutions are supported. Each solution corresponds to a different polarization. The first solution describes the transverse magnetic modes (TM or p modes), for which only $E_y$, $E_z$ and $H_x$ components of the field are non-zero, while the second solution defines the transverse electric modes (TE or s modes), with only $H_y$, $H_z$ and $E_x$ being non-zero components.

For the TM modes we get:

$$E_y = -\frac{k_{\text{spp}}}{\omega\varepsilon_r\varepsilon_0}H_x, \tag{4.16}$$

$$E_z = -\frac{1}{j\omega\varepsilon_r\varepsilon_0}\frac{\partial H_x}{\partial y} \tag{4.17}$$

and the wave equation can be written in the form:

$$\frac{\partial^2 H_x}{\partial y^2} + (k_0^2\varepsilon_r - k_{\text{spp}}^2)H_x = 0. \tag{4.18}$$

We look for solutions that represent propagating modes localized at the interface between the two media. Thus, their amplitude should decay exponentially as $y$ moves away from zero. For the $y > 0$ region we get:

$$H_x(y) = A_2 e^{-k_2 y} e^{-jk_{\rm spp} z}, \tag{4.19}$$

$$E_y(y) = -\frac{k_{\rm spp} A_2}{\omega \varepsilon_2 \varepsilon_0} e^{-k_2 y} e^{-jk_{\rm spp} z}, \tag{4.20}$$

$$E_z(y) = \frac{k_2 A_2}{j\omega \varepsilon_2 \varepsilon_0} e^{-k_2 y} e^{-jk_{\rm spp} z}. \tag{4.21}$$

And for the $y < 0$ region we get:

$$H_x(y) = A_1 e^{k_1 y} e^{-jk_{\rm spp} z}, \tag{4.22}$$

$$E_y(y) = -\frac{k_{\rm spp} A_1}{\omega \varepsilon_1 \varepsilon_0} e^{k_1 y} e^{-jk_{\rm spp} z}, \tag{4.23}$$

$$E_z(y) = -\frac{k_1 A_1}{j\omega \varepsilon_1 \varepsilon_0} e^{k_1 y} e^{-jk_{\rm spp} z}. \tag{4.24}$$

The quantities $k_i = k_{y,i} > 0$ with $i = 1, 2$, are the components of the wave vector normal to the interface between the two media. The inverse quantity $\delta_i = 1/k_{y,i}$, expresses the penetration depth of the wave inside each of the two media. This quantity reveals how localized the supported mode is near the interface. Taking into account the continuity of the tangential component of the magnetic field ($H_x$) and of the electric field ($E_z$) on the interface $y = 0$, we conclude that:

$$A_1 = A_2 \tag{4.25}$$

$$\frac{k_2}{k_1} = -\frac{\varepsilon_2}{\varepsilon_1} \tag{4.26}$$

At this point, in order for a surface wave to exist and be bounded to the surface, the necessary condition $\varepsilon_1 \varepsilon_2 < 0$ must be fulfilled. So, an SPP mode will exist only if the two media have opposite signs of their electric permittivities. Media with negative dielectric function are metals, in some cases semiconductors, or even superconductors below their plasma frequency, while dielectrics most commonly possess positive values of permittivity. For a combination of materials that fulfil this condition we get:

$$k_1^2 = k_{\rm spp}^2 - k_0^2 \varepsilon_1, \tag{4.27}$$

$$k_2^2 = k_{\rm spp}^2 - k_0^2 \varepsilon_2. \tag{4.28}$$

From which the dispersion equation of an SPP mode in the case of an infinite planar interface can be derived:

$$k_{\text{spp}} = k_0 \sqrt{\frac{\varepsilon_1 \varepsilon_2}{\varepsilon_1 + \varepsilon_2}}. \tag{4.29}$$

For any specific frequency the wavenumber of the SPP mode is higher than the one of a plane wave propagating in the dielectric region. Thus, such a mode cannot be excited directly by the plane wave due to its insufficient momentum (wavenumber), and a special mode matching technique is required [37]. Fig. 4.1(b) shows the dispersion curve of an SPP mode in a sliver-air single interface.

We also examine the case of TE modes. From Eq. (4.11-12), we get:

$$H_y = \frac{k_{\text{spp}}}{\omega \mu_0} E_x, \tag{4.30}$$

$$H_z = \frac{1}{j\omega\mu_0} \frac{\partial E_x}{\partial y}. \tag{4.31}$$

So the wave equation (Eq. (4.3)) in this case can be written in the form:

$$\frac{\partial^2 E_x}{\partial y^2} + (k_0^2 \varepsilon_r - k_{\text{spp}}^2) E_x = 0. \tag{4.32}$$

We are searching for solutions expressing TE surface waves. For the region $y > 0$ the non-zero components of the field are:

$$E_x(y) = A_2 e^{-k_2 y} e^{-jk_{\text{spp}} z}, \tag{4.33}$$

$$H_y(y) = \frac{k_{\text{spp}} A_2}{\omega \mu_0} e^{-k_2 y} e^{-jk_{\text{spp}} z}, \tag{4.34}$$

$$H_z(y) = -\frac{k_2 A_2}{j\omega\mu_0} e^{-k_2 y} e^{-jk_{\text{spp}} z}. \tag{4.35}$$

While for the region $y < 0$ we get:

$$E_x(y) = A_1 e^{k_1 y} e^{-jk_{\text{spp}} z}, \tag{4.36}$$

$$H_y(y) = \frac{k_{\text{spp}} A_1}{\omega \mu_0} e^{k_1 y} e^{-jk_{\text{spp}} z}, \tag{4.37}$$

$$H_z(y) = \frac{k_1 A_1}{j\omega\mu_0} e^{k_1 y} e^{-jk_{\text{spp}} z}. \tag{4.38}$$

The continuity boundary conditions for the components $E_x$ and $H_z$ on the interface

$y = 0$ lead to:

$$A_1(k_1 + k_2) = 0. \tag{4.39}$$

Since both $k_1 > 0$ and $k_2 > 0$ due to the fact that we are looking for a surface wave solution, Eq. (4.39) leads to $A_1 = 0$, and therefore $A_1 = A_2 = 0$, which implies that no SPP mode with TE polarization exists.

In case of a negative-$\varepsilon$ medium with losses in the $y < 0$ region, $\varepsilon_1$ is a complex number with the imaginary part being negative. This results in $k_1$ and $k_2$ being complex numbers as well, with their real parts being positive (so that the wave attenuates as we move away from the interface in the $y$-direction). Following the same analysis it is easy to show that a surface wave is supported if $\Re[\varepsilon_1] < 0$ and $\varepsilon_2 > 0$. However, losses limit the propagation length of the mode, which depends on the extent (concentration level) of the mode inside the lossy region. The propagation length of the mode, defined as the distance at which the energy of the wave is attenuated to the $1/e$ level compared to its initial value, is :

$$L = \frac{1}{2|\Im[k_{\text{spp}}]|} \tag{4.40}$$

The cases when losses are also/only in the dielectric region are treated in the same way. It is important to mention that the greater the extent of the mode inside the lossy medium, the smaller its propagation length. This tradeoff, although depends on the particular waveguiding structure considered, always applies to any SPP geometry.

Note: It is useful to describe the propagation of the SPP mode in terms of an effective refractive index and an attenuation constant. Given that the propagation constant of an SPP mode is $k_{\text{spp}}$ and that of a free-space propagating wave corresponding to the same frequency is $k_0$, we define as the effective refractive index $n_{\text{eff}}$ of the SPP mode the quantity given by the relation $n_{\text{eff}} = \Re[k_{\text{spp}}/k_0]$, and as the attenuation constant of the SPP mode the quantity $\alpha$ defined through the relation $\alpha = \Im[k_{\text{spp}}/k_0]$.

**SPPs in three-layer structures**

As a next step it is instructive to examine multilayered structures where the sign of the real part of the dielectric permittivity alternates from layer to layer. In such structures, each interface is able to support a propagating SPP mode. When the penetration depth $\delta$ (as defined above) is comparable to or smaller than the thickness

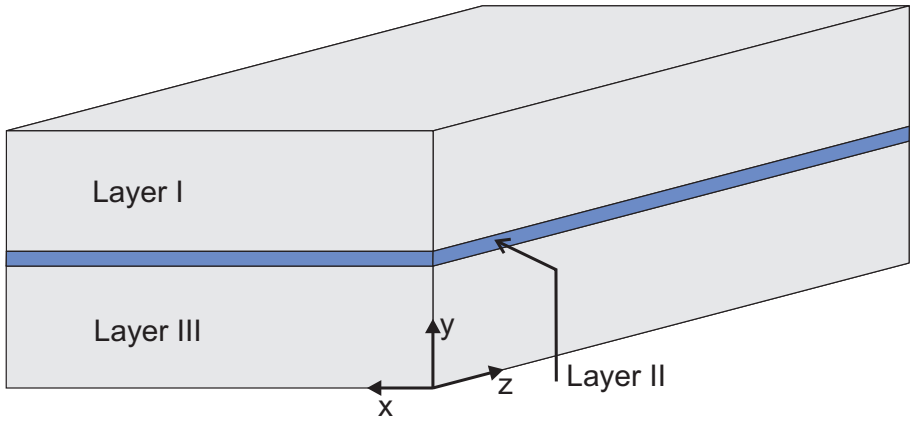


**Figure 4.2:** *Geometry of a three layer structure. Infinite extension in x-direction is assumed. In most practical cases, layer II is thin in order for coupled SPP modes to exist.*

of these layers, a strong interaction between the modes supported by each interface takes place, leading to the excitation of coupled modes. The simplest case of a multilayer structure is the symmetric three-layer structure (see Fig. 4.2), where layers I and III are the same ($\varepsilon_1 = \varepsilon_3$), which leads to $k_1 = k_3$. The most common examples of three-layer structures are Insulator-Metal-Insulator (IMI), which are actually thin films embedded in dielectrics, and Metal-Insulator-Metal (MIM) structures, which are also known as parallel plate or gap-plasmon waveguides. Following a similar analysis to the one presented above for a single interface and examining the lowest order modes only, we conclude that two plasmonic modes are supported, one of which is symmetric (even) and the other is antisymmetric (odd) [37]. They appear as a result of coupling of two independent modes formed at the two interfaces. We can easily derive the dispersion equations for these coupled plasmonic modes:

$$\tanh(k_2 a) = -\frac{k_1 \varepsilon_2}{k_2 \varepsilon_1}, \tag{4.41}$$

$$\tanh(k_2 a) = -\frac{k_2 \varepsilon_1}{k_1 \varepsilon_2}. \tag{4.42}$$

Starting with IMI geometry, we assume that the metallic layer between the two dielectric layers has a thickness of $2a$. In this case, $\varepsilon_2 = \varepsilon_2(\omega)$ is the frequency-dependent permittivity of the metal, while $\varepsilon_1$ is the positive relative permittivity of the substrate and superstrate. For the odd modes in IMI structures, the mode concentration in-

side the metal layer is decreasing when the thickness of the layer is decreasing and as the thickness of the metal is approaching zero the mode transforms into a plane wave propagating in the dielectric along the metal layer. As a result of the reduced Ohmic losses due to the weaker confinement in the metallic region the propagation length dramatically increases. That was why the odd modes were termed Long-Range SPPs (LR-SPPs) [144]. The even modes show the opposite behaviour, with their propagation length decreasing as the thickness of the metal decreases, and were termed Short-Range SPPs (SR-SPPs) [37].

In case of MIM geometries, we have $\varepsilon_1 = \varepsilon_1(\omega)$ for the frequency-dependent permittivity of the metallic regions, and $\varepsilon_2$ for the relative permittivity of the dielectric spacer. The most important feature of the supported modes in MIM structures is that no cut-off thickness exists for the odd mode. In addition, the propagation constant (or the effective refractive index) of the odd mode can take substantially larger values than the refractive index of the dielectric in the central region (layer II) as its thickness decreases. This leads to enhanced localization inside the dielectric layer with only small penetration in the metallic layers. However, in practice, due to finite conductivity, e.g., of metals, there is a tradeoff between the propagation length of the mode and the level of localisation achieved.

### 4.1.2 The Circuit-Model Analysis of SPP Modes

The electromagnetic analysis presented above yields the necessary conditions for observing SPP modes at the interface between two media. We concluded that the supported modes can only be TM polarized and the media must have dielectric functions with opposite signs in the desired frequency range. However, the question whether these modes are able to provide localization beyond the diffraction limit and multifold compression of the field in the propagation direction remains open. For example, from the electromagnetic analysis we conclude that in case of a metal-dielectric interface there is always a supported propagating plasmonic mode as long as the frequency is below the metal's plasma frequency (in this region metals have negative permittivities), but for frequencies in the microwave range the supported plasmonic mode is indistinguishable from a plane wave propagating along the interface in the dielectric region (i.e., no localisation or compression of the field in the propagation direction is achieved). It

would be very useful to have the a-priori knowledge of whether the supported mode for a particular waveguiding geometry is offering the ground for "useful plasmonics". We have to clarify that with the term "useful plasmonics" we imply plasmonic waveguiding that provides localization beyond the diffraction limit and effective refractive indexes much higher than that in the dielectric regions.

The theory of Yablonovitch et al. tries to answer this question with a simple and elegant model derived from an electrical networks approach [140]. Although electric circuit analogues have been already considered for describing localised plasmonic resonances in metallic nanoparticles [37], as shown in Fig. 4.3, Yablonovitch et al. suggested such an approach also for propagating SPP modes. Let us discuss this approach a bit further. Assume a bulk medium with a cross-section area $A$ subjected to a small electric field $\mathbf{E}$. This field creates a small charge separation $z$ inside the medium. When we remove the external field, the displaced electron cloud starts to oscillate around the ionic lattice. The natural frequency of these oscillations is called the plasma frequency $\omega_p$. Based on the suggested view, the electronic sub-system could be seen as a mass on a spring oscillator or an electric circuit LC oscillator. Having the LC oscillator as an analogue, the plasmon oscillation will have a resonant frequency:

$$\omega_{LC}^2 = \frac{1}{LC} = \frac{nq^2}{\varepsilon m}\frac{z}{A}\frac{A}{z} = \frac{nq^2}{\varepsilon m} \equiv \omega_p^2, \tag{4.43}$$

where $n$ is the number of charge $q$ carriers, each one having mass $m$, and $\varepsilon$ is the permittivity. Thus plasmonic oscillations can be represented by an equivalent kinetic inductance $L_{\text{kin}} = \frac{m}{nq^2}\frac{z}{A}$ and a capacitance $C = \varepsilon\frac{A}{z}$ created by the charge lattice separation.

We now consider a conducting medium, such as a metal, described by the Drude model [145]. Its dielectric function is given by the following formula:

$$\varepsilon = \varepsilon^{'} + j\varepsilon^{''} = 1 - \frac{\omega_p^2\tau^2}{\omega^2\tau^2+1} - j\frac{\omega_p^2\tau}{\omega(\omega^2\tau^2+1)}, \tag{4.44}$$

where $\omega_p$ is the plasma frequency of the electrons and $\tau$ their relaxation time. The full derivation of Eq. (4.44) was given in Section A.2.2, where it was shown that conductivity is related to permittivity through the formula: $\sigma = j\omega\varepsilon_0(\varepsilon - 1)$. Based on this

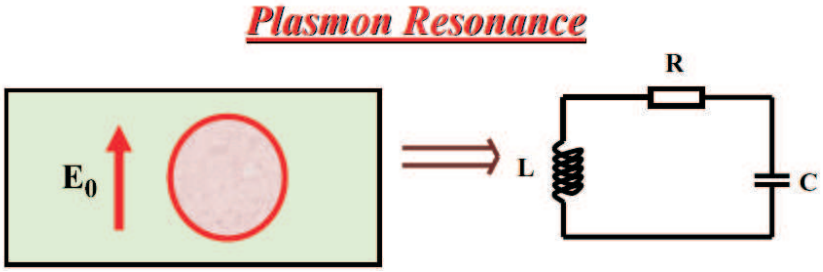


**Figure 4.3:** *An artistic illustration of a metallic nanoparticle excited by an oscillating electric field $E_0$. Such a system forms a plasmonic resonator that can be mapped onto an equivalent electric LC resonator [37]. In the case of existing losses in the plasmonic system, the LC resonator also includes a resistance R (i.e., formally, an RLC resonator).*

relationship, we calculate the complex resistivity of the material:

$$Z = \frac{1}{\sigma(\omega)} \frac{z}{A}, \tag{4.45}$$

which can be written also in the form $Z = R + j\omega L_{\text{kin}}$, meaning that the material is described as the combination of a resistance $R$ and an inductance $L_{\text{kin}}$, with

$$R = \frac{m}{nq^2\tau} \frac{z}{A}, \tag{4.46}$$

and

$$L_{\text{kin}} = \frac{1}{\omega^2 \varepsilon_0 (1-\varepsilon)} \frac{z}{A}. \tag{4.47}$$

The resistive term describes the energy dissipation by the electron gas and depends on the relaxation time $\tau$ of the electrons. In addition, in every structure there is an additional term due to the Faraday inductance $L_F$ linked to the magnetic field created by the flow of currents in the structure. Therefore, the total inductance is $L = L_{\text{kin}} + L_F$.

Based on Yablonovitch's theory, we suggest that the behaviour of the plasmonic modes is controlled by two criteria. The first criterion asks for the kinetic inductance to be comparable to the Faraday inductance, which in the electromagnetic (equivalent) description corresponds to the effective refractive index of the SPP mode to be higher than the refractive index of the dielectric in the structure. This is a measure of both the localisation and the propagation velocity of the mode. By defining a certain difference

between the refractive indexes we can end up with a design rule:

$$\frac{L_{\text{kin}}}{L_F} > c_1, \tag{4.48}$$

where $c_1$ is a parameter that depends on the ratio between the effective refractive index of the SPP mode to the refractive index of the dielectric. This formula suggests two ways of enhancing the localisation of the mode. The first way is based on just increasing the $L_{\text{kin}}$ term. Materials, predominately metals, that have small negative values of permittivity in the targeted frequency range are the best candidates here, since this is translated to immediate enhancement of the kinetic inductance term. In this context gold (Au), aluminium (Al), and silver (Ag) are considered good plasmonic media in the visible part of the spectrum. The second way is to suppress the Faraday inductance more than the kinetic inductance through the structuring of the medium. Since the Faraday inductance is associated with the magnetic field created by currents flowing through the structure, geometries that favor smaller induced currents or currents that mutually cancel their induced magnetic fields lead to lower Faraday inductance values and promote stronger plasmonic response. This second category encompasses the solutions based on plasmonic waveguides and, in a broader sense, spoof-plasmon concepts, for which the next section is devoted.

Of course, the issue of losses has to be examined as well. The second criterion is related to the fact that the plasmonic response should not be completely damped by losses, and therefore, expresses our ability to measure such a response or, even more, exploit it. A propagating plasmonic mode has to 'survive' after the energy dissipation due to scattering of electrons predominately with the lattice ions and impurities. Therefore, the system should be able to have kinetic inductance larger than its intrinsic resistance, so that the input power is not immediately transformed to heat losses. So the second criterion can be expressed mathematically by the following formula:

$$\frac{\omega L_{\text{kin}}}{R} > c_2, \tag{4.49}$$

where $c_2$ is related to the propagation distance of the mode. If $c_2$ is approaching zero the electron gas oscillations are immediately damped, killing the plasmonic response.

It is only when both Eq. (4.48) and Eq. (4.49) are fulfilled that we have distinct

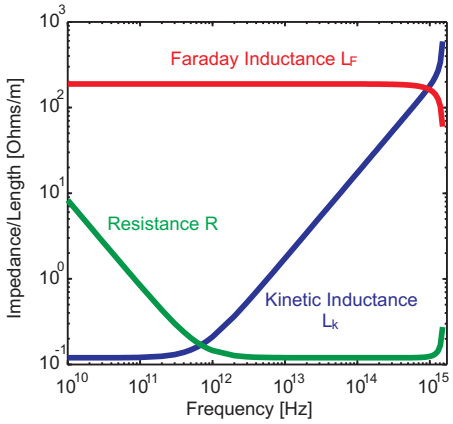


**Figure 4.4:** *Frequency dependence of Faraday inductance, resistance and kinetic inductance calculated for a silver-air planar interface. The plasmonic regime coincides with the dominance of kinetic inductance term. Derivations are based on the theory presented in [140] assuming a plasma frequency of* $\omega_p = 2\pi 2.18 \times 10^{15}$ *rad/s and a relaxation time of* $\tau = 2.297 \times 10^{13} s$ *for silver [146].*

plasmonic modes that are strongly confined beyond the diffraction limit and propagate far enough. These properties are useful in signal processing, imaging, etc. So we can claim that these criteria mark the "useful" plasmonic regime. For a metal-dielectric surface these criteria are met only for frequencies in the IR and visible parts of the spectrum. For example, in Fig. 4.4 the plasmonic regime is presented for the case of a silver-air interface in terms of the resistance, kinetic inductance, and Faraday inductance, derived following the analysis presented in [140]. This regime coincides with the region where the kinetic inductance dominates.

Based on this model, one can conclude that metals offer the potential for subwavelength guiding of SPP modes in optical frequencies with a variety of different structures including planar interfaces, IMI and MIM structures, cylindrical metal nanowires or nanoholes [147], V-groove waveguides [148], dielectric loaded SPP waveguides (DLSPPWs) [149], and even chains of nanoparticles [143]. Such structures find applications in the field of nanophotonics using tapered metallic guiding nanostructures [150], in sensors, or in the fabrication of passive plasmonic components including plasmonic couplers [151], Mach-Zehnder interferometers, and filters [152].

### 4.1.3 Creating Spoof Plasmons

Just before diving into the topic of superconducting plasmonics, we briefly discuss the concept of spoof plasmons. Structures that are able to support spoof plasmon modes offer a viable solution for guided propagation of THz waves.

Metals in the RF, microwave, and millimetre-wave regimes have very high but finite conductivity. Values as large as $10^9$S/m are very typical, leading to the common practice of considering metals in these frequencies as perfect electric conductors (PEC). A perfect electric conductor has infinite conductivity and does not allow electric fields to penetrate its interior. Such an approach is very convenient for analytical and numerical modelling, since it reduces considerably the complexity of the problem [65]. The perfect electric conductor leads to a Dirichlet boundary condition [65], simplifying the electromagnetic model. Unfortunately, a perfect electric conductor does not support SPP modes. This can be explained by the fact that we model such a conductor without a negative real part of permittivity, in addition to the fact that a PEC boundary condition does not allow for any tangential component of the electric field to exist. Thus, no TM mode is supported at the metal-dielectric interface.

In 2004, Sir John Pendry et al. of Imperial College London reported on the appearance of electromagnetic modes similar in behaviour to SPPs on surfaces of perfect electric conductors perforated with holes (Fig. 4.5(a)) [41]. They managed to show that the microwave TM surface mode supported in this case was governed by an effective permittivity of the same frequency dispersion as in plasmonic metals at the optical frequencies. More interestingly, they proposed that the size and spacing of holes can control the dispersion characteristics of the modes in frequency and in space, opening a way to design the spoof plasmon response of the material. A whole new perspective appeared in how to create localised electromagnetic modes near the surface of metals; followed by many published papers on this field afterwards. A complete treatment of the topic can be found in [138].

It should be noted that corrugated surfaces were first shown to support strongly bounded propagating TM modes back in the 1960s (Fig. 4.5(b)). For instance, in the book of R. E. Collin "Field Theory of Guided Waves" surface waves propagating along a corrugated plane are described in detail as a way to achieve guiding of localised

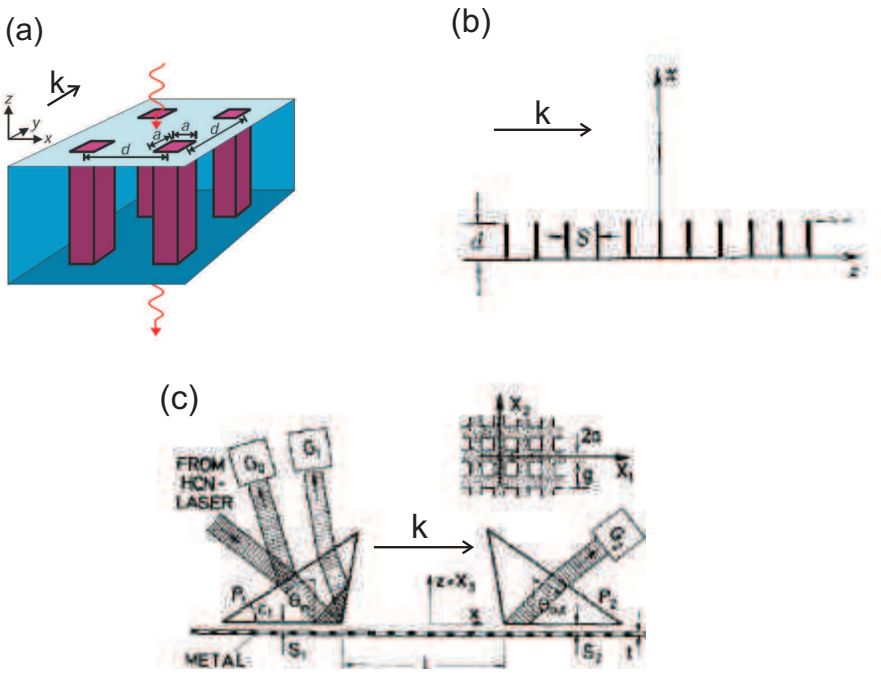


**Figure 4.5:** *(a) The structure considered in recent spoof plasmons concept from [41]. An 1D surface corrugation for localising a TM surface wave from [42]. The structure considered by Ulrich and Tacke for bounding millimetre waves from [43].*

electromagnetic modes [42]. Usually such modes were termed TM modes of the "slow wave type" due to their high effective refractive index but had not been related to plasmons. Furthermore, the effect of the corrugation parameters, such as the period in the case of 1D and 2D periodic structures, the thickness, etc. was known to control the dispersion characteristics. More interestingly, such approaches had been not only known theoretically but they also found use in end-fire antenna designs back in that days.

This kind of approach in waveguiding is very important in the case of millimetre and THz waves, where materials could still be seen as perfect conductors. This was already understood and explored more than 30 years ago (Fig. 4.5(c)). Most important is the work of R. Ulrich and M. Tacke in 1972 [43]. The authors reported on guiding TM surface waves along thin copper sheets perforated in a regular pattern (metallic mesh). In addition, the ability to control the dispersion characteristics of the propagating mode was demonstrated.

In reality, metals do have a finite conductivity leading to a large but finite complex permittivity with negative real and imaginary parts. This actually implies that metals

even at low frequencies have the ability to support SPP modes, as has been explained in the previous subsection. However, the large values of the real and imaginary parts of the permittivity make the guided modes to spread over many wavelengths in the dielectric region, while they penetrate only marginally the conducting medium. These modes have propagation constants essentially equal to the wavenumber of a plane wave propagating in the dielectric along the conducting surface at these frequencies. Therefore the result obtained with the PEC assumption is indeed a very good approximation to reality. An analysis of spoof plasmon modes based on the exact conductivity of metals is presented in [153], which can be considered for the THz region as well. In this region, corrugated surfaces offer an efficient way to create plasmonic modes [44]. As we have seen, this structuring is equivalent to reducing the Faraday inductance of the structure, so that the kinetic inductance can dominate. Nevertheless, the response of the structure shows a high frequency dispersion, while the structure itself lacks the ability to adapt.

## 4.2 Superconducting Plasmonics

As mentioned before, for the plasmonic technology to be efficient and useful the issue of losses has to be resolved. This is a taunting problem, since losses increase as the localization of the mode is increased. One way of compensating for the power losses of an SPP mode is to introduce optical gain in the dielectric material adjacent to the metal. But since the gain required to match the SPP dissipative loss is very large, all attempts so far have only slightly increased the propagation length of the mode [154]. An example of this was recently shown with gain compensation for losses using optically pumped dye molecules [155]. Other approaches towards this challenge are focusing in developing new and better plasmonic materials [156, 157].

What remains also a challenge is the implementation of active devices like modulators, plasmon amplifiers, sources, and detectors without converting SPP modes back to pure light waves or electric signals. Recently, all-optical control that has the potential for femtosecond switching by influencing the absorption in the metal [158] or the dielectric using quantum dots [159] have been achieved. However, the modulation was achieved using planar SPP modes that are not confined in the lateral direction, so the challenge of modulating guided localized SPP modes remains yet to be tackled. In

addition, recent steps in direct electrical detection of SPP modes have been made [160].

Superconductors emerge as an intriguing low-loss alternative to the metallic plasmonic media and their behaviour can be controlled dynamically through temperature variation, applied magnetic fields, or current signals. Thus, superconductors may be used to realise plasmonic devices operating at THz frequencies that are able to confront both challenges mentioned above. In this section, we do show that superconductors due to their vanishing Ohmic resistance and dominant kinetic inductance have the ability to support propagating plasmonic excitations from low frequencies up to the THz regime [161].

Already, low-dimensional plasma modes (analogous to bulk plasma excitations in metals) or their resulting effects have been predicted in thin superconducting wires [162] and layered superconductors [163–165], and experimentally demonstrated in thin superconducting films [166]. We argue here that recent developments in the field of superconducting metamaterials [110, 112, 118, 121, 167] bring about a practical proposition for propagating superconducting plasmons. We show that the latter are genuine bound surface modes similar to optical plasmons, which up to the THz frequencies can be guided with a nanometer-scale confinement propagating for tens of millimetres without noticeable attenuation. From a theoretical point of view, this reveals that high-frequencies are not a necessary condition for the existence of useful plasmonics, while the significant potential for applications of superconducting plasmonic structures originates from the easy incorporation of active control in these devices [113].

Indeed, there are striking similarities between the electromagnetic response of metals at optical frequencies and superconductors at terahertz frequencies and below. In metals exposed to radio- and lower-frequency electromagnetic waves, the dynamics of a free electron is dominated by its ubiquitous collisions with atoms, lattice defects, and other free electrons taking place during each cycle of the driving field, as described in Section A.2.2, by the introduction of the Drude model. As a result, the electron mean velocity and thus the strength of electrical currents induced by an external wave are proportional to the instantaneous value of the field with the constant of proportionality -the conductivity- determined by the rate of such collisions. This is the regime described by Ohm's law, in which the metal is characterised by a large value of the imaginary part of the metal permittivity and a smaller real part (as shown in Fig. 4.6(a)). In

contrast, at higher optical frequencies, electrons oscillate so rapidly that no collisions happen during at least one optical cycle: the collective dynamics of electron plasma is dominated by the inertia of the carriers. Here we talk about the plasmonic regime: the displacement currents become important and the real part of the metal permittivity begins to dominate. In silver such a transition from Ohm's law electrodynamics to plasmonics occurs at frequencies above a few THz and extends into the infrared (IR) and the visible (VR) (as shown in Fig. 4.6(a)). While the response of plasmonic metals is characterised by a dominant negative real part of the permittivity at optical frequencies, in the superconducting state such a behaviour is found across most of the sub-THz and THz spectral domains (as shown in Fig. 4.6(b)). Indeed, the collective motion of 'superconducting electrons' joined in Cooper pairs experiences no scattering and proceeds freely through the lattice. In fact, each of the electrons creating the Cooper pair scatters all the time, however the total momentum of such a system (by definition of the Cooper pair given in BCS theory [168]) remains constant, so that their free acceleration in the direction of the applied electric field is not hindered. Their electrodynamic response, as in plasmonic metals, is thus determined by inertia. Moreover, the imaginary part of the permittivity is much lower than its real part. At higher frequencies, superconductors become lossy as the energy of the incident wave quanta is sufficient to break the Cooper pairs and destroy superconductivity. For example, for the high-temperature superconductor YBCO, the spectral domain of plasmonic-like behaviour extends from dc to a few THz ($\approx$ 6THz). What could be noted here is that, in the reverse analogy, plasmonic metals can be considered as behaving like high-frequency superconductors with the electrons in the macroscopically coherent state created through the coupling with incident light.

Unfortunately, electromagnetic fields at the surface of a superconductor are almost completely expelled from the medium, making SPP excitations loosely bounded to the surface, weakly localised, and thus unsuitable for waveguiding applications. For instance, with YBCO at 1THz, the wave extends into vacuum for tens of wavelengths, and thus differs very little from a free-space plane wave propagating nearly parallel to the surface. In particular, such a mode has an effective refractive index $n_{\text{eff}} = 1.00000005 - j0.00000000033$, which is almost equivalent to a plane wave propagating along the interface in free-space with refractive index $n = 1$. Strong localisation is a very

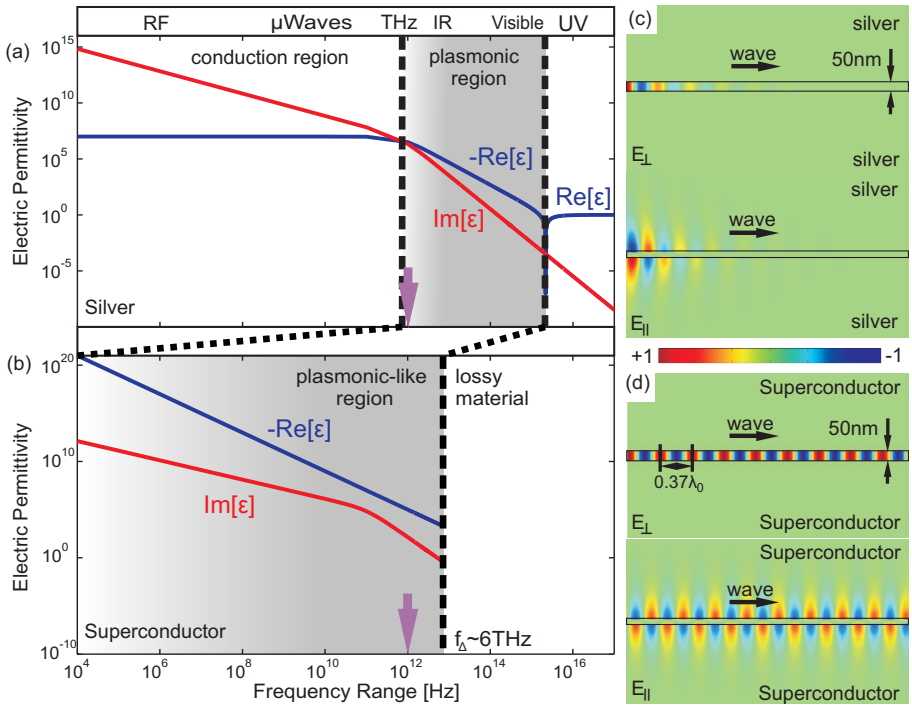


**Figure 4.6:** *Metallic and superconducting plasmonic waveguides. The permittivity of silver $\varepsilon$, derived from the Drude model (a), indicates plasmonic behaviour in the IR and visible parts of the spectrum. A high-temperature superconductor, using the two-fluid model (b), exhibits plasmonic-like behaviour at terahertz frequencies and below. Here, $f_\Delta$ is the superconductor's gap frequency. (c) and (d) Distribution of the electric field in a TM wave propagating through silver (c) and superconducting (d) parallel-plate waveguides at $1\,THz$. $E_\parallel$ and $E_\perp$ are components of the wave's electric field parallel and perpendicular to the propagation direction. In the silver waveguide the wave decays rapidly. The wave supported by the superconducting waveguide is 'compressed' (suitable for compact devices) and suffers negligible losses. Here $\lambda_0 = 0.3mm$ is the free-space wavelength.*

desirable feature from the perspective of using superconducting plasmons as information carriers. In order to improve the plasmonic behaviour of superconductors either proper structuring is necessary to suppress the Faraday inductance or operation at a higher range than the THz frequencies is needed in order for the the kinetic inductance to increase, as we have indicated in Section 4.1.2. Therefore, in superconducting films localisation can improve by significantly increasing the permittivity of the adjacent dielectric and/or by operating at frequencies close to the bandgap [119], at the expense of, unfortunately, higher losses.

### 4.2.1 Superconducting Plasmonic Waveguides: The Idea

We argue here that there is a much better way to unlock the potential of superconducting plasmonics: namely, by using the waveguide configuration that literally squeezes the plasmonic field. This can be achieved by trapping the plasmonic field laterally between two superconducting surfaces of a parallel-plate waveguide with a sub-wavelength gap of just a few tens of nanometres. Fig. 4.7(a) and (b) show a cross-section and a 3D view of the sub-wavelength parallel-plate waveguide, respectively. An alternative geometry that could be used, perhaps easier to fabricate, is that of a slot waveguide, created by a nanometer-wide slot made in a thin superconducting film, as shown in Fig. 4.7(c).

To prove our point, we simulated the propagation of electromagnetic fields at 1THz in a 50nm wide air gap between (i) two YBCO plates and (ii) two silver (Ag) plates and compared the results for the two waveguide systems. In our simulation the superconductor is described by using the two-fluid model that is described in Section A.2.2. Based on this model, we assume the existence of two non-interacting electronic subsystems contributing to the electromagnetic response of the superconductor at non-zero temperatures: Cooper pairs, that we call superconducting electrons, with purely inertial dynamics forming the super-current, and normal electrons participating in scattering and energy dissipation. Therefore, a generalised Drude model [169] is used for the dielectric function of such a two-component electron plasma at frequencies below the superconductor gap frequency $f_{\text{gap}} = 2\Delta/\hbar$, with $\Delta$ the necessary energy to break superconductivity:

$$\varepsilon = \varepsilon^{'} + j\varepsilon^{''} = 1 - \frac{\omega_s^2}{\omega^2} - \frac{\omega_n^2\tau^2}{\omega^2\tau^2+1} - j\frac{\omega_n^2\tau}{\omega(\omega^2\tau^2+1)}. \tag{4.50}$$

The second term in Eq. (4.50) represents the contribution from the non-dissipating super-current of Cooper pairs with plasma frequency $\omega_s = \sqrt{\frac{N_s e^2}{m\varepsilon_0}} = \frac{c}{\lambda_L}$, where $\lambda_L$ is the London penetration depth, $N_s$ is the density of the superconducting electrons, $m$ is their effective mass, and $\varepsilon_0$ is the free-space permittivity. The third and the fourth terms account for the normal electron plasma of resonant frequency $\omega_n = \sqrt{\frac{N_n e^2}{m\varepsilon_0}}$, where $N_n$ is the density of normal electrons and $\tau$ is their relaxation time. The balance between densities of the superconducting and normal electrons is described by the empirical Gorter-Casimir relation as given by Eq. (A.25-26). We choose the pa-

rameters in the superconductor model to describe $YBa_2Cu_3O_7$ with $T_c = 88$K and $N = 1.255 \times 10^{27}\mathrm{m}^{-3}$. At $T = T_c$ the normal electron plasma frequency has the value $\omega_n = 2 \times 10^{15}\mathrm{rad\ s}^{-1}$, which also corresponds to the super-current plasma frequency $\omega_s$ at $T = 0$. At intermediate temperatures these frequencies are determined by changes in the densities of superconducting and normal electrons according to the Gorter-Casimir relation. Additionally, $\tau$ is derived from the published experimental temperature dependence of the scattering rate of quasiparticles for $YBa_2Cu_3O_7$ films [126]. At the critical temperature we have $\tau_c = \frac{1}{\gamma_c} = 3.57 \times 10^{-14}$s, while the experimental temperature dependence of the scattering rate can be accurately fitted by a curve of the form:

$$\gamma(t = \frac{T}{T_c}) = \gamma_c \frac{t}{1 + at(t^{-\xi} - 1)}, \tag{4.51}$$

where $a$ and $\xi$ are fitting parameters. In our model we use $a = 10$ and $\xi = 1.5$ [170]. The dielectric constant of Ag is also calculated using the Drude model with a plasma frequency $\omega_n = 2\pi \times 2.1810^{15}$ rad $\mathrm{s}^{-1}$ and a scattering time $\tau = 2.297 \times 10^{-13}$s [146]. The propagation of the electromagnetic modes in the gap waveguide is modeled using the three dimensional Maxwell equations solver COMSOL Multiphysics, assuming an electric dipole excitation perpendicular to the superconducting surface inside the gap at the beginning of the waveguiding structure.

The results of our simulations are presented in Fig. 4.6(d). Quite remarkably, the superconducting waveguide supports a mode that is different from the usual TEM mode existing between perfectly conducting plates (parallel plate transmission line). It has a component of the electric field parallel to the propagation direction (TM mode) and is therefore analogous to the surface plasmon waves supported by metals at optical frequencies. At 1THz this mode has a wavelength several times shorter than in free space (good for miniaturization) and can propagate in a 50nm wide gap without significant attenuation for tens of millimetres (see Fig. 4.6(d)). In comparison, a TM mode of the same frequency in a silver waveguide of identical geometry is damped within a distance of just one wavelength (Fig. 4.6(c)).

### 4.2.2 Superconducting Plasmonic Waveguides: The Physics

Such a dramatic difference between nanoscale waveguiding efficiencies in the superconducting and the normal-conduction regimes can be explained by a simple analytical model[2], which generalises the analysis for any conductor and superconductor and any dielectric under specific conditions.

Consider a dielectric slab buried into either a conductor or a superconductor, forming a gap waveguide, and assume that $|\frac{\varepsilon'}{\varepsilon}| >> 1$ and $kd << 1$, where $\varepsilon'$ is the permittivity of the conductor or superconductor, $\varepsilon$ is the permittivity of the dielectric slab, $d$ is the thickness of the slab, and $k$ is the light-wave vector inside the dielectric. The first condition $\left(|\frac{\varepsilon'}{\varepsilon}| >> 1\right)$ is fulfilled in THz frequencies and below both for superconductors and conductors, since their relative permittivity, $\varepsilon^{'}$, is extremely large compared to that of the slab, $\varepsilon$. The guided modes are defined by the Fabry-Perot condition for waves propagating up and down the slab and reflecting from both interfaces, as shown in Fig. 4.7(a) :

$$1 - r^2 \exp(2jk_\perp d) = 0, \tag{4.52}$$

where

$$r = \frac{\varepsilon^{'} k_\perp - \varepsilon k_\perp^{'}}{\varepsilon^{'} k_\perp + \varepsilon k_\perp^{'}} \tag{4.53}$$

is the TM Fresnel reflection coefficient for the interface between the superconductor or conductor and the dielectric, $k_\perp = \sqrt{k^2 - k_\parallel^2}$ and $k_\perp^{'} = \sqrt{k^2 \frac{\varepsilon^{'}}{\varepsilon} - k_\parallel^2}$ are the wave vector components normal to the interface in the dielectric slab and superconductor or conductor, and $k_\parallel$ is the wave vector component parallel to the interface. This is shown in Fig. 4.7(a).

Eq. (4.52) reflects the fact that the wave must be in-phase after one round trip in the dielectric slab, including reflections at the upper and lower interfaces. Under the approximations made we could write $k_\perp^{'} \approx k\sqrt{\frac{\varepsilon^{'}}{\varepsilon}}$ and simplify Eq. (4.53), so that:

$$r \approx \frac{1 - \frac{k}{k_\perp \sqrt{\varepsilon^{'}/\varepsilon}}}{1 + \frac{k}{k_\perp \sqrt{\varepsilon^{'}/\varepsilon}}} \approx 1 - \frac{2k}{k_\perp \sqrt{\varepsilon^{'}/\varepsilon}}. \tag{4.54}$$

[2]This model was suggested by Prof. Javier Garcia de Abajo.

Substituting Eq. (4.54) in Eq. (4.52), we obtain:

$$1 - \frac{4k}{k_\perp \sqrt{\varepsilon^{'}/\varepsilon}} \approx 1 - 2jk_\perp d, \tag{4.55}$$

so that:

$$k_\perp \approx \sqrt{-\frac{2jk}{d\sqrt{\varepsilon^{'}/\varepsilon}}}. \tag{4.56}$$

From Eq. (4.56) the wave vector component which is parallel to the interface can be obtained:

$$k_\parallel = \sqrt{k^2 - k_\perp^2} \approx k\sqrt{1 + \frac{2j}{kd\sqrt{\varepsilon^{'}/\varepsilon}}}. \tag{4.57}$$

The expression given by Eq. (4.57) is valid if $|\frac{\varepsilon^{'}}{\varepsilon}| >> 1$ and $kd << 1$. The second condition is easily fulfilled for $d$-values in the micrometer and nanometer ranges. Since these two conditions affect the same denominator in Eq. (4.57), $k_\parallel$ can be either very close to or different from $k$, even in the case of an air gap ($\varepsilon = 1$). We consider the two limiting cases:

**Case I: The ideal superconductor limit** ($T \to 0$ and losses $\to 0$):
In this case $\varepsilon^{'} \sim -\omega_s^2/\omega^2$ which immediately leads to:

$$k_\parallel \approx k\sqrt{1 + \frac{2(\omega/\omega_s)\sqrt{\varepsilon}}{kd}}. \tag{4.58}$$

Expression given by Eq. (4.58) reflects the fact that the mode propagates in an ideal superconducting gap waveguide without losses ($k_\parallel$ is real) and its dispersion can significantly deviate from the light line for small $d$, which represents the strong confinement case.

**Case II: The perfect conductor limit** (becoming better approximation as $\omega \to 0$):
In this case $\varepsilon^{'} \sim -j\omega_n^2\tau/\omega$, (in real conductors the imaginary part of permittivity dominates) which leads to:

$$k_\parallel \approx k\sqrt{1 + \frac{2(\omega/\omega_n)}{kd}\sqrt{\frac{\varepsilon}{j\omega\tau}}}. \tag{4.59}$$

Thus, there are significant losses for the mode propagating in a perfect conducting gap waveguide, and the level of losses increases with the departure of $k_{||}$ from the light line, i.e., when the mode is subjected to stronger confinement ($d \rightarrow 0$), rendering metals completely incapable of nanoscale waveguiding at low frequencies.

### 4.2.3 Superconducting Plasmonic Waveguides: The results

Low-loss superconducting waveguides are a promising solution for large bandwidth terahertz and sub-millimetre waves plasmonic circuits. The term 'large bandwidth' corresponds to their ability to carry signals of higher bandwidth compared to circuits operating in the microwave or radio-wave regimes. This is enabled by their key characteristics, such as the strong lateral confinement and longitudinal compression necessary for high density-integration, but without dissipative losses that hamper plasmonic applications at optical frequencies. As an extra desirable feature, superconducting plasmonic waveguides enable access to this higher bandwidth and faster data transfer rates due to their extremely weak dispersion. This is demonstrated below for superconducting YBCO at 40K for both gap- and slot-waveguide configurations (see Fig. 4.7(d)). For the gap mode we can reach an analytic close-form expression for the dispersion equation (Eq. (4.41)), which is of a transcendental form. Thus, we employ the scheme described in [171] to derive its roots (this is an exact solution derivation and not an approximation as described in the intuitional analytic model of the previous subsection). Unfortunately, there are no close-form expressions for the dispersion equation of the slot waveguide plasmonic modes. For this case, the effective refractive index and propagation distance are retrieved from the results of COMSOL simulations.

Figure 4.7(d) shows the dispersion curves calculated in the 0.5-1.5 THz range of frequencies for the modes propagating in 50nm wide gap and slot waveguides. Similar to free-space propagation in the air, the dispersion of the bounded superconducting plasmons here appears to be linear, effectively corresponding to free-space propagation in denser dielectrics. The slope of the dispersion curves can be decreased further by increasing the refractive index of the guiding regions (by using a denser dielectric), but more importantly, the longitudinal compression of the modes can be efficiently controlled by the size of the cross-section and the temperature of the waveguides. As it is clear from Fig. 4.7(e), the effective refractive index of the plasmonic mode in the gap

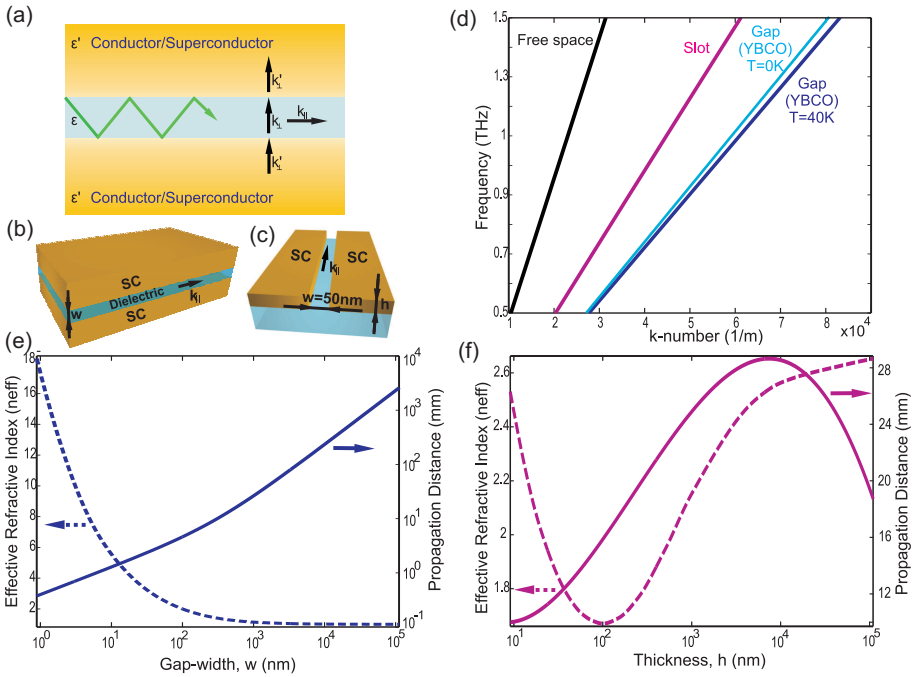


**Figure 4.7:** *Dispersion and propagation characteristics of superconducting YBCO plasmonic waveguides at 40K. (a) Schematic cross-section of the gap-plasmon waveguide. (b-c) 3D schematics of the gap-plasmon and slot waveguide configurations used in the simulations. (d) Dispersion curves calculated for the terahertz modes propagating in free-space (black) and superconducting gap (blue) and slot (magenta) waveguides. The light blue curve represents the mode dispersion in the superconducting gap waveguide calculated analytically (superconductor at 0K). (e) Effective refractive index (dotted curve) and propagation distance (solid curve) of the gap-plasmon calculated at 1THz as a function of the gap width, w. (f) Effective refractive index (dotted curve) and propagation distance (solid curve) of the slot-plasmon calculated at 1THz as a function of the superconducting film thickness, h.*

waveguide monotonically increases with decreasing gap size and can reach a value of 5 for a gap as large as 10nm. Similar to optical plasmons, of-course, the superconducting ones are also subject to the trade-off between confinement and propagation distance, illustrated in the same figure. However, considering a nanoscale confinement that was so far exclusive of optical plasmons, the propagation distance of its superconducting counterpart at 1THz extends here to a colossal value of 6.5mm (about 60 effective wavelengths). Interestingly, the effective refractive index and the propagation distance is significantly affected by the temperature of the waveguide. The propagation distance can be in the range of meters near 10K, while it drops to just a fraction of the guided wavelength near the critical temperature. Exactly opposite in trend is the temperature dependence of the effective refractive index, illustrated in Fig. 4.8. We note here that decreasing the temperature results in the reduction of the kinetic inductance of the

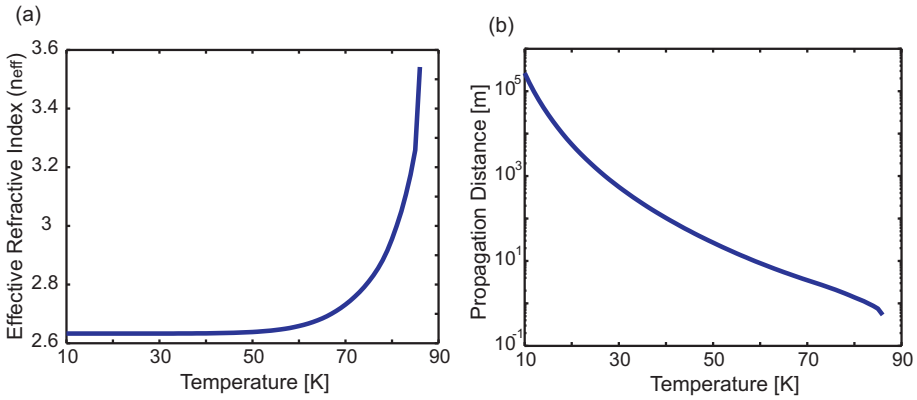


**Figure 4.8:** *Temperature-dependence of (a) the effective refractive index ($n_{\text{eff}}$) and (b) the propagation distance of the superconducting gap-plasmon mode. The width of the structure is $w = 50nm$ and the frequency is $1\,THz$.*

superconductor, while reducing the gap size suppresses the Faraday inductance of the structure [119, 140]. An optimised choice of gap size and temperature can result in a high ratio of the kinetic to the Faraday inductance, which enhances the demonstrated plasmonic behaviour and at the same time achieves the desired propagation length.

For the slot waveguide configuration (which is technologically more appealing), the plasmonic mode is confined laterally in two dimensions, and the dependances of its refractive index and propagation distance on the parameters of the waveguide cross-section are more complicated, as presented in Fig. 4.7(f). As we decrease the thickness $h$ of the slot, the effective refractive index is initially decreasing, since the mode in this structure is confined only in one transversal dimension compared to the gap-plasmon mode. Therefore, as we shrink the thickness, a larger part of the mode is propagating in the surrounding dielectric environment. For example, the effective refractive index of the mode residing in the 50nm wide slot reaches a minimum value of 1.67 for a superconducting film thickness of 100nm. However, after this point the supported mode starts transforming into a corner-edge bounded mode, which explains the increase in both the effective refractive index and the losses as we further reduce the thickness h of the slot, due to the strongly bounded nature of the latter mode. In addition, the propagation distance of the plasmonic mode in such a waveguide at 1THz is of the order of a few tens of millimetres, which corresponds to an impressive value of a 100 effective wavelengths.

### 4.2.4 Superconducting Plasmonic Waveguides: Challenges and Comparison with other Technologies

Obviously, in order to imply that plasmonics could be used as a data handling and processing paradigm in the same way as photonics technology is exploited, efficient techniques for active manipulation of plasmon signals are necessary [172]. In this respect, superconductors have another important advantage over metals: the electromagnetic characteristics of superconductors may be readily altered, especially close to their critical temperature, by external stimuli such as magnetic fields, optical illumination, surface currents or heat. Our work on superconducting metamaterials already has shown the ability to use temperature control [118], but also magnetic fields were used in [110]. More recently the appealing control through the application of electric currents in superconducting metamaterials was shown in [113]. This opens up a new path towards 'active plasmonic' applications, where the plasmon signal can be efficiently controlled in data processing and interconnect applications.

In essence, high-temperature superconducting waveguides constitute a promising avenue for developing ultra-compact terahertz data processing circuits, providing a superior alternative to sub-millimeter metal single-wire transmission lines and circular waveguides [7, 173, 174]. Also, propagation distances of up to several meters, and truly nanoscale confinement of the guided terahertz plasmonic modes, which can be actively manipulated through various easy-to-implement routes, make the superconducting plasmonic waveguides a strong candidate for terahertz wave propagation compared to other possible solutions based on the use of semiconductors, corrugated metal surfaces or graphene. Indeed, although semiconductors can exhibit plasmonic behavior in the range of 1-10 THz with lower losses compared to metals, their conductance and kinetic inductance are both still substantially lower than in superconductors, resulting in shorter mode propagation lengths and weaker confinement. For example, for a semiconductor such as InSb, which has one of the lowest scattering rates of all III-IV compounds with $\varepsilon = -14 - j12$ [175], the propagation length of a surface guided SPP mode at 1THz is only 1.3mm, which is around four effective wavelengths, whereas its field extends in vacuum for more than 0.18mm. If YBCO was replaced by InSb in the gap waveguide configuration, the propagation distance of the gap mode would

be 6.4$\mu$m, only a fraction of the mode's effective wavelength of 14.4$\mu$m. Corrugated metal surfaces can, in principle, guide terahertz waves in the form of spoof plasmons, but they offer no means of active control, whereas the scale of the mode localisation is much larger than in the superconducting waveguides, typically in the order of tens of microns. Finally, the efficiency of waveguides based on graphene, which has been shown to support plasmonic excitations at terahertz frequencies [176], can be severely limited by imperfections in the actual samples [177].

The main drawback of superconducting plasmonic technology is the unavoidable operation only in cryogenic temperatures. However, the cryo-cooling requirement for the superconducting waveguides is no longer a serious technological limitation, especially in the case of high-temperature superconductors, as compact cryogenic devices are now widely deployed in telecommunications (e.g., microwave filters) and in sensing equipment.

## 4.3 Epilogue

In this chapter, we have demonstrated a direct analogy between the electromagnetic properties of superconductors at frequencies up to the superconducting gap frequency (almost 6 THz for YBCO) and plasmonic metals in the optical part of the spectrum. We have also identified the existence of a surface plasmonic bound mode in superconducting waveguide structures, that is closely connected to surface plasmon polaritons in noble metals. This is a peculiar low-frequency, low-loss, and low-dispersion mode that can be guided for tens of wavelengths and be confined in structures with nanoscale transversal dimensions, demonstrating a significant application potential.

# 5

# Generating THz Radiation

The difficulty of generating THz fields is probably the first among all challenges of THz technology that we need to overcome in order to utilize this spectral band for scientific investigation and commercial applications. In fact, the inability of conventional electronics to work efficiently above several hundreds of GHz and the lack of conventional lasing devices in the THz range signify the challenges involved in THz generation.

Most of the demonstrated sources usually have very low efficiencies in terms of generating THz radiation and cannot achieve useful power levels (typically higher than in the range from 0.1mW to 1W). However, over the last years many interesting approaches for THz generation appeared, including the utilization of photoconductive surfaces [10, 11], frequency multipliers [49], and, most commonly, Quantum-Cascade Lasers (QCLs) [50].

In our work, reported in this chapter, we focus on the generation of high-intensity THz magnetic fields. Strong magnetic pulses at THz frequencies are desirable for applications such as magnetic data recording and time-domain magnetic spectroscopy (important for materials characterization). Here, we theoretically demonstrate that metamaterial arrays composed of bimetallic rings, when illuminated by femtosecond optical pulses, can lead to the generation of magnetic pulses localised in the ring cavity with peak-amplitudes of the order of one Tesla[1].

The chapter starts with a description of the thermoelectric effect, followed by a description of the mechanisms involved in high magnetic fields generation through thermoelectric metamaterials. This discussion concludes with the results of our analysis for

[1]This work has been conducted in collaboration with Evangelos Atmatzakis.

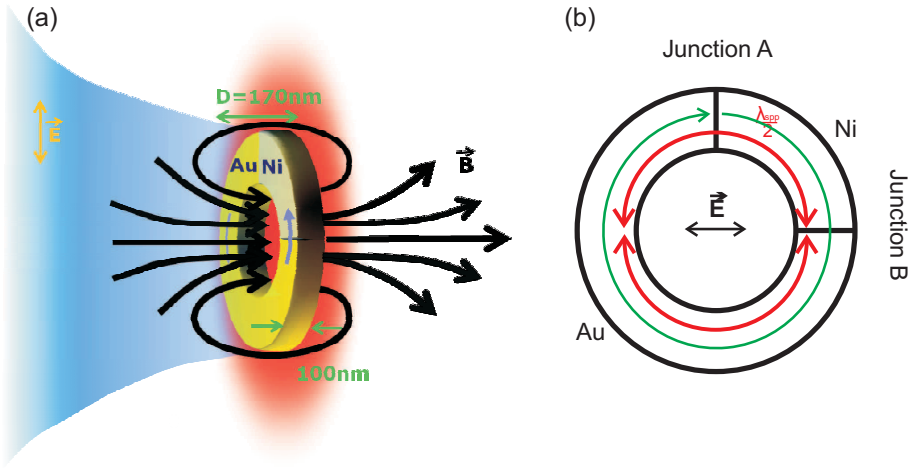


**Figure 5.1:** *(a) A conceptual representation of an Au/Ni nanoring able to absorb energy in the form of heat from the electromagnetic field when excited at its plasmonic resonance wavelength, and transform it into intense sub-ps magnetic field pulses. (b) At the plasmonic resonance of the ring, a dipole current (red) oscillating at the incident light frequency is excited, leading to the absorption and subsequent heating of conduction-electrons. A strong, non-oscillating thermoelectric current (green) is then produced in the created short-circuited thermocouple, driven by the conduction-electron temperature difference between the cold (B) and hot (A) Au/Ni junctions.*

a thermoelectric metamaterial array of bimetallic gold (Au)/nickel (Ni) rings.

## 5.1 Introduction to Thermoelectric Metamaterials

While most metamaterials act as passive elements, in the form of energy storage devices, here, we present a conceptually different class of metamaterials, which we call 'thermoelectric metamaterials'. The main property of the latter is their ability to transform high frequency optical waves into longer-wavelength THz radiation. In essence, a metamaterial array of ring structures made of two different metal composites, such as gold and nickel, can utilize the plasmonic and thermoelectric properties of the metallic pair in order to form nanostructured sources of high intensity magnetic fields with ps-duration.

In simple terms, in thermoelectric metamaterials, the meta-atoms are rings consisting of three quadrants of Au and one quadrant of Ni, forming both a plasmonic resonator and a thermocouple pair, as shown in Fig. 5.1. Each ring is 100nm-thick, has an inner diameter of 70nm, an outer diameter of 170nm, and is embedded in glass. The

excitation of the ring occurs with an optical pulse at the wavelength of 920nm with polarisation along one of the Au/Ni junctions. The main idea lies on the fact that the lowest-order dipole plasmon resonance of the ring, which is on the same wavelength as the optical excitation, leads to enhanced absorption of the wave's optical energy near one of the Au/Ni junctions (the junction denoted with the letter A in Fig. 5.1(b)). In a homogeneous gold ring, symmetry would lead to resonant absorption at two diametrically opposite regions, however, the asymmetry imposed by the bimetallic composite, leads to stronger absorption near the Au/Ni interface. This nonuniform absorption produces a steep gradient of the electron temperature along the ring, and subsequently, a net displacement of charge carriers from hotter to colder regions, giving rise to a Seebeck electromotive force (emf). In the Au/Ni thermocouple, charge carriers in gold and nickel are electrons and holes, respectively, so that the resulting thermoelectric current contributes along the same direction on either side of each metal junction [178], leading to a transient circular current in the ring. Since femtosecond pulses give rise to temperature differences of several thousand degrees in the conduction electron gas, the circular thermoelectric current created is very strong before thermalisation into the atomic lattice takes place within a few picoseconds. Finally, this transient circular current generates a magnetic field, mainly perpendicular to the plane of the ring (black lines in Fig. 5.1(a)), that lies in the THz domain, as it is implied by the time scale of the thermalisation time of the lattice.

## 5.2 The Seebeck Effect

The Seebeck effect describes the conversion of temperature differences directly into electricity and is named after the Baltic German physicist Thomas John Seebeck. In 1821, T. J. Seebeck discovered that a compass needle is deflected by a closed loop formed by two metals joined in two places when there is a temperature difference between the junctions. This was a result of the different response of each of the metals to the temperature difference imposed, resulting in a current loop and an induced magnetic field. However, since Seebeck did not recognize that there was an electric current involved, he called the phenomenon: 'the thermomagnetic effect'. It was, actually, the Danish physicist Hans Christian Oersted that rectified the mistake and used the term

thermoelectricity.

In essence, the Seebeck effect is the direct conversion of temperature differences to electric voltage and vice-versa. Consider, for example, the case of a single metallic bar heated at one of its ends and kept at a constant very low temperature at the other, as shown in Fig. 5.2(a). The electrons in the hot region are more restless due to their higher kinetic energies. As a result, they move with higher velocities compared to those in the cold region and a net diffusion of electrons from the hot end towards the cold end takes place, leaving behind exposed positive metal ions in the hot region and accumulating electrons in the cold region. This thermal motion of electrons leads to the creation of a thermal current. Note that this current will disappear only when the number of accumulated charges at each side of the bar is high enough to build an electric field able to give rise to a normal current flow equal in magnitude and opposite in direction to the thermal current. Then a typical situation of a dynamic equilibrium occurs between the two currents.

The potential difference $\Delta V$ across a piece of metal due to a temperature difference $\Delta T$ is expressed through a coefficient called Seebeck and denoted with $S$, which depends on temperature $T$ [53]. Therefore the Seebeck coefficient is given by the formula:

$$S(T) = \frac{\mathrm{d}V}{\mathrm{d}T}. \tag{5.1}$$

The electric field created by a temperature gradient in this case is:

$$E_{\mathrm{th}} = S(T)\nabla T. \tag{5.2}$$

In reality, if we try to measure the voltage drop $\Delta V$ across the metallic bar by using wires of the same metal (as that of the bar) connected to a voltmeter, as shown in Fig. 5.2(b), no net voltage will be measured by the voltmeter. The reason why this occurs is that the potential difference created along the wires in this case is opposite to the voltage drop across the bar. The solution to this problem is to use wires made of a different metal from that of the bar, thus, having a different Seebeck coefficient. Such a device is called a thermocouple and is illustrated in Fig. 5.2(c).

Unfortunately, current loops, which can induce strong magnetic fields, cannot be created with such an open-end design.

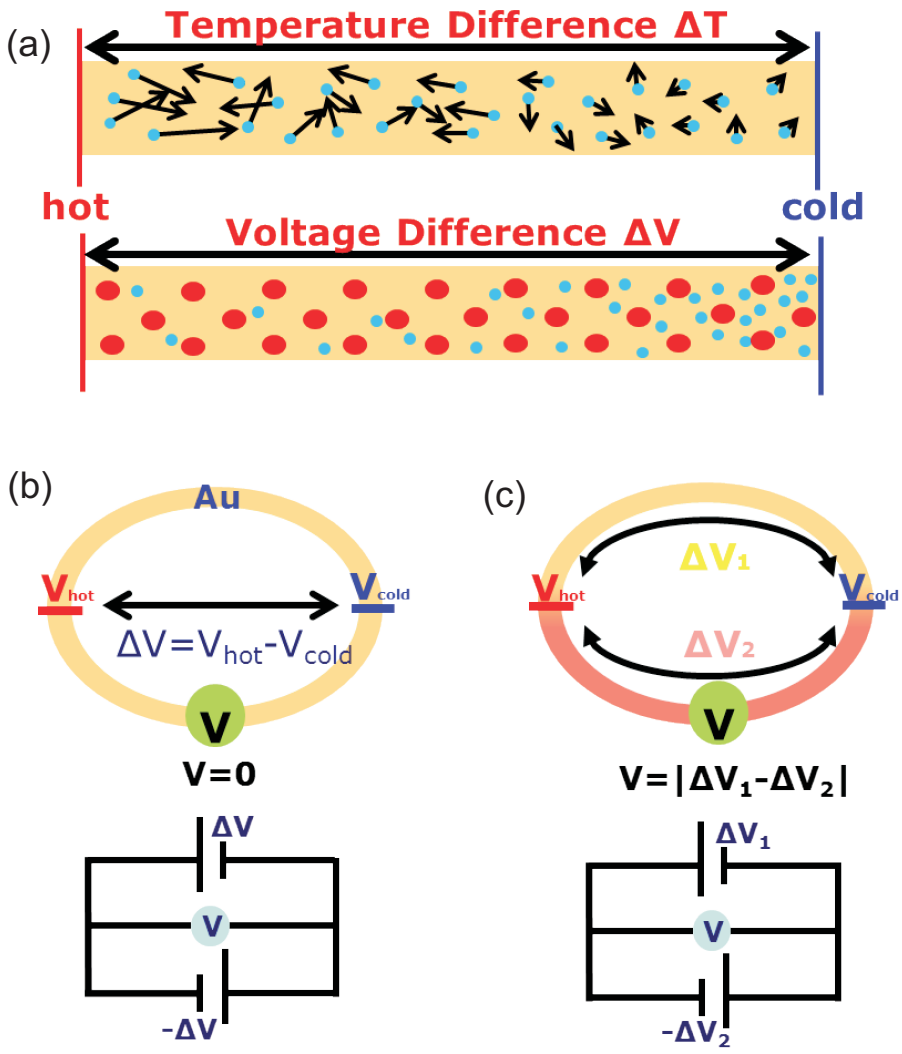


**Figure 5.2:** *(a) A temperature gradient due to Seebeck effect leads to a voltage gradient. The arrows represent the velocities of electrons (blue circles). High temperatures increase the kinetic energy of electrons, which start diffusing towards the colder side of the bar. In the end, a voltage barrier has been built up inside the bar due to electrostatic forces that opposes the movement of hot electrons. (b) A single material network cannot act as a voltage source created by the Seebeck effect. Due to the symmetry of the structure the same potential difference exists in both paths between the hot and cold spots, eliminating the ability to measure any voltage. A circuit analogue of this case is presented. (c) The solution to this problem is the use of two materials, having different Seebeck coefficients. Such a device is called a thermocouple and its electric circuit analogue is presented.*

## 5.3 The Plasmonic Resonance of a Metallic Ring

Aiming to design a magnetic field source of nanometre size, we try to create loops of currents in our meta-atoms. From this perspective, a metallic ring design seems like

a natural choice. Such a ring, when it is excited by a wave of proper polarisation and wavelength, can exhibit a plasmonic resonance at which enhanced absorption of the wave's energy occurs. Eventually, the energy stored in the plasmonic resonator will be dissipated and transformed into heat through Ohmic losses. The generated heat increases the temperature of the ring. Since energy dissipation in the case of a plasmonic resonator occurs more drastically in some parts of the structure than others, the temperature distribution across the ring is non-uniform, resulting in some cases to the formation of circulating thermal currents and the subsequent induction of magnetic fields.

We start by examining the case of a ring made of gold, which is a low-loss metal able to show a strong plasmonic response. The ring is 100nm-thick, with an inner diameter of 70nm and a linewidth of 50nm, embedded in glass ($n = 1.45$). The dimensions of the ring have been chosen in such a way that the resulting structure falls in the fabrication capabilities of today. Such a ring, when excited by an optical linearly polarised wave, has a plasmonic dipole resonance at 940nm (see the simulated transmission and absorption spectrum in Fig. 5.3(a)). This resonance is created when the circumference of the ring is equal to the effective wavelength of the supported SPP mode ($\lambda_{\text{spp}}$). This mode is excited on the surface of the ring by the electric field of the incident wave, as shown in Fig. 5.1(b). At resonance, the ring absorbs energy from the external field, which is transformed into a scattered field (radiation losses) and Joule losses. Since on resonance the electric field magnitude is maximum on the sections of the ring that coincide with the direction of the polarisation of the wave, maximum currents exist in between these sections. Thus, at the places that currents are maximum Ohmic losses are also maximum (assuming that the resistance of the ring is uniform across the structure). Fig. 5.3(a) shows both the distribution of the magnitude of the total electric field on the surface of the ring and the places that maximum Joule losses occur. Since Joule losses are not the same all over the ring, the resistive heating that occurs leads to a temperature gradient over the ring structure; such a temperature gradient is necessary for the Seebeck effect. Unfortunately, due to the symmetry of the golden nanoring structure and the excitation wave, the generation of a current loop is impossible. This situation is analogous to connecting two sources of opposite polarity in parallel. No current will flow in the loop (see Fig. 5.2(b)).

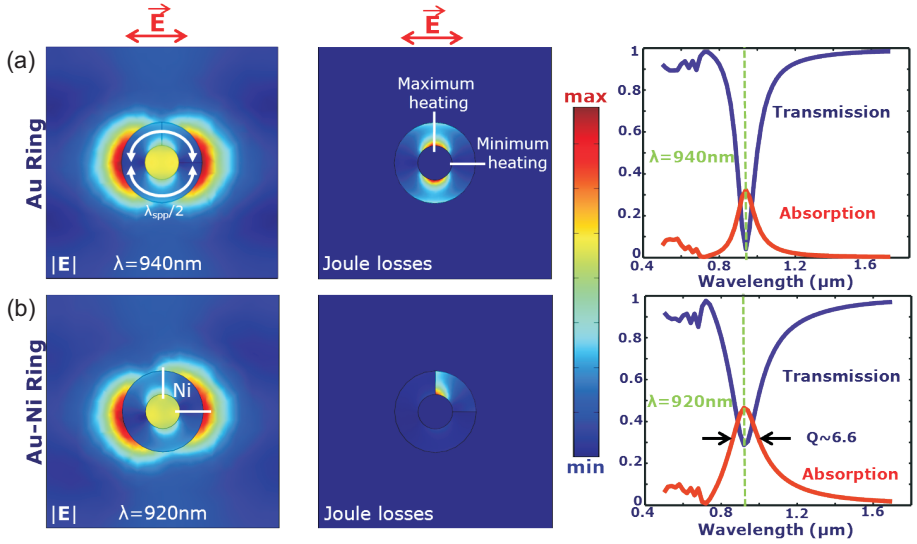


**Figure 5.3:** *Simulation results: (a) The electric field magnitude and Joule losses distribution at the resonant wavelength of* $\lambda = 940nm$*, shown for the plane passing through the middle of an Au ring. Transmission and absorption spectra are presented. (b) The same as in (a) but for an Au/Ni ring. White lines enclose the area where Au has been replaced by Ni. The resonance has been shifted to* $\lambda = 920nm$ *and broadened due to the increased losses of Ni. The ring is* $100nm$*-thick, with an inner diameter of* $70nm$ *and a linewidth of* $50nm$*, embedded in glass* ($n = 1.45$).

Similarly to the case of measuring the voltage across a metallic bar, we have to use two different metals in order to form a bimetallic ring which allows a current loop to be induced within it. In this case, when the two interfaces between the two metals are at different temperatures, a net emf will appear able to induce currents. To maximize the induced thermal currents, we place one of the junctions exactly where the resistive heating is maximum, while the other one is placed at the place where the resistive heating is minimum. In the case of the golden nanoring, such a condition is fulfilled by placing the junctions 90° apart, with one of them coinciding with the direction of the polarisation of the wave (see Fig. 5.3(a)). In the case of a bimetallic ring, such a condition although not necessarily optimum, results in strong circulating currents as will be shown in the following sections. Thus, we design the ring with 3/4 made of gold and the remainder 1/4 made of a different metal. For the choice of the second metal three conditions need to be fulfilled simultaneously. First of all, the metal chosen should not alter significantly the plasmonic properties of the ring, so that the ring can act as a plasmonic dipole resonator. Second, the chosen metal should form a good thermal-

pair with gold, since the created emf would be proportional to the difference of the Seebeck coefficients of the metals. Maximizing this difference is of crucial importance for achieving strong thermal currents. Third of all, this metal should be easily handled and used in nanofabrication procedures. Nickel, from this perspective, fulfills all three conditions.

An Au/Ni ring designed under the stated conditions and embedded in silica has its dipole plasmonic resonance at 920nm. This resonance has a quality factor of 6.6. Fig. 5.3(b) shows the simulated electric field magnitude distribution, the Joule losses distribution, and the estimated transmission and absorption spectra of such an Au/Ni nanoring. Of course, inserting the Ni section in the formation of the ring breaks the symmetry of the structure, which in this case appears to have enhanced resistive heating near the Au/Ni junction (junction A) compared to the diametrically opposite area of Au only. This is a result of the higher resistance of Ni compared to Au. In fact, this can be seen by comparing the permittivities of the two metals: Au has a relative permittivity $\varepsilon_r = -33.56 - j1.93$ at 920nm, while for Ni we have $\varepsilon_r = -15.47 - j26.03$ [175]. The increased value of the imaginary part for the relative permittivity of Ni, explains why the currents created provoke higher Joule losses at the side that Ni exists compared to the all Au side (see inset of Fig. 5.4(a)).

In essence, the core idea is the exploitation of the losses occurring in a plasmonic resonator as a transformation mechanism from optical wave energy to heat generation, subsequent temperature increase, and through the Seebeck effect to THz currents generation. Therefore, losses, considered the weak point in plasmonic resonators, here, are the driving engine of the THz-radiation generator.

## 5.4 Light-pulse Absorption & Temperature Dynamics

From the previous sections it has been clear that the source of the temperature gradient created across the ring is due to the Ohmic losses of the plasmonic resonator. It is obvious, then, that an increase of dissipated energy due to Ohmic losses will result in a stronger heat source, leading to the formation of steeper temperature gradients. This can be more easily achieved with the use of a pulse rather than a CW laser source for exciting the ring at the resonant frequency. Thus, we consider a short

Gaussian pulse of $\sim 2\Delta t_{\text{pulse}} = 100$fs duration, centered at a wavelength of 920nm, and incident on the ring with linear polarisation as shown in Fig. 5.1(a). The pulse fluence is $11.3\text{J/m}^2$. Since the pulse duration is much longer than the period of the wave ($T = 3.1$ fs) and the time it takes for a resonance to be established on the ring structure, which is of the order of $\sim QT = 20$ps, the absorbed power density (i.e., the position- and time-dependent power absorbed per unit volume inside the ring) is approximated as $p(\mathbf{r}, t) = p(\mathbf{r})f(t)$, assuming that it follows the pulse temporal profile $f(t) = \exp\left[-t^2/\left(\Delta t_{\text{pulse}}\right)^2\right]$, multiplied by the peak absorption density $p(\mathbf{r})$, which we calculate for a plane wave with the same intensity as the pulse maximum. In reality, there is a small delay $t_0$ between the maximum of the optical pulse and the maximum of the absorbed energy due to causality. This only leads to a small time-shift and is, therefore, neglected. These assumptions simplify the problem, since we avoid the calculation of the transient response created when a fs-pulse excites the structure.

The absorbed energy is initially deposited on the surface electrons of Au and Ni. As a result, their temperature, and subsequently their kinetic energies, are increased. Finally, through scattering with phonons, this energy will be transferred to the lattice. A widely accepted and developed model used to predict this heat transfer process is the two-temperature model [178], which can be expressed through the two coupled equations [178]:

$$C_e \frac{\partial T_e}{\partial t} = \nabla(k_e \nabla T_e) - G(T_e - T_l) + p, \tag{5.3}$$

$$C_l \frac{\partial T_l}{\partial t} = \nabla(k_l \nabla T_l) + G(T_e - T_l), \tag{5.4}$$

where $C$ is the heat capacity, $k$ the thermal conductivity, and $T$ is the temperature. The index $e$ corresponds to the conduction-electrons, while the index $l$ to the atomic-lattice. Following its derivation, the conduction-electrons and atomic-lattice subsystems have their own temperatures $T_e(\mathbf{r}, t)$ and $T_l(\mathbf{r}, t)$ respectively. The temperature dynamics of each of these subsystems evolves over a different time scale. Since we assume that the heating produced through $p(\mathbf{r}, t)$ is entirely transferred from the light to the conduction electrons, we use the term $p(\mathbf{r}, t)$ as a source term for the thermal diffusion equation of the electronic subsystem. In addition, the electronic and the lattice subsystems are coupled through a term $G$ that accounts for the heat transfer from the former to

the latter and is proportional to their instantaneous temperature difference. Since the electrons reach local thermal equilibrium in a short time compared to the characteristic times for thermal diffusion and lattice thermalisation, the thermal diffusion equations are solved simultaneously for the electronic and lattice subsystems. It has to be stated that all the involved parameters $C$, $k$, and $G$ are temperature dependent both for Au and Ni, which leads to a strongly nonlinear problem.

For the estimation of the thermal parameters as a function of temperature, both for Au and Ni, we have to consider that the scattering rates in these metals, after ultrashort pulsed laser heating, can be drastically different from those predicted in the free electron theory [178]. The large electron temperatures achieved can lead to excitations of electron orbitals far below the Fermi energy level. Thus, we have to account for these effects into the estimation of the thermal coefficients involved in the Eq. (5.3-4). We use values of the coefficients compiled from [178–185], as we discuss in Section 5.7 of this chapter. For simplicity, we ignore the effect of hetero-junction thermal barriers, which should contribute to create higher temperature gradients and stronger magnetic fields.

## 5.5 Thermal Currents & Magnetic Induction

From the solution of Eq. (5.3-4), we derive a thermoelectric emf equal to $S(T_e)\nabla T_e$, where $S$ is the Seebeck coefficient that depends on the temperature of conduction electrons. This allows us to write the thermoelectric current as:

$$\mathbf{j}(\mathbf{r},t) = \sigma(T_e)(S(T_e)\nabla T_e - \nabla V), \tag{5.5}$$

where $\sigma$ is the temperature-dependent electric conductivity and $V$ represents the potential displayed in response to the thermoelectric source because of charge displacements and accumulation in certain places. Since the time scale of these effects is in the order of $10^{-18}$s, and, thus, faster than the diffusion effects, they cannot be omitted. Values of temperature-dependent $\sigma$ and $S$ for Au and Ni are calculated according to [178,184] (refer to Section 5.7).

Since $T_e$ varies smoothly over hundreds of femtoseconds, involving frequencies below the mid-infrared, we can assume that the metals behave almost as perfect conduc-

tors (see comments following Eq. (A.9)), so that the thermoelectric current is quasi-stationary and the continuity equation:

$$\frac{\partial \rho(\mathbf{r},t)}{\partial t} + \nabla \mathbf{j}(\mathbf{r},t) = 0, \tag{5.6}$$

reduces to the vanishing of the $\nabla \mathbf{j}(\mathbf{r},t)$ term. This is equivalent to neglecting the self-inductance of the thermoelectric current. Then, combining Eq. (5.6) with Eq. (5.5), we get:

$$\nabla \cdot \sigma(T_e) \nabla V = \nabla \cdot \sigma(T_e) S(T_e) \nabla T_e, \tag{5.7}$$

which is formally equivalent to the Poisson equation with a local response function $\sigma$ and a source term $-\nabla \cdot \sigma S \nabla T_e$. Incidentally, by setting $\sigma = 0$ outside the ring structure, Eq. (5.7) guarantees the vanishing of the normal current at the ring boundaries. We obtain $V$ by solving Eq. (5.7), and this is then inserted into Eq. (5.5) to estimate $\mathbf{j}(\mathbf{r},t)$.

Finally, we use the thermoelectric induced current $\mathbf{j}(\mathbf{r},t)$ in order to obtain the resulting magnetic induction. From classical electromagnetic theory we have [185]:

$$\mathbf{B}(\mathbf{r},t) = \frac{\mu_0}{4\pi} \int \mathrm{d}^3\mathbf{r}' \frac{\mathbf{j} \times (\mathbf{r} - \mathbf{r}')}{|\mathbf{r} - \mathbf{r}'|^3}, \tag{5.8}$$

where the integral is extended over the volume of the ring. Here we have used the magnetostatic approach, since the dimensions of the nanoring structure are much smaller than the emitted wavelengths. Thus, the nanoring behaves as a magnetic dipole source.

## 5.6 The Intense Magnetic Pulse Generator

At this point, the design considerations of the Au/Ni rings have been justified and the physical mechanisms involved have been described. It is obvious that in order to calculate the magnetic field generation induced by an optical pulse with the mediation of thermoelectric currents in bimetallic Au/Ni rings, the tedious task of solving a system of coupled equations involving the energy absorption of the plasmonic resonator, the heat diffusion problem, the resulting thermoelectric currents estimation problem, and the magnetic field calculation itself has to be carried out. For this reason, we have used the commercial FEM solver Comsol Multiphysics, which is able to perform the calculations involved in the various coupled physical models of this problem.

From the simulations conducted and with an incident pulse fluence of $11.3\text{J/m}^2$, we estimate that the energy transferred to the ring is $\sim 1.4\text{pJ}$, since the absorption cross-section of the dipole plasmonic resonator is $\sim 0.12\mu\text{m}^2$. Thus, we get the time evolution of $T_e$ and $T_l$ temperatures at the two Au/Ni interfaces, illustrated in Fig. 5.4(a). Following an initial excitation with the ultrafast optical pulse, the electron-gas temperature rapidly rises at both junctions, reaching peak values shortly after the maximum of the incident pulse. The nickel section of the ring produces a considerable temperature difference between the two junctions: electrons at the hot junction (A) reach a peak temperature of $\sim 6000\text{K}$, which is approximately twice the temperature of the cold junction electrons (B). The peak temperature at B occurs nearly 1ps after the maximum of A, as a result of hot-electrons diffusion. Over this short time interval, the absorbed energy remains almost entirely in the electron gas, while thermalization of the Au and Ni lattices, initially at 300K, takes place over a time scale of several picoseconds. The lattice and electron temperatures become nearly identical $\sim 10\text{ps}$ after irradiation, when both junctions are at $\sim 600\text{K}$, well below the melting temperature of the ring materials. Finally, the ring cools back to room temperature after a few nanoseconds due to diffusion through the surrounding glass.

Actually, the decay from maximum heating reveals three different time scales: a fast decay ($\sim$ 1ps) produced by thermal diffusion within the electron gases of the two metals; an intermediate decay ($\sim$ 10ps) that can be ascribed to thermalisation of the electrons into the lattice via electron-phonon scattering; and a slow decay ($\sim$ nanoseconds) arising from thermalisation into the surrounding glass. This picture is consistent with the temperature dependence of the involved materials' parameters, as presented in Section 5.7.

The temperature gradient between the two junctions of metals with different Seebeck coefficients produces an emf that drives a thermoelectric current along the ring's circumference, as we have already explained. Because of the high electron temperatures involved, the thermoelectric current density in the confined ring geometry reaches values as high as $\sim 10^{13}\text{A/m}^2$. Fig. 5.4(b) illustrates the temporal evolution of the current density through junction A, which follows quite closely the temperature difference over time, with a maximum occurring $\sim 100\text{fs}$ after the peak of the excitation pulse. The current distribution on the ring surface (shown in Fig. 5.4(c)) reveals a dominant

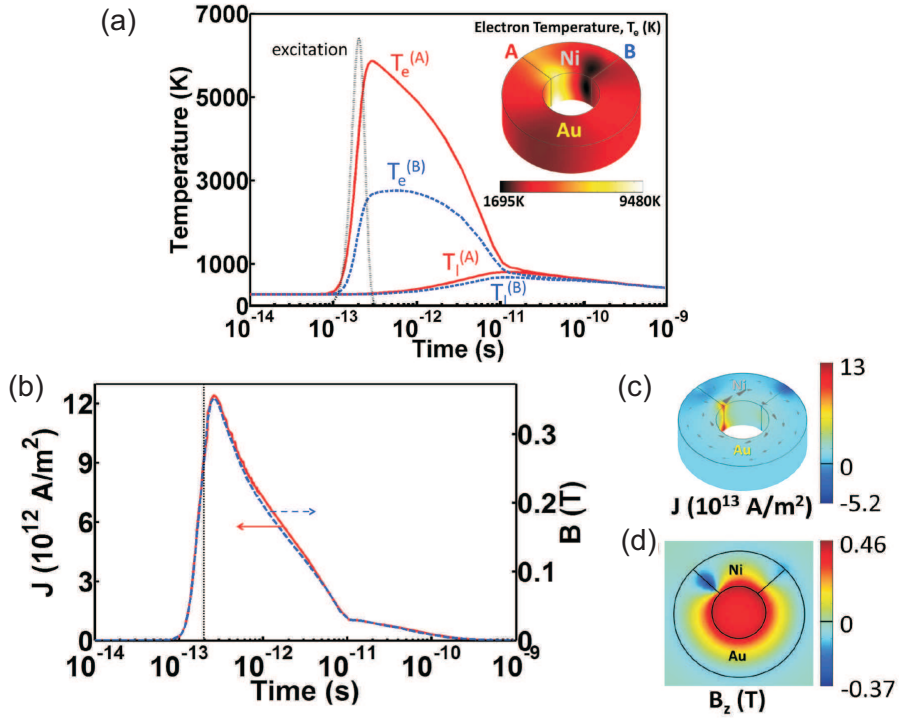


**Figure 5.4:** *(a) Temporal temperature profiles upon irradiation by a light pulse. Electron $T_e$ and lattice $T_l$ temperatures at the hot-A (red) and cold-B (blue) junctions of the ring. The pulse fluence is $11.3 J/m^2$ and evolves as shown by the dotted curve. Inset: the electronic temperature distribution of the ring at the maximum point of the red curve. (b) The time evolution of the azimuthal component of the current through junction A (dashed) and the magnetic induction averaged over the ring hole (solid). The dotted vertical line indicates the maximum of the light pulse intensity. (c) and (d) Snapshots of the instantaneous current on the ring surface (c) and the axial component of the magnetic induction (d), both at the time of the maximum of the curves plotted in (b).*

azimuthal component, except near the hot junction, where parasitic short-length loops are produced.

These strong currents give rise to a large magnetic induction ($> 0.35$T peak-value) of similar temporal profile. The magnetic induction is localised inside the ring cavity, as shown in Fig. 5.4(d). A small anomaly is observed near the hot junction as a result of the parasitic loops. The magnetic pulse has a duration $\Delta t_{\mathrm{mag}} \approx 1.8$ps FWHM, mainly controlled by the electron diffusion time and thermalisation into the lattice.

The radiation produced by the transient thermoelectric current in one nanoring is expected to be roughly peaked at a frequency corresponding to the inverse of the temporal width of the heating peak. The calculated radiation energy per unit of emission frequency, which is represented in Fig. 5.5, fully corroborates this intuition. Thus,

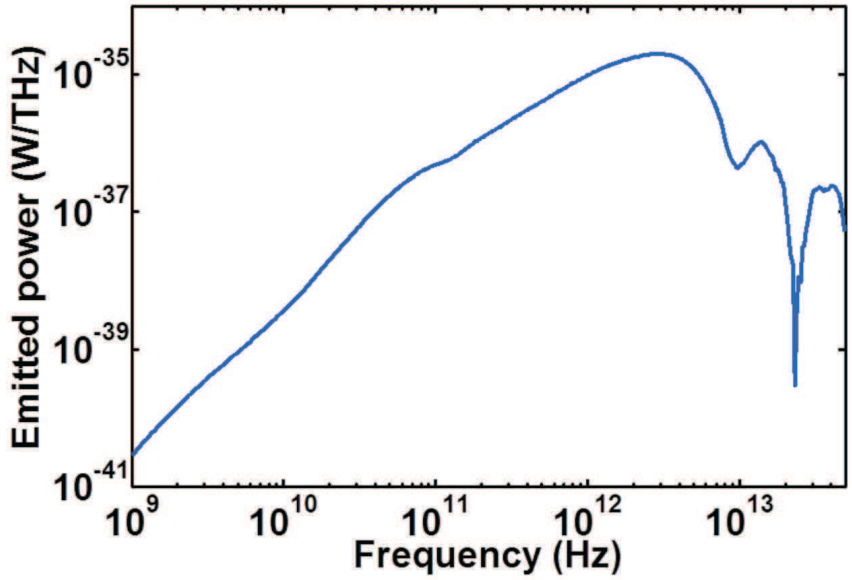


**Figure 5.5:** *Radiation emission spectrum produced by the thermoelectric current. The energy radiated by the thermoelectric current per unit of emission frequency is illustrated. The radiation is roughly peaked at the frequency* ($\sim 1\,THz$) *corresponding to the inverse of the temporal width of the heating peak* ($\sim 10^{-12}s$).

thermoelectric metamaterials constitute an innovative way of generating THz radiation, although the efficiency of the emission is small compared to the energy dissipated via relaxation to the lattice.

As a practical consideration, the main limitation on the values of the achievable magnetic field comes from the breakdown current in the rings ($\sim 10^{12} - 10^{13}\mathrm{A/m}^2$ for gold [186, 187]), as well as from possible melting of the metals [188]. However, the short duration of the optical irradiation, the moderate lattice temperatures involved, and the embedding of the ring in a rigid glass matrix should push the thresholds for melting and electrical breakdown well beyond the currets and temperatures considered here. In addition, it needs to be stated that here our aim is to show a generic way of creating intense transient magnetic fields with optical excitations, thus, optimization of the structure in the future could help to overcome limitations of this kind.

## 5.7 Thermal & Optical Parameters

In this section we provide the physical parameters describing the thermal diffusion and the thermoelectric properties of Au and Ni.

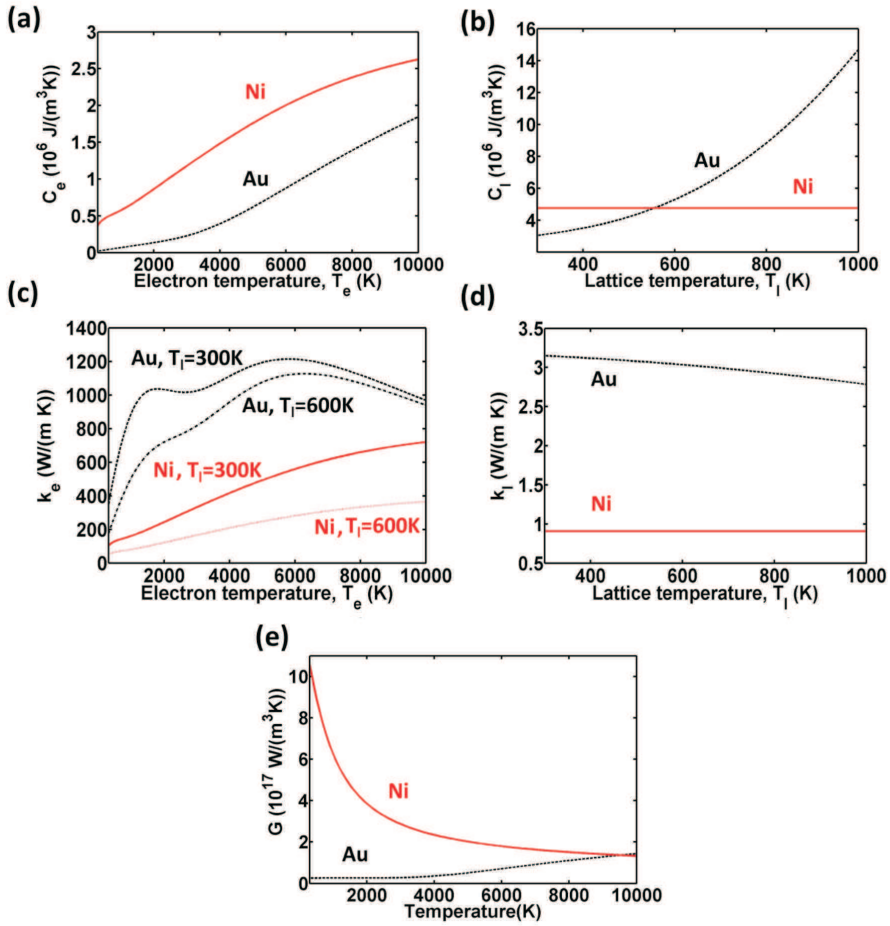


**Figure 5.6:** *Thermal parameters used in the description of heat diffusion for Ni and Au. (a) and (b) Electronic [178] and lattice [179, 180] heat capacities, $C_e$ and $C_l$, respectively. (c) and (d) Electronic [181–183] and lattice [179, 180] thermal conductivities, $k_e$ and $k_l$, respectively. (e) Electron-lattice coupling coefficient G [178].*

The parameters describing heat diffusion in both the electronic and lattice subsystems of Ni and Au are plotted in Fig. 5.6, along with the coefficient for electron-lattice thermalisation. These parameters depend on the electron temperature. Additionally, the electron thermal conductance depends also on the lattice temperature.

The temperature-dependent electron heat capacities are taken from [178], whereas the lattice heat capacity for Au is taken from [179]. However, there is little information available on the temperature dependence of the lattice heat capacity for Ni. However, since the lattice temperature is only slightly affecting our final results and the range of lattice temperatures is limited to $\approx 300-600$K, we have approximated it by a constant value measured at room temperature [180].

We approximate the electron thermal conductivity from the Drude model [181] as:

$$k_e(T_e, T_l) = \frac{1}{3} C_e u_F^2 \tau(Te, T_l), \tag{5.9}$$

where $u_F$ is the Fermi velocity ($1.40 \times 10^6$m/s in Au [181] and $0.28 \times 10^6$m/s in Ni [189]) and $\tau(T_e, T_l)$ is the inverse of the electron scattering rate. The latter is approximated as [182]:

$$\tau(T_e, T_l) = \frac{1}{A_e T_e^2 + B_l T_l}, \tag{5.10}$$

where $A_e = 1.2 \times 10^7$ and $B_l = 1.23 \times 10^{11}$ for Au [182] and $A_e = 1.4 \times 10^6$ and $B_l = 1.624 \times 10^{13}$ for Ni [183], all in SI units with the temperatures measured in Kelvin. The lattice thermal conductivity is taken from [179] for Au, and considered constant for Ni, as stated earlier. In addition, the electron-lattice thermal coupling coefficient $G$ is taken from [178].

Finally, the Seebeck coefficient $S$ and the electrical conductivity $\sigma$ are calculated, following the derivation described in [184], from the electronic density of states, taken from [178] for Au and Ni, and weighted by the Fermi-Dirac distribution for each temperature $T_e$. Both $S$ and $\sigma$ exhibit a pronounced electron-temperature dependence, as shown in Fig. 5.7.

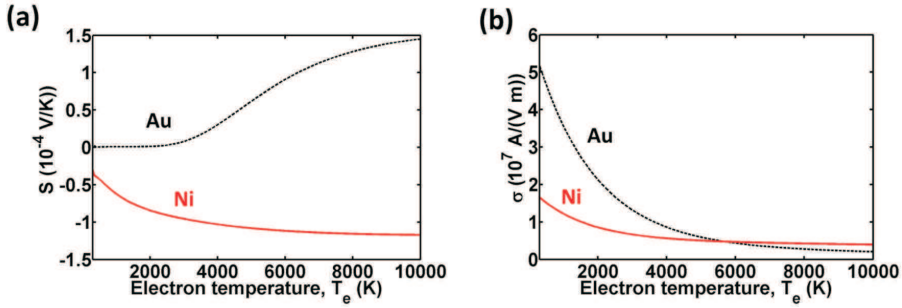


**Figure 5.7:** *Electrical and thermoelectrical properties of Au and Ni. Temperature dependence of (a) the Seebeck coefficient [184] and (b) the electric conductivity [178, 184].*

## 5.8 Epilogue

Our results indicate that we can take advantage of the strong thermoelectric currents that are induced at nanostructures by NIR light pulses, in order to generate transient

THz electromagnetic fields with very intense magnetic field component. This can form the basis of a new source of optically pumped THz radiation, whereby illuminated rings act as localised magnetic dipoles. These results can facilitate the study of ultrafast nanoscale magnetic phenomena and they hold great potential for applications in materials characterization, in the generation of terahertz radiation, and in future magnetic recording. Especially for the magnetic recording application, nanoscale recording is allowed (with spot sizes smaller than the 100nm diameter of the ring cavity) in the case that this method is used to magnetise suitable magnetic-grain sizes able to react to the short duration of the THz magnetic pulses generated [52].

# 6 Conclusions

## 6.1 Summary

The lack of natural materials able to interact efficiently with THz radiation poses challenges in the generation and control of THz fields. In addition, guiding of THz radiation with low-loss and low-dispersion waveguiding structures is another challenge. Thus, huge obstacles exist for both the scientific investigation of this spectral band and the commercialization of devices operating in it.

In this thesis, we addressed these challenges and presented novel ways for efficiently manipulating, guiding, and generating THz and sub-THz radiation based on interdisciplinary approaches. Novel in the sense that they haven't been considered before, and efficient since they can show the required functionality without suffering from high losses. The interdisciplinary approaches presented in this thesis exploit the exotic electrodynamics of metamaterials and the intriguing physics of superconductors coupled with plasmonic and thermoelectric phenomena in nanostructures. In the previous chapters, it was mainly shown that superconductors enabled low-loss manipulation and guiding of THz fields, while structures combining the plasmonic and the thermoelectric properties of materials allowed the generation of THz radiation. Here, we summarize the most important of the experimental and theoretical results reported in this thesis.

The first experimental study of free-space superconducting metamaterials has been presented. Through the realisation and demonstration of superconducting metamaterials made of low critical-temperature superconductor Nb and high critical-temperature superconductor YBCO, we managed to show that patterning superconductors on a mi-

croscale does not affect their low-resistance state much. Furthermore, we managed to conduct the first demonstration of Fano-type resonances in the sub-THz (millimetre-wave) frequency domain with superconducting metamaterial arrays of asymmetric split-rings (ASRs), which were also dynamically controlled through temperature.

The first experimental realisation of the extraordinary transmission effect in periodically perforated superconducting films was reported. It was identified that in the millimetre-wave part of the spectrum strong extraordinary transmission exists in the ideal superconducting state of the films. It was also shown that in hole arrays the extraordinary transmission effect is created by the collective interaction of radiation propagating through the holes, with this collective interaction affected by the temperature-controlled conductive properties of the material. In addition, as part of this thesis attempts have been reported to develop and experimentally demonstrate a quantum superconducting metamaterial.

From a theoretical point of view, we showed that a classical simple model can be used to describe the high-temperature yttrium-barium-copper-oxide (YBCO) superconducting metamaterial structures. This model found use in simulations involving superconducting structures and in the interpretation of the response of these structures. This theoretical model was based on the Drude model for metals, the two-fluid model for superconductors, derived experimental results of the electrons scattering rate in superconducting films under irradiation with high frequency electromagnetic waves, and the surface impedance concept. While tested only for YBCO structures we postulate that the extension to different kinds of superconducting metamaterial structures is straight-forward.

As part of the work reported in this thesis we have identified superconductors as intrinsically plasmonic media. More importantly, it was theoretically estimated that in certain geometries virtually dispersionless plasmonic modes could be supported at the THz frequencies (up to the gap frequency of the relevant superconductor) and below, exhibiting extreme localisation and very low propagation losses. These structures could be useful in imaging and high-rate data-carrying applications.

Finally, the concept of thermoelectric metamaterials has been introduced in this thesis. It was theoretically predicted that optically induced generation of Tesla magnetic pulses with ultrafast temporal dynamics and nanoscale localisation is possible,

through the exploitation of metamaterial plasmonic resonators that also have specific thermoelectric properties. More precisely, it was estimated that a bimetallic ring can act as a Tesla-scale magnetic field generator, through an interplay between the appearance of the Peltier-Seebeck effect in the structure and the absorption of energy from an optical excitation at the lowest-order dipole plasmon resonance of the ring. The ability to create strong magnetic fields with ultrafast temporal dynamics and nanoscale localisation is of importance for applications such as data magnetic recording and time-domain magnetic spectroscopy.

## 6.2 Outlook

This thesis did mainly report on "proof of concept" demonstrations of effects and theoretical investigations of ideas that could be exploited for efficient manipulation, guiding, and generation of THz and sub-THz radiation. Therefore, as far as the "proof of concept" demonstrations are concerned, further work is necessary to optimise the structures and assess the importance of the reported effects for practical applications. Regarding the theoretical investigations of possible effects, the immediate next step would be their demonstration through experiments. More precisely, suggestions for future work on each of the discussed topics are presented:

**Manipulating THz Radiation (Superconducting Metamaterials)** Since most of the experiments reported in this thesis were conducted in sub-THz frequencies, the realisation of superconducting metamaterials operating at higher THz frequencies is necessary in the future. In addition, further studies should be conducted on the active control of superconducting metamaterial structures. In particular, the effects of intense light incident on the metamaterial surface, and strong magnetic fields or currents passing through the structure could be examined[1]. Furthermore, the macroscopic quantum coherent state of superconductors could be exploited for realising quantum metamaterials. An experimental confirmation of the theoretically predicted behaviour of metamaterial arrays of rings with Josephson Junctions would be a step in this direction.

[1]In fact, the influence of current propagating through a metamaterial array and its influence on the electromagnetic response was shown by Savinov et al. in [113].

**Guiding THz Radiation (Superconducting Plasmonics)** In this thesis, the importance of the plasmonic nature of superconductors at frequencies up to the THz domain has been highlighted. Based on this, possible waveguiding configurations have been proposed, having many advantages in guiding THz and sub-THz signals, including the ability to achieve nanoscale localisation, low losses, and negligible dispersion. A necessary next step would be the realisation and characterisation of these waveguiding structures. Furthermore, different kinds of waveguiding geometries as well as their dynamic control through stimuli that affect the superconducting state could be investigated. For certain waveguide realisations, where dimensions of only a few nanometres exist, quantum effects should appear (as predicted in the Josephson Junction theory). Waveguiding structures exploiting these quantum effects could be considered, which could enable new ways to interact with the propagating plasmonic modes.

**Generating THz Radiation (Thermoelectric Metamaterials)** As a part of this thesis, significant effort has been placed in developing the concept of thermoelectric metamaterials and identifying structures able to generate strong THz fields. Since the concept of thermoelectric metamaterials exploits the interplay of many effects described by highly nonlinear models, such as plasmonic resonances of nanostructures, heating dynamics, and magnetic fields generation, a huge effort has been placed in developing an extremely complex multiphysics model that was required for predicting their response. An immediate next step is the experimental confirmation of the theoretical results, necessary also in order to reveal any limitations of these structures. Furthermore, new optimised meta-atom designs as well as different combinations of metals could be considered, in order to achieve an optimum combination of plasmonic and thermoelectric properties in the structure. That could lead to enhanced performance and ultimately to the generation of THz radiation with higher efficiency than the suggested approach.

# A

# Brief Introduction to Superconductivity

Superconductors behave similar to normal materials down to a critical temperature $T_c$, below which they change to the superconducting state [142]. The superconducting state is characterised by three unique properties, not shared by normal metals: zero DC resistance, fully diamagnetic Meissner effect, and macroscopic quantum coherence. The last property gives actually birth to the other two and results in effects such as the magnetic flux quantization and the Josephson effect.

Although this thesis does not contribute in the advancement of superconductors and their physics, a brief overview of the physics involved in the field of superconductivity can help us interpret our results and gain understanding of why and how metamaterials can be designed by exploiting such materials. In this appendix, we provide a short history of the field of superconductivity over the last 100 years and we explain the physics behind superconductors' behaviour.

## A.1 Superconductivity: The Story

Superconductivity arguably ranks among the ultimate in beauty, elegance, and profundity, both experimentally and theoretically, of all the advances in condensed-matter physics during the 20th century, even if it has to date yielded only a few applications that have permeated society. When a team led by Heike Kamerlingh Onnes stumbled across superconductivity, 100 years ago, the scientific community was caught by complete surprise. Given that electrons usually conduct imperfectly, by continuously colliding with the atomic lattice through which they pass, the fact that conduction can also be perfect under the right conditions is surely fascinating.

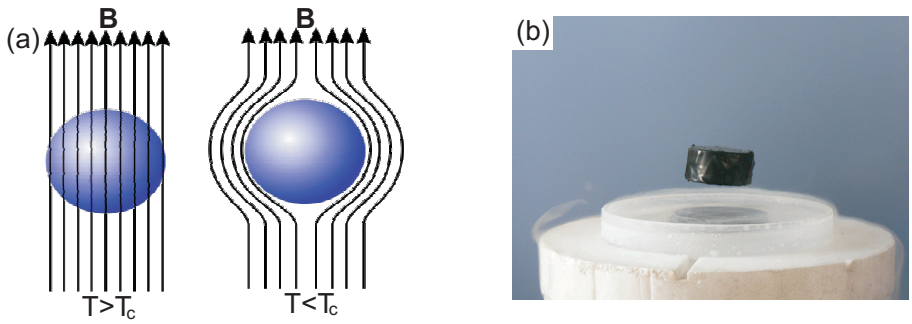


**Figure A.1:** *(a) Any kind of magnetic field, stationary or time-varying, is totally expelled from the superconductor once it has been cooled below the transition temperature $T_c$ (Meissner effect). (b) A manifestation of the Meissner effect: the elevation of a magnet above a superconductor.*

The discovery of superconductivity was a race between the Dutch physicist Onnes and the British physicist James Dewar as they competed to reach a temperature of absolute zero using ever more complex devices to liquefy gases. Onnes won, after he successfully liquified helium by cooling it to 4.2K, for which he also got the Nobel prize in 1913. Having achieved these low temperatures, his team was interested in how the properties of materials, particularly their electrical conductance, change under cryogenic conditions. Up to that point, it was known that when a current is carried by an ordinary conductor, such as a normal metal or a semiconductor, resistance is inevitably present because the current carriers are scattered with a change in their momentum. Thus, their free acceleration induced in the direction of an applied electric field is hindered due to scattering of the electrons from impurity atoms, lattice defects or thermal vibrations (phonons) [190]. To test if this was still the case in very low temperatures, Gilles Holst suggested creating a sample by repeatedly distilling liquid mercury to remove the impurities that were found to dominate scattering below 10K. It was in April 1911 that Holst and his lab technician Gerrit Flim discovered that the resistance of liquid mercury, when cooled to 4.2K reached a value so small that was impossible to measure. This phenomenon - the complete absence of electrical resistance- is the hallmark of superconductivity.

After the 1911 discovery, research into superconductivity languished for several decades, mainly since having the necessary equipment was difficult and expensive. In addition, there was another reason: the zero DC-resistance state disappeared when

a sample was exposed to even quite modest magnetic fields. By the time other labs in Europe and North America developed their own liquid-helium cryogenic facilities, interest and progress in superconductivity resumed. In 1933, Walther Meissner and Robert Ochsenfeld observed that any magnetic field (stationary and time-varying) near a superconducting material was totally expelled from the sample once it had been cooled below the transition temperature $T_c$. The magnetic field lines, which under normal circumstances would pass straight through the material, had to flow around the superconductor, as shown in Fig. A.1(a). This effect is now known as "magnetic flux expulsion" or "Meissner effect" [191] and can even lead to the elevation of magnets above superconductors (see Fig. A.1(b)).

Progress in forming the fundamental theory behind superconductivity advanced more slowly. In 1935, Fritz and Heinz London proposed a phenomenological adjustment to Maxwell's constituent equations to accommodate the notion of "penetration depth" of an externally applied magnetic field beyond the surface of a superconductor [192]. Their main contribution was to realise that the "Meissner effect" was more important for the formation of an explanation of superconductivity compared to the lack of resistance in DC electric fields. They were also the first to grasp that superconductivity is an example of quantum coherence not on a scale of a single atom -a nanometre across- but on the scale of a sample size -several millimetres or centimetres across. Fritz London used for the first time the phrase "macroscopic quantum phenomenon" to categorize superconductivity. A macroscopic sample of superconductor behaves like a giant atom.

A theory that can explain superconductivity was finally formed by John Bardeen, Leon Cooper, and Robert Schrieffer, leading to what is now called the BCS theory [168], for which the three of them shared the 1972 Nobel Prize for Physics. Cooper had determined that a gas of electrons is unstable in the presence of any infinitesimal attractive interaction, leading to pairs of electrons binding together [193]. Bardeen and his student Schrieffer then realised that the resulting quantum state had to be macroscopic and statistical in nature. Experimental evidence suggested that somehow lattice vibrations (phonons) are involved in superconductivity. BCS theory proved that these vibrations, which under regular conditions contribute to the metal's intrinsic resistance, could yield the attractive interaction that allows a material to conduct

without resistance when the conditions are right. Although the BCS theory can explain the observed effects, it is very poor at pointing out what materials to use or develop to create new superconductors.

Meanwhile, new developments happened in the field of superconductivity. In 1962, Brian Josephson at Cambridge University proved that a current can electrically tunnel across two superconductors separated by a thin insulating or normal metal barrier [194]. This effect was observed one year later by John Rowell and Philip Anderson of Bell Laboratories, and resulted in the development of the superconducting quantum interference device (SQUID), which can measure minute levels of magnetic fields [195]. More than two decades later, Georg Bednorz and Alex Muller observed that in layered copper-oxide perovskites[1] there was zero resistance at temperatures above 30K. These superconductors were called "high temperature", not because their transition temperatures are really high, but since they exceeded the maximum transition temperatures implied by the BCS model [190]. The discovery of "high temperature superconductors" not only offered Georg Bednorz and Alex Muller the Nobel Prize for Physics in 1987, but also triggered a boom in research into the field once again. One year later, Paul Chu and his collaborators at the university of Houston in Alabama discovered that an yttrium-barium-copper-oxide compound -$YBa_2Cu_3O_{6.97}$, most commonly known as YBCO- could superconduct at a temperature of 93K [196]. As this is 16K above the boiling point of liquid nitrogen, the discovery of these materials allowed researchers to explore for the first time applications of superconductivity using a very common and cheap cryogen (i.e., nitrogen). Since then superconductivity has been observed in different types of materials, such as salt, the cheap and simple chemical magnesium diboride ($MgB_2$), and iron compounds. The record in transition temperatures is currently at 138K in fluorinated $HgBa_2Ca_2Cu_3O_{8+\delta}$ at ambient pressure (or 166K under a pressure of 23GPa).

Alongside these advances in the science of superconductivity, there have been numerous attempts to apply the phenomenon to advance old and create new technologies ranging from the very small scales (applications in ultrafast computers) to the very large ones (for generating and transporting electricity). Although the inexistence of

[1]Perovskite is a calcium titanium oxide mineral species composed of calcium titanate with the chemical formula $CaTiO_3$. However, it lends its name to the class of compounds which have the same type of crystal structure as $CaTiO_3$, which is known as the perovskite structure.

room temperature superconductors has prevented the large deployment of superconducting devices in the generation and the transportation of electric energy (primarily due to the cost of the necessary coolant) there have been successful demonstrations of superconducting cables, generators, and transformers. The small weight compared to other similar devices that use iron is another advantage. Thus, applications have emerged in situations that weight is an issue or accuracy is needed. A second major area of applications has been in the generation of high magnetic fields. Such strong magnetic fields are necessary for magnetic resonance imaging (MRI) and particle colliders in high energy physics laboratories. Finally, superconductors have also found extensive use in the realisation of high quality-factor (Q-factor) filters in microwave circuits and in applications that the need for low losses exceeds the extra cost.

## A.2 Superconductivity: The Theory

We start this section by describing qualitatively the BCS theory. More emphasis is then given to London's equations, which provide a phenomenological description of the superconductors response to an applied electromagnetic field. This knowledge is of importance for the design and the analysis of the response of the structures presented in this thesis.

### A.2.1 The BCS Theory

The BCS theory starts from the assumption that there is some attraction between electrons that allows them to overcome the Coulomb repulsion. In low-temperature superconductors this attraction is caused by the coupling of electrons with the crystal lattice. A free electron moving through the lattice will attract nearby positive charges. The deformation of the lattice causes another electron, with opposite spin, to move into the region of higher positive charge density. The two electrons then become correlated, appearing as an electron pair which is coupled over a range of hundreds of nanometres, three orders of magnitude larger than the lattice spacing, and is called a Cooper pair. Since many such pairs are formed, they overlap very strongly, and create a highly collective condensate. In this condensed state, the breaking of one pair will change the energy of the entire condensate. Thus, the energy required to break any single

pair is related to the energy required to break all the pairs, and is of the order of milli-electron volts. Actually, it is the pairing that increases this energy barrier, so that the scattering with oscillating atoms of the lattice is not enough to affect the condensate as a whole or any individual pair within the condensate. It needs to be noted that anyhow this scattering process in these low temperatures is not so strong, as a consequence of the small kinetic energies of the atoms. Thus, the electrons stay as pairs, which is qualitatively equivalent to the electron flow not experiencing any resistance. There would be no superconductivity without this condensate; there would be no superconductivity without this macroscopic coherent quantum state.

Staying a bit more in the explanation of zero resistance, the effect could be described as follows. A passing electron attracts the lattice, causing a slight ripple in its path. Another electron passing in the opposite direction is attracted to this displacement. This attraction constitutes the coupling between the electrons. Since the first electron's momentum change in its scattering with the lattice is canceled by the opposite momentum change of the second electron, the total momentum of the Cooper pair stays the same in the direction of the scattering. In a macroscopic level, this is equivalent to no scattering taking place, which leads to a zero DC-resistance [142].

Among the general conclusions of the BCS theory is the very simple expression:

$$T_c \sim \Theta / e^{1/\lambda}, \tag{A.1}$$

that relates the transition temperature $T_c$ below which a material superconducts, with the characteristic temperature of the boson field $\Theta$ (that is the Debye temperature in the case of phonons), and the coupling constant of that field to electrons and/or holes in solids $\lambda$. A material with a large value of $\lambda$ is generally a good candidate for a superconductor even if it is a poor metal under normal conditions. This explains why sodium, gold, silver, and copper, despite being good metals, are not superconductors, yet lead is [190]. The BCS theory also explains the Meissner effect, the temperature-dependence of the energy needed to break the superconducting state, and the Josephson effect.

### A.2.2 The London Equations

Leaving the microscopic description of superconductors, we now focus on their macroscopic behaviour and especially on the response of superconductors to an applied electromagnetic field. In this description, the work of the London brothers was crucial. Meissner and Ochsenfeld had showed that a superconductor below $T_c$ when exposed to an applied magnetic field expels that magnetic field from its interior. For this effect to take place, surface superconducting electrical currents, denoted as supercurrents, flow around the superconductor in such a way that the interior is shielded from the applied magnetic field. These circulating supercurrents oppose the applied magnetic field, so that deep within the superconductor the magnetic field is close to zero -an effect known as perfect diamagnetism. This effect is different from the screening of ac electromagnetic fields by conductors, since, in the latter case, only alternating fields are screened, while a static magnetic field could penetrate thoroughly. Actually, in the case of ideal conductors, the field would have been trapped inside them. Therefore, ideal conduction, which had been thought of as the superconductor's defining quality, lost its central role in the explanation of their behaviour. It was the London brothers that realised that it was more of a by-product. A new relation between the electric current and the magnetic field was needed for superconductors rather than a relationship between the electric current and the electric field (new Ohm's law). In the rest of this section, the London equations will be presented. To facilitate our discussion we start by examining the case of a normal conductor [145].

We assume an electron with charge $-e$ having mass $m$ and moving with velocity $\mathbf{v}$ in the presence of an applied electric field $\mathbf{E}$. In this case, the equation of its motion is:

$$m\frac{d\mathbf{v}}{dt} = -e\mathbf{E} - \frac{m}{\tau_{tr}}\mathbf{v}, \tag{A.2}$$

where the first term on the right-hand side of this equation is derived from Ohm's Law, while the second term is related to the scattering of electrons and is inversely proportional to the transport scattering time $\tau_{tr}$. This time is defined as the average time an electron is able to travel freely under the acceleration of the electric field $\mathbf{E}$

without the occurrence of scattering. Eq. (A.2) can be written as:

$$m\frac{d\mathbf{v}}{dt} + \frac{m}{\tau_{tr}}\mathbf{v} = -e\mathbf{E}. \tag{A.3}$$

We assume that the electric field is sinusoidal. Therefore, the response of a single electron to the applied field is sinusoidal as well. Thus, we write: $\mathbf{E} = \Re[\dot{\mathbf{E}}e^{j\omega t}]$ and $\mathbf{v} = \Re[\dot{\mathbf{v}}e^{j\omega t}]$. Then, we have:

$$j\omega m\dot{\mathbf{v}} + \frac{m}{\tau_{tr}}\dot{\mathbf{v}} = -e\dot{\mathbf{E}}, \tag{A.4}$$

and

$$\dot{\mathbf{v}} = \frac{-e\tau_{tr}}{m}\frac{1}{1+j\omega\tau_{tr}}\dot{\mathbf{E}}. \tag{A.5}$$

If we now consider a density of $n$ conduction electrons per unit volume, their total response, which corresponds to the current density, is:

$$\dot{\mathbf{J}} = -ne\dot{\mathbf{v}} = \left(\frac{ne^2\tau_{tr}}{m}\right)\frac{1}{1+j\omega\tau_{tr}}\dot{\mathbf{E}}. \tag{A.6}$$

In this case we define:

$$\sigma(\omega) = \sigma_0\frac{1}{1+j\omega\tau_{tr}}, \tag{A.7}$$

with $\sigma_0 = \frac{ne^2\tau_{tr}}{m}$ called the DC conductivity. Eq. (A.7) can be written in the form:

$$\sigma(\omega) = \Re[\sigma(\omega)] + j\Im[\sigma(\omega)] = \frac{\sigma_0}{1+(\omega\tau_{tr})^2} - j\frac{\sigma_0\omega\tau_{tr}}{1+(\omega\tau_{tr})^2}. \tag{A.8}$$

The real and imaginary parts of conductivity can be connected with the imaginary and the real parts of permittivity, respectively, through the relationship:

$$\varepsilon(\omega) = 1 - \frac{j\sigma(\omega)}{\varepsilon_0\omega} = 1 - \frac{\sigma_0\tau_{tr}}{\varepsilon_0(1+(\omega\tau_{tr})^2)} - j\frac{\sigma_0}{\varepsilon_0\omega(1+(\omega\tau_{tr})^2)}. \tag{A.9}$$

From the perspective of permittivity, the real part is associated with the "dielectric" response of the material and can be seen as an inductive term, while the imaginary part is related to the Ohmic losses.

When $\omega\tau_{tr} >> 1$, the material has no losses but only a purely inductive behaviour, which implies that it is an ideal conductor. On the other hand, assuming $\sigma(\omega) =$

$\sigma_0 \to \infty$ (infinite conductivity) means that the material is purely resistive (perfect conductor).

The approach of the London brothers was to assume that there is no scattering between the carriers in the superconductor. If we consider a density of $n_s$ superconducting electrons, then their equation of motion is:

$$n_s m \frac{\mathrm{d}\mathbf{v}_s}{\mathrm{d}t} = n_s q_s \mathbf{E}, \tag{A.10}$$

where $m$ is the superconducting carrier mass, $q_s$ their charge, and $\mathbf{v}_s$ their average velocity. Therefore the supercurrent density, defined as $\mathbf{J}_s = n_s q_s \mathbf{v}_s$, relates to the applied electric field $\mathbf{E}$ through the formula:

$$\mathbf{E} = \frac{\mathrm{d}}{\mathrm{d}t}(\lambda \mathbf{J}_s), \tag{A.11}$$

with $\lambda = \frac{m_s}{n_s q_s^2}$. The superconducting carriers are actually electron Cooper pairs, so $m_s = 2m$, $q_s = -2e$, and $n_s = n/2$, leading to $\lambda = \frac{m}{ne^2}$.

Eq. (A.11) is the First London equation and expresses the direct relation between the superconducting current variations and the electric field. It implies that a stationary supercurrent flows without voltage and, thus, without any resistance. The most serious limitation of the London theory is connected to the assumption that $n_s$ and $n_n$ are uniform in space. This is equivalent to examining only the stationary state. The Ginzburg-Landau theory overcomes this limitation [197].

If we now consider the curl of the First London equation we get:

$$\nabla \times \mathbf{J}_s = \frac{e^2 n_s}{m} \nabla \times \mathbf{E} = -\frac{e^2 n_s}{m} \frac{\partial \mathbf{B}}{\partial t}. \tag{A.12}$$

Eq. (A.12) integrated in time gives:

$$\nabla \times \mathbf{J}_s = -\frac{e^2 n_s}{m} \mathbf{B} + \mathbf{C}(\mathbf{r}), \tag{A.13}$$

where $\mathbf{C}(\mathbf{r})$ represents a constant of integration at each point $\mathbf{r}$ inside the superconductor and can be determined from the initial conditions. In the case that we have as initial condition a superconducting body in zero applied magnetic field, $\mathbf{J}_s \equiv \mathbf{0}$ and

$\mathbf{B} \equiv \mathbf{0}$ and, therefore, $\mathbf{C}(\mathbf{r}) = \mathbf{0}$.

However, to describe the Meissner effect we have to consider the case of a body becoming superconducting (by cooling) in a non-zero applied magnetic field. Unfortunately, this case cannot be treated within the London theory, since the superfluid density $n_s$ has been assumed to be constant in time. To account for the flux expulsion, the London brothers postulated that $\mathbf{C} \equiv \mathbf{0}$, regardless of the history of the system, which led to:

$$\nabla \times \mathbf{J}_s = -\frac{e^2 n_s}{m}\mathbf{B}, \tag{A.14}$$

which is known as the Second London equation.

**Superconductor's Response on an Applied DC Magnetic Field**

We apply the London theory to derive the repsonse of a superconductor in the case of an applied DC magnetic field. We start by considering Ampere's Law:

$$\nabla \times \mathbf{B} = (\mathbf{J} + \mathbf{J}_s)\,\mu_0. \tag{A.15}$$

There are no displacement currents at DC, therefore we get:

$$\nabla \times \nabla \times \mathbf{B} = -\frac{\mu_0 e^2 n_s}{m}\mathbf{B} + \mu_0 \sigma_n \nabla \times \mathbf{E} = -\frac{\mu_0 e^2 n_s}{m}\mathbf{B} - \mu_0 \sigma_n \frac{\partial \mathbf{B}}{\partial t}. \tag{A.16}$$

Since at DC there is no time-dependence, we drop the last term on the right-hand side of Eq. (A.16). So, Eq. (A.16) is written as:

$$-\nabla(\nabla \cdot \mathbf{B}) + \nabla^2 \mathbf{B} = \frac{\mu_0 e^2 n_s}{m}\mathbf{B}. \tag{A.17}$$

At this point, we define the London penetration depth as:

$$\lambda_L = \sqrt{\frac{m}{n_s e^2 \mu_0}}. \tag{A.18}$$

This allows us to write Eq. (A.17) in the simple form:

$$\nabla^2 \mathbf{B} = \frac{1}{\lambda_L^2}\mathbf{B}, \tag{A.19}$$

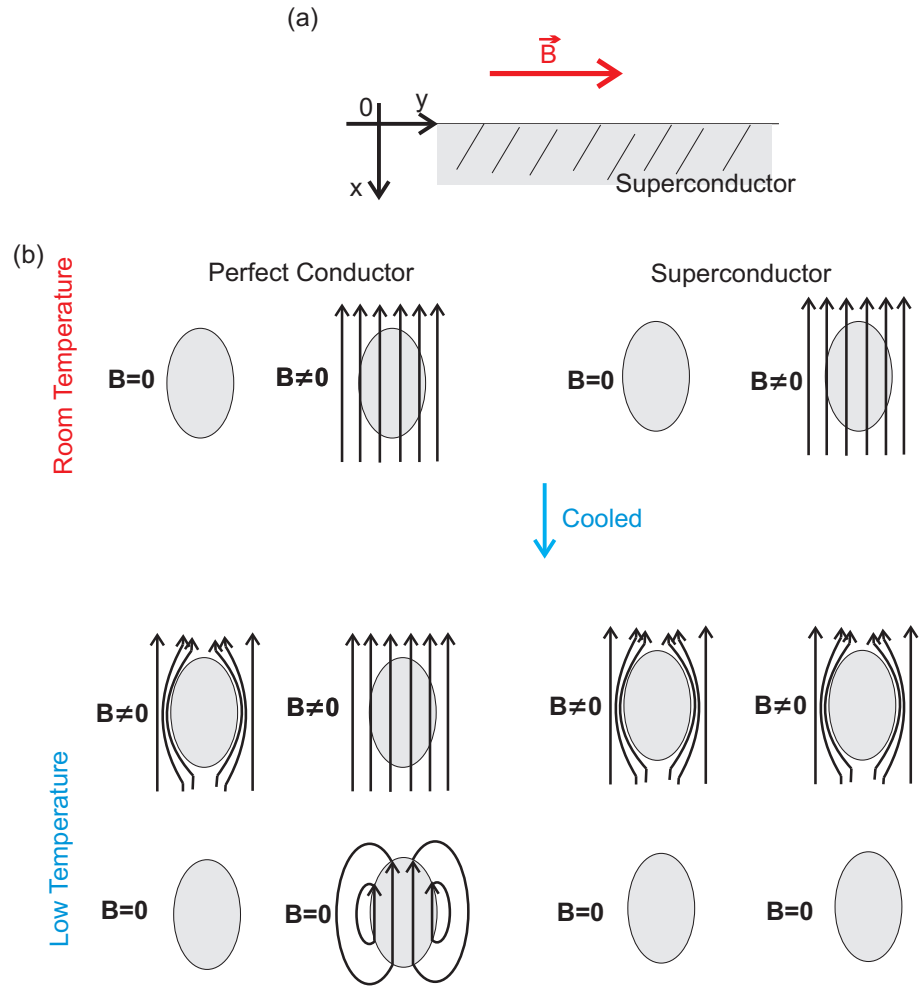


**Figure A.2:** *(a) A semi-infinite superconductor is filling the half-space $x > 0$, while a stationary magnetic field is applied in the y-direction parallel to the surface of the superconductor. Deep inside the superconductor no magnetic flux manages to penetrate due to the screening effect of the excited supercurrents. (b) The difference between a superconductor and a perfect conductor. Magnetic flux is expelled in all cases below $T_c$ for the superconductor case. In the case of a perfect conductor the field not only can penetrate its interior but also the flux is trapped in there when we remove the excitation field.*

since $\nabla \cdot \mathbf{B}$=0. The implications of this formula are shown, e.g., if we consider a semi-infinite superconductor filling the half space $x > 0$ and an applied magnetic field $\mathbf{B}_{\text{apl}}$=$\mu_0\mathbf{H}_{\text{apl}} = B_{\text{apl}}\hat{\mathbf{y}}$, parallel to the surface of the superconductor, as illustrated in Fig. A.2(a). We can then derive the solution of Eq. (A.19):

$$\mathbf{B}(x) = B_{\text{apl}} e^{-x/\lambda_L} \hat{\mathbf{y}}, \quad \text{for } x \geq 0. \tag{A.20}$$

The magnetic field, thus, decreases exponentially when the distance from the surface of

the superconductor is increased. So, deep inside the superconductor we have $\mathbf{B} \to \mathbf{0}$. Using the second London equation in combination with the continuity equation we get:

$$\nabla \cdot \mathbf{J}_s = 0, \tag{A.21}$$

which leads to:

$$\mathbf{J}_s(x) = -\frac{1}{\lambda_L} B_{\text{apl}} e^{-x/\lambda_L} \hat{\mathbf{z}}, \tag{A.22}$$

for $x \geq 0$. Thus, the supercurrent flows in a direction parallel to the surface of the superconductor and perpendicular to $\mathbf{B}$, decreasing into the bulk superconducting region with a penetration depth equal to $\lambda_L$. In this sense, $\mathbf{J}_s$ could be perceived as the screening current required to keep the magnetic field out of the bulk of the superconductor.

The last remarks and the extension of the magnetic flux expulsion in the DC regime are necessary to distinct a superconductor from a perfect conductor. In the case of a perfect conductor, magnetic fields of alternating frequencies are screened from the bulk of the material, an effect known as skin effect [55]. However, in superconductors this also happens for stationary fields. Furthermore, there is one more difference between the two, explained by the theory presented. When we apply a stationary magnetic field to a perfect conductor, the field lines not only pass through it, but also when we remove this field, the original magnetic flux distribution is conserved in the interior of the conductor. Of course, in the superconductor there is no magnetic field inside the medium in any case. This is better illustrated in Fig. A.2(b), which schematically summarizes the differences between perfect electric conductors and superconductors.

### A.2.3 The Two-Fluid Model

Moving a step forward, we introduce the two-fluid model proposed by Gorter and Casimir [198]. This model suggests that the electrodynamic response of a superconductor at nonzero temperature is dominated by the co-existence of two noninteracting currents; the current of Cooper pairs of superconducting electrons, known as supercurrent, and the current of normal electrons encountering scattering processes. We use the symbols $J_s$ for the supercurrent density, as it was derived in the London theory, and $J_n$ for the normal current of electrons. Therefore, we have:

$$\frac{\partial \mathbf{J}_s}{\partial t} = \frac{1}{\lambda}\mathbf{E}, \tag{A.23}$$

and

$$\mathbf{J}_n = \sigma \mathbf{E}, \tag{A.24}$$

with $\lambda$ and $\sigma$ as defined earlier. The contribution of this model is that it allows the superconducting electron (Cooper pairs) density $n_s$ and the normal electron density $n_n$ to be temperature dependent. According to the two-fluid model, all free electrons at zero temperature are in superconducting state, thus $n_n = 0$. On the contrary, no superconducting electrons exist at the critical temperature $T_c$ and above, thus $n_s = 0$. This corresponds to a lossy metallic behavior. The balance between the densities of the superconducting and normal electrons is often described by the empirical Gorter-Casimir relation:

$$n_s(T) = \frac{n}{2}\left[1 - \left(\frac{T}{T_c}\right)^4\right], \tag{A.25}$$

where $n$ is the temperature independent total density of free carriers[2], while:

$$n_n(T) = n - 2n_s(T). \tag{A.26}$$

The carriers' dependence on temperature also implies that the London penetration depth is temperature dependent. More precisely, the temperature dependence of the latter is given by the formula:

$$\lambda_L(T) = \lambda_L \frac{1}{\left(1 - \left(\frac{T}{T_c}\right)^4\right)^{1/2}}, \tag{A.27}$$

where $\lambda_L$ is the London penetration depth at zero temperature, defined by Eq. (A.18). Interestingly, although this model is phenomenological and there is no microscopic physical basis for its derivation [197], it macroscopically provides a fairly accurate prediction of the electromagnetic response of superconductors, without diving into the

[2]In this derivation we have assumed for Cooper pairs a density equal to half the normal electrons density at zero temperature and a charge equal to twice the charge of an electron. At the time this model was proposed it was assumed that superconducting carriers had charge equal to the charge of an electron and density at zero temperature equal to the density of normal electrons at transition temperature. Of course, the final result for the supercurrent is the same.

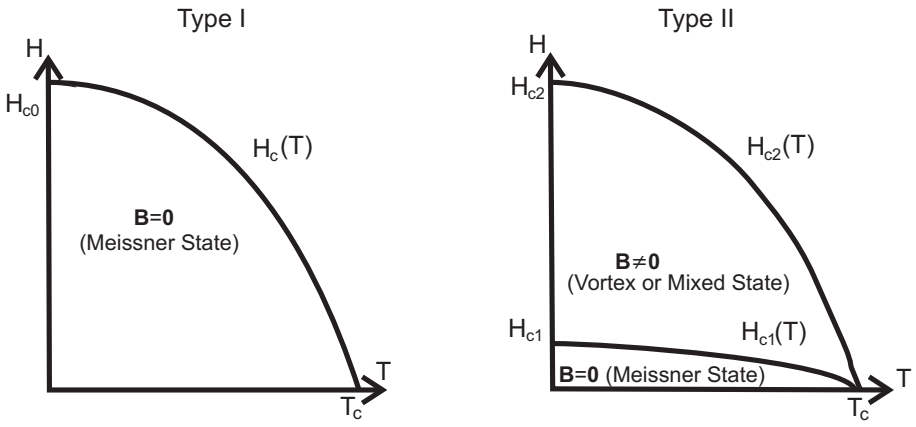


**Figure A.3:** *Type-I and Type-II superconductors. In the case of Type-II superconductors the application of a magnetic field of certain strength can lead to the formation of an intermediate state, known as the vortex state, in which both superconducting and normal regions exist in the superconductor's body.*

details and the complexity of quantum-theoretic interpretations.

## A.3 Superconductivity: Different Types

We have mentioned above that superconductivity breaks down when a magnetic field above a specific critical value is applied. Due to this behaviour, this magnetic field is named critical magnetic field $H_c$, and superconductors can be divided into two types according to how this breakdown occurs, as shown in Fig. A.3.

In type-I superconductors, superconductivity is abruptly destroyed via a first order phase transition[3] when the strength of the applied field rises above the critical value $H_c$. All type of elemental superconductors belong to this type except for niobium, vanadium, and technetium. Depending on the demagnetization factor, one may also obtain an intermediate state, in which a separation into macroscopic normal and superconducting domains is observed [197].

This behavior is different from type-II superconductors. Superconductors of this type exhibit two critical magnetic fields. Above a certain critical strength $H_{c1}$, the formation of magnetic vortices occurs. These magnetic vortices manifest themselves as lines of magnetic flux passing through the material, turning a superconducting region back into the normal state. This normal region is separated from the rest of the super-

[3]First order transitions involve a discontinuous change in density, which is the first derivative of free energy with respect to the chemical potential [190].

conductor by a circulating supercurrent around its edge. In analogy to fluid dynamics, the swirling supercurrent creates what is known as a vortex or an Abrikosov vortex. These vortices arrange themselves into a regular array known as a vortex lattice. The vortex density increases with increasing magnetic field strength. Finally, increasing the magnetic field until the critical value $H_{c2}$ is reached, destroys superconductivity completely [197]. Metal alloys or complex oxide ceramics are usually type-II superconductors. In addition, all high temperature superconductors are type-II superconductors as well as niobium, vanadium, and technetium.

The superconducting materials considered in this thesis, YBCO and niobium, are both type-II superconductors.

# B

# Publications

## B.1 Journal Publications

- V. A. Fedotov, A. Tsiatmas, J. H. Shi, R. Buckingham, P. de Groot, Y. Chen, S. Wang, and N. I. Zheludev. "Temperature control of Fano resonances and transmission in superconducting metamaterials". *Opt. Express*, 18:9015–9019, 2010.

- A. Tsiatmas, A. R. Buckingham, V. A. Fedotov, S. Wang, Y. Chen, P. A. J. de Groot, and N. I. Zheludev. "Superconducting plasmonics and extraordinary transmission". *Appl. Phys. Lett.*, 97:111106, 2010.
  Also selected for *Virtual Journal of Applications of Superconductivity*, 19(6), 2010.

- A. Tsiatmas, V. A. Fedotov, F. J. G. de Abajo, and N. I. Zheludev. "Low-loss terahertz superconducting plasmonics". *New J. Phys.*, 14:115006, 2012.

- A. Tsiatmas, E. Atmatzakis, N. Papasimakis, V. A. Fedotov, B. Luk'yanchuk, N. I. Zheludev, and F. J. G. de Abajo, "Optical generation of intense ultrashort magnetic pulses at the nanoscale," *arXiv:1303.6072v1*, 2013.

## B.2 Additional Publications

- V. Savinov, A. Tsiatmas, A. R. Buckingham, V. A. Fedotov, P. A. J. de Groot, and N. I. Zheludev. "Flux exclusion superconducting quantum metamaterial: towards quantum-level switching". *Sci. Rep.*, 2:450, 2012.

## B.3 Conference Contributions

- (oral) E. Atmatzakis, A. Tsiatmas, N. Papasimakis, V. A. Fedotov, B. Luk'yanchuk, F. J. G. de Abajo, and N. I. Zheludev, "Optical Excitation of Unipolar Tesla Magnetic Pulses in Plasmonic Nanostructures," *CLEO/Europe-EQEC*, Munich, Germany, 12 - 16 May 2013

- (invited) E. Atmatzakis, A. Tsiatmas, N. Papasimakis, V. A. Fedotov, B. Luk'yanchuk, F. J. G. de Abajo, and N. I. Zheludev. "Tesla Magnetic Pulses by Optical Excitation of Plasmonic Nanostructures," *IPS Meeting 2013*, Singapore, 4 - 6 Mar 2013

- (oral) E. Atmatzakis, A. Tsiatmas, N. Papasimakis, V. A. Fedotov, B. Luk'yanchuk, F. J. G. de Abajo, and N. I. Zheludev. "Generating Tesla Magnetic Pulses in Plasmonic Nanostructures," *IPS Nanometa 2013*, Seefeld, Austria, 3 - 6 Jan 2013

- (oral) V. Savinov, A. Tsiatmas, A. R. Buckingham, V. A. Fedotov, P. de Groot, and N. I. Zheludev, "Flux exclusion quantum superconducting metamaterials," *CLEO: 2012*, San Jose, USA, 6- 11 May 2012

- (poster) V. Savinov, A. Tsiatmas, A. R. Buckingham, V. A. Fedotov, P. A. J. de Groot, and N. I. Zheludev, "Flux exclusion quantum superconducting metamaterials," *SPIE Photonics Europe*, Brussels, Belgium, 16- 19 Apr 2012

- (invited) A. R. Buckingham, A. Tsiatmas, V. Savinov, V. A. Fedotov, P. A. J. de Groot, and N. I. Zheludev, "Realising tunable, quantum and low-loss metamaterials and plasmonics with superconductors," *Metamaterials 2011*, Barcelona, Spain, 10- 15 Oct 2011

- (oral) A. Tsiatmas, A. R. Buckingham, V. A. Fedotov, F. Javier Garcia de Abajo, and N. I. Zheludev, "Channeling plasmons in nanostructured superconducting waveguides," *Metamaterials 2011*, Barcelona, Spain, 10- 15 Oct 2011

- (oral) P. A. J. de Groot, A. R. Buckingham, V. Savinov, A. Tsiatmas, V. A. Fedotov, S. Wang, Y. Chen, and N. I. Zheludev, "Superconducting Metamater-

ials and Plasmonics," *Vortex Matter in Nanostructured Superconductors*, Rhodes, Greece, 10- 17 Sep 2011

- (invited) A. Tsiatmas, A. R. Buckingham, V. A. Fedotov, and N. I. Zheludev, "Superconducting Plasmonics," *SPIE Optics & Photonics 2011*, San Diego, CA, USA, 21- 25 Aug 2011

- (oral) A. Tsiatmas, V. A. Fedotov, and N. I. Zheludev, "Superconducting Analogue of Optical Plasmonic Waveguides," *CLEO/Europe - EQEC 2011*, Munich, Germany, 22- 26 May 2011

- (oral) A. Tsiatmas, V. A. Fedotov, T. Kaelberer, N. Papasimakis, V. Savinov, A. Rogacheva, D. P. Tsai, and N. I. Zheludev, "Demonstrating Elusive Toroidal Dipolar Response in Metamaterials," *CLEO/Europe - EQEC 2011*, Munich, Germany, 22- 26 May 2011

- (oral) A. Tsiatmas, A. R. Buckingham, V. Savinov, V. A. Fedotov, P. A. J. de Groot, and N. I. Zheludev, "Superconducting Plasmonics and Quantum Metamaterials," *SPP5*, Busan, S. Korea, 15- 20 May 2011

- (oral) A. Tsiatmas, A. R. Buckingham, V. A. Fedotov, P. A. J. de Groot, and N. I. Zheludev, "Superconducting Metamaterials and Extraordinary Transmission," *IONS 9*, Salamanca, Spain, 7- 9 Apr 2011

- (oral) A. R. Buckingham, A. Tsiatmas, V. A. Fedotov, Y. Chen, P. A. J. de Groot, and N. I. Zheludev, "Superconducting plasmonics and metamaterials: from extraordinary transmission to Fano resonances," *NANOMETA 2011*, Seefeld, Austria, 3- 6 Jan 2011

- (oral) A. R. Buckingham, A. Tsiatmas, V. A. Fedotov, Y. Chen, P. A. J. de Groot, and N. I. Zheludev, "Superconducting plasmonics: Extraordinary transmission and Fano resonances," *CMMP 2010*, Warwick University, UK, 14- 16 Dec 2010

- (oral) A. Tsiatmas, R. Buckingham, V. A. Fedotov, S. Wang, Y. Chen, P. A. J. de Groot, and N. I. Zheludev, [presenter: K. F. MacDonald], "Superconducting plasmonics and extraordinary transmission," *Frontiers in Optics 2010*, Rochester, NY, USA, 24- 28 Oct 2010

- (oral) A. Tsiatmas, R. Buckingham, V. A. Fedotov, S. Wang, Y. Chen, P. de Groot, and N. I. Zheludev, "Superconducting plasmonics and extraordinary transmission," *Metamaterials'2010*, Karlsruhe, Germany, 13- 16 Sep 2010

- (invited) V. A. Fedotov, J. H. Shi, A. Tsiatmas, Y. Chen, P. A. J. de Groot, and N. I. Zheludev, "High-Tc superconducting metamaterials," *SPIE Optics & Photonics*, San Diego, CA, USA, 01- 05 Aug 2010

- V. A. Fedotov, J.-H. Shi, A. Tsiatmas, P. A. J. de Groot, Y. Chen, and N. I. Zheludev, "High-Tc superconducting metamaterials," *SPIE Photonics Europe 2010*, Brussels, Belgium, 12- 16 Apr 2010

## B.4 Patents

- "Magnetic Field Generator", N. I. Zheludev, V. A. Fedotov, A. Tsiatmas, F. J. G. de Abajo, and W. J. Stewart, United States Patent Application No. 13/733,338 and United Kingdom Patent Application No. 1200186.3, 2012.

# References


[1] J. Federici and L. Moeller. "Review of terahertz and subterahertz wireless communications". *J. Appl. Phys.*, 107:111101, 2010.

[2] M. Tonouchi. "Cutting-edge terahertz technology". *Nat. Photonics*, 1:97–105, 2007.

[3] C. M. Armstrong. "The Truth About Terahertz". *IEEE Spectrum*, 49 (9):28–33, 2012.

[4] D. Graham-Rowe. "Terahertz takes to the stage". *Nat. Photonics*, 1:75–77, 2007.

[5] E. Linfield. "A source of fresh hope". *Nat. Photonics*, 1:257–258, 2007.

[6] P. Mukherjee and B. Gupta. "Terahertz (THz) Frequency Sources and Antennas - A Brief Review". *Int. J. Infrared Milli Waves*, 29:1091–1102, 2008.

[7] K. Wang and D. M. Mittleman. "Metal wires for terahertz waveguiding". *Nature*, 432:376–379, 2004.

[8] H. Pahlevanninezhad, B. Heshmat, and T. E. Darcie. "Advances in Terahertz Waveguides and Sources". *IEEE Phot. J.*, 3 (2):307–310, 2011.

[9] M. Born and E. Wolf. *Principles of Optics*. Cambridge University Press, 1997.

[10] L. Jofre, J. Romeu, S. Capdevila, J. Abril, E. Nova, and M. Alosnso. "The "challenging" world of Terahertz radiation and imaging". *Proceedings of the 5th*

*European Conference on Antennas and Propagation (EUCAP)*, pages 3470–3475, 2011.

[11] P. Siegel, P. de Maagt, and A. Zaghloul. "Antennas for terahertz applications". *IEEE Antennas and Propagation Society International Symposium 2006*, pages 2383–2386, 2006.

[12] H. I. Libon, S. Baumgartner, M. Hempel, N. E. Hecker, J. Feldmann, M. Koch, and P. Dawson. "An optically controllable terahertz filter". *Appl. Phys. Lett.*, 76:2821, 2000.

[13] T. Kleine-Ostmann, P. Dawson, K. Pierz, G. Hein, and M. Koch. "Room-temperature operation of an electrically driven terahertz modulator". *Appl. Phys. Lett.*, 84:3555, 2004.

[14] M. Unlu, C. W. Berry, S. Li, S.-H. Yang, M. R. Hashemi, and M. Jarahhi. "Broadband Terahertz Modulators based on MEMS-Reconfigurable Mesh Filters". *arXiv:1212.6562v1*, 2012.

[15] S. Choi and K. Sarabandi. "Performance assessment of bundled carbon nanotubes for antenna applications at terahertz frequencies and higher". *IEEE Trans. Antennas Propag.*, 59 (3):802–809, 2011.

[16] B. Sensale-Rodriguez, R. Yan, M. M. Kelly, T. Fang, K. Tahy, W. S. Hwang, D. Jena, L. Liu, and H. G. Xing. "Broadband graphene terahertz modulators enabled by intraband transitions". *Nat. Communications*, 3:780, 2012.

[17] S. H. Lee, M. Choi, T.-T. Kim, S. Lee, M. Liu, X. Yin, H. K. Choi, S. S. Lee, C.-G. Choi, S.-Y. Choi, X. Zhang, and B. Min. "Switching terahertz waves with gate-controlled active graphene metamaterials". *Nat. Materials*, 11:936–941, 2012.

[18] N. I. Zheludev. "The Road Ahead for Metamaterials". *Science*, 328:582–583, 2010.

[19] W. Withayachumnankul and D. Abbott. "Metamaterials in the Terahertz Regime". *IEEE Phot. Journal*, 1 (2):99–118, 2009.

[20] H.-T. Chen, W. J. Padilla, R. D. Averitt, A. C. Gossard, C. Highstrete, M. Lee, J. F. O'Hara, and A. J. Taylor. "Electromagnetic Metamaterials for Terahertz Applications". *Terahertz Science and Technology*, 1 (1):42–50, 2008.

[21] H.-T. Chen, W. J. Padilla, M. J. Cich, A. K. Azad, R. D. Averitt, and A. J. Taylor. "A metamaterial solid-state terahertz phase modulator". *Nat. Photonics*, 3:148–151, 2009.

[22] T. J. Yen, W. J. Padilla, N. Fang, D. C. Vier, D. R. Smith, J. B. Pendry, D. N. Basov, and X. Zhang. "Terahertz magnetic response from artificial materials". *Science*, 303:1494–1496, 2004.

[23] W. J. Padilla, M. T. Aronsson, C. Highstrete, M. Lee, A. J. Taylor, and R. D. Averitt. "Electrically resonant terahertz metamaterials: Theoretical and experimental investigations". *Phys. Rev. B*, 75:041102:1–4, 2007.

[24] T. F. Gundogdu, I. Tsiapa, A. Kostopoulos, N. Konstantinidis, R. S. Penciu, M. Kafesaki, E. N. Economou, T. Koschny, and C. M. Soukoulis. "Experimental demonstration of negative magnetic permeability in the far-infrared frequency regime". *Appl. Phys. Lett.*, 89:084103, 2006.

[25] H. O. Moser, B. D. F. Casse, O. Wilhelmi, and B. T. Saw. "Terahertz response of a microfabricated rod splitring resonator electromagnetic metamaterial". *Appl. Phys. Lett.*, 94:063901, 2005.

[26] H. T. Chen, J. F. O'Hara, A. K. Azad, A. J. Taylor, R. D. Averitt, D. B. Shrekenhamer, and W. J. Padilla. "Experimental demonstration of frequency-agile terahertz metamaterials". *Nat. Photonics*, 2:295–298, 2008.

[27] C. Rockstuhl and W. Zhang. "Terahertz phase modulator". *Nat. Photonics*, 3:130–131, 2009.

[28] J. Gu, R. Singh, X. Zhang, S. A. Maier, Z. Tian, A. K. Azad, H. T. Chen, A. J. Taylor, J. Han, and W. Zhang. "Active control of electromagnetically induced transparency analogue in terahertz metamaterials". *Nat. Communications*, 3, 2012.

[29] H. Tao, A. C. Strikwerda, K. Fan, W. J. Padilla, X. Zhang, and R. D. Averitt. "MEMS Based Structurally Tunable Metamaterials at Terahertz Frequencies". *J. Infrared Milli Terahz Waves*, 32 (5):580–595, 2011.

[30] D. Wu, N. Fang, C. Sun, X. Zhang, W. J. Padilla, D. N. Basov, D. R. Smith, and S. Schultz. "Terahertz plasmonic high pass filter". *Appl. Phys. Lett.*, 83:201–203, 2003.

[31] H. Tao, N. I. Landy, C. M. Bingham, X. Zhang, R. D. Averitt, and W. J. Padilla. "A metamaterial absorber for the terahertz regime: Design, fabrication and characterization". *Opt. Express*, 16:7181–7188, 2008.

[32] P. Tassin, T. Koschny, M. Kafesaki, and C. M. Soukoulis. "A comparison of graphene, superconductors and metals as conductors for metamaterials and plasmonics". *Nat. Photonics*, 6:259–264, 2012.

[33] B. Bowden, J. A. Harrington, and O. Mitrofanov. "Fabrication of terahertz hollow-glass metallic waveguides with inner dielectric coatings". *J. Appl. Phys.*, 104:093110, 2008.

[34] J.-K. Lu, C.-P. Yu, H.-C. Chang, H.-W. Chen, and Y.-T. Li. "Terahertz air-core microstructure fiber". *Appl. Phys. Lett.*, 92:064105, 2008.

[35] R. Mendis and D. Grischkowsky. "Undistorded guided-wave propagation of subpicosecond terahertz pulses". *Opt. Lett.*, 26:846–848, 2001.

[36] S. Maier, S. Andrews, L. Martin-Moreno, and F. J. Garcia-Vidal. "Terahertz Surface Plasmon-Polariton Propagation and Focusing on Periodically Corrugated Metal Wires". *Phys. Rev. Lett.*, 97:176805, 2006.

[37] S. A. Maier. *Plasmonics: Fundamentals and Applications.* Springer, 2006.

[38] M. L. Brongersma and V. M. Shalaev. "The Case for Plasmonics". *Science*, 328:440–441, 2010.

[39] H. Raether. *Surface Plasmons on Smooth and Rough Surfaces and on Gratings.* Springer, 1988.

[40] D. K. Gramotnev and S. I. Bozhevolnyi. "Plasmonics beyond the diffraction limit". *Nat. Photonics*, 4:83–91, 2010.

[41] J. B. Pendry. "Mimicking Surface Plasmons with Structured Surfaces". *Science*, 305:847–848, 2004.

[42] R. E. Collin. *Field Theory of Guided Waves*. McGraw Hill, New York, 1960.

[43] R. Ulrich and M. Tacke. "Submillimeter waveguiding on periodic metal structure". *Appl. Phys. Lett.*, 22:251–253, 1973.

[44] D. Martin-Cano, O. Quevedo-Teruel, E. Moreno, L. Martin-Moreno, and F. J. Garcia-Vidal. "Waveguided spoof surface plasmons with deep-subwavelength lateral confinement". *Opt. Lett.*, 36:4635–4637, 2011.

[45] M. B. Johnston. "Superfocusing of terahertz waves". *Nat. Photonics*, 1:14–15, 2007.

[46] D. Saeedkia and S. Sefavi-Naeini. "Terahertz Photonics: Optoelectronic Techniques for Generation and Detection of Terahertz Waves". *J. Lightwave Tech.*, 26 (15):2409–2423, 2008.

[47] D. Mittleman. *Sensing with Terahertz Radiation*. Springer, 2003.

[48] I. Hosako, N. Sekine, M. Patrashin, S. Saito, K. Fukunaga, Y. Kasai, P. Baron, T. Seta, J. Mendrok, S. Ochiai, and H. Yasuda. "At the dawn of a new era in terahertz technology". *Proc. IEEE*, 95 (8):1611–1623, 2007.

[49] C. Jastrow, K. Munter, R. Piesiewicz, T. Kurner, M. Koch, and T. Kleine-Ostman. "300 Ghz transmission system". *Electron. Lett.*, 44 (3):213–214, 2008.

[50] B. S. Williams. "Terahertz quantum-cascade lasers". *Nat. Photonics*, 1:517–525, 2007.

[51] M. S. Vitiello and A. Tredicucci. "Tunable Emission in THz Quantum Cascade Lasers". *IEEE Trans. on THz Sc. and Technol.*, 1:76–84, 2011.

[52] I. Tudosa, C. Stamm, A. B. Kashuba, F. King, H. C. Siegmann, J. Stohr, G. Ju, B. Lu, and D. Weller. "The ultimate speed of magnetic switching in granular recording media". *Nature*, 428:831, 2004.

[53] W. M. Magie. *A Source Book in Physics*. Harvard: Cambridge MA, 1963.

[54] S. Chrouch and D. A. Skoog. *Principles of instrumental analysis*. Thomson Brooks: Australia, 2007.

[55] D. Pozar. *Microwave Engineering*. John Wiley: New York, 2005.

[56] H. T. Friis. "A note on a simple transmission formula". *Proc. IRE*, 34:254, 1946.

[57] C. A. Balanis. *Antenna Theory: Analysis and Design*. Wiley-Interscience, 2005.

[58] AN 1287-3 Agilent. *Applying Error Correction to Network Analyzer Measurements*. Agilent, 2003.

[59] N. Papasimakis. *Trapped-modes, Slow Light and Collective Resonances in Metamaterials*. University of Southampton: PhD Thesis, 2009.

[60] D. Brewster. "On the laws which regulate the polarisation of light by reflection from transparent bodies". *Phil. Trans. Royal Soc. of London*, 105:125–159, 1815.

[61] A. Ern and J. L. Guermond. *Theory and practice of finite elements*. Springer, 2004.

[62] J. J. Leader. *Numerical Analysis and Scientific Computation*. Addison Wesley, 2004.

[63] R. Courant. "Variational methods for the solution of problems of equilibrium and vibrations". *Bulletin of the American Mathematical Society*, 1943.

[64] R. W. Clough. *The Finite Element Method in Plane Stress Analysis*. American Society of Civil Engineers, 1960.

[65] D. Davidson. *Computational Electromagnetics for RF and Microwave Engineering*. Cambridge University Press, 2005.

[66] J. Jin and D. J. Riley. *Finite Element Analysis of Antennas and Arrays*. John Wiley: New Jersey, 2009.

[67] W. T. Padgett, D. V. Anderson, and J. Moura. *Fixed-Point Signal Processing*. Morgan and Claypool Publishers, 2009.

[68] J. W. Coburn and N. R. Whetten. *Plasma etching and reactive ion etching.* American Institute of Physics, 1982.

[69] *www.zemetrics.com.*

[70] S. D. Jenkins and J. Ruostekoski. "Collective electromagnetic response of discrete metamaterial systems". arXiv:1012.3928, 2010.

[71] S. D. Jenkins and J. Ruostekoski. "Controlled manipulation of light by cooperative response of atoms in an optical lattice". *Phys. Rev. A.*, 86:031602 (R), 2012.

[72] M. Lapine, I. Shadrivov, and Y. Kivshar. "Wide-band negative permeability of nonlinear metamaterials". *Sci. Rep.*, 2:412, 2012.

[73] E. Yablonovitch. "Inhibited Spontaneous Emission in Solid-State Physics and Electronics". *Phys. Rev. Lett.*, 58:2059–2062, 1987.

[74] B. A. Munk. *Frequency Selective Surfaces: Theory and Design.* John Wiley & Sons, 2005.

[75] J. Brown. "Artificial dielectrics having refractive indices less than unity". *Proc. IEE*, 100:51, 1953.

[76] W. Rotman. "Plasma simulation by artificial dielectric and parallel-plate media". *IRE Transactions on Antennas and Propagation*, 10:82, 1962.

[77] J. B. Pendry, A. J. Holden, D. J. Robbins, and W. J. Stewart. "Magnetism from conductors and enhanced nonlinear phenomena". *IEEE Trans. on Microw. Theory and Techn.*, 47:2075–2084, 1999.

[78] W. N. Hardy and L. A. Whitehead. "Split-ring resonator for use in magnetic resonance from 200-2000 MHz". *Rev. Sci. Instrum.*, 52:213, 1981.

[79] D. R. Smith, J. B. Pendry, and M. C. K. Wiltshire. "Metamaterials and Negative Refractive Index". *Science*, 305:788–792, 2004.

[80] D. R. Smith, W. J. Padilla, D. C. Vier, S. C. Nemat-Nasser, and S. Schultz. "Composite Medium with Simultaneously Negative Permeability and Permittivity". *Phys. Rev. Lett.*, 84:4184, 2000.

[81] V. G. Veselago. "The Electrodynamics of Substances with Simultaneously Negative Values of $\varepsilon$ and $\mu$". *Sov. Phys. Uspekhi*, 10:509, 1968.

[82] R. A. Shelby, D. R. Smith, and S. Schultz. "Experimental Verification of a Negative Index of Refraction". *Science*, 292:77–79, 2001.

[83] J. B. Pendry. "Negative Rerfraction Makes a Perfect Lens". *Phys. Rev. Lett.*, 85:3966–3969, 2000.

[84] J. B. Pendry, D. Schurig, and D. R. Smith. "Controlling Electromagnetic Fields". *Science*, 312:1780–1782, 2006.

[85] U. Leonhardt. "Optical conformal mapping". *Science*, 312:1777, 2006.

[86] D. Schurig, J. J. Mock, B. J. Justice, S. A. Cummer, J. B. Pendry, A. F. Starr, and D. R. Smith. "Metamaterial electromagnetic cloak at microwave frequencies". *Science*, 314:977, 2006.

[87] N. Fang, H. Lee, C. Sun, and X. Zhang. "Experimental Verification of a Negative Index of Refraction". *Science*, 308:534–537, 2005.

[88] T. Ergin, N. Stenger, P. Brenner, J. B. Pendry, and M. Wegener. "Three-Dimensional Invisibility Cloak at Optical Wavelengths". *Science*, 328:337–339, 2010.

[89] A. E. Nikolaenko, F. De Angelis, S. A. Boden, N. Papasimakis, P. Ashburn, E. Di Fabrizio, and N. I. Zheludev. "Carbon Nanotubes in a Photonic Metamaterial". *Phys. Rev. Lett.*, 104:153902, 2010.

[90] A. E. Nikolaenko, N. Papasimakis, E. Atmatzakis, Z. Luo, Z. Shen Xiang, F. De Angelis, S. A. Boden, E. Di Fabrizio, and N. I. Zheludev. "Nonlinear graphene metamaterial". *Appl. Phys. Lett.*, 100:181109, 2012.

[91] Z. L. Samsón, K. F. Macdonald, F. De Angelis, B. Gholipour, K. Knight, C.-C. Huang, E. Di Fabrizio, D. W. Hewak, and N. I. Zheludev. "Metamaterial electro-optic switch of nanoscale thickness". *Appl. Phys. Lett.*, 96:143105, 2010.

[92] J. Y. Ou, E. Plum, L. Jiang, and N. I. Zheludev. "Reconfigurable photonic metamaterials". *Nano Lett.*, 11 (5):2142–2144, 2011.

[93] G. Dolling, C. Enkrich, M. Wegener, J. F. Zhou, C. M. Soukoulis, and Linden S. "Cut-wire pairs and plate pairs as magnetic atoms for optical metamaterials". *Opt. Lett.*, 30:3198–3200, 2005.

[94] J. Valentine, S. Zhang, T. Zentgraf, E. Ulin-Avila, D. A. Genov, G. Bartal, and Z. Zhang. "Three-dimensional optical metamaterial with a negative refractive index". *Nature*, 455:376–379, 2008.

[95] N. Papasimakis, V. A. Fedotov, Y. H. Fu, D. P. Tsai, and N. I. Zheludev. "Coherent and incoherent metamaterials and order-disorder transitions". *Phys. Rev. B*, 80:041102(R), 2009.

[96] V. A. Fedotov, M. Rose, S. L. Prosvirnin, N. Papasimakis, and N. I. Zheludev. "Sharp trapped-mode resonances in planar metamaterials with a broken structural symmetry". *Phys. Rev. Lett.*, 99:147401, 2007.

[97] S. Prosvirnin and S. Zouhdi. "Resonances of Closed Modes in Thin Arrays of Complex Particles". *Adv. in Electr. of Complex Media and Metamaterials*, 89:281–290, 2002.

[98] A. E. Miroshnichenko, S. Flach, and Y. S. Kivshar. "Fano resonances in nanoscale structures". *Rev. Mod. Phys.*, 82:2257–2298, 2010.

[99] B. Lukýanchuk, N. I. Zheludev, S. A. Maier, N. J. Halas, P. Nordlander, H. Giessen, and C. T. Chong. "The Fano resonance in plasmonic nanostructures and metamaterials". *Nat. Materials*, 9:707–715, 2010.

[100] N. Papasimakis and N. I. Zheludev. "Metamaterial Induced Transparency". *Optics and Photonics News*, 20 *(10)*:22, 2009.

[101] D. O. Guney, T. Koschny, and C. M. Soukoulis. "Reducing ohmic losses in metamaterials by geometric tailoring". *Phys. Rev. B*, 80:125129, 2009.

[102] E. Plum, V. A. Fedotov, P. Kuo, D. P. Tsai, and N. I. Zheludev. "Towards the lasing spaser: controlling metamaterial optical response with semiconductor quantum dots". *Opt. Express*, 17:8548–8551, 2009.

[103] J. B Khurgin and G. Sun. "In search of the elusive lossless metal". *Appl. Phys. Lett.*, 96:1–4, 2010.

[104] R. Singh, T. Zhen, H. Jianguang, C. Rockstuhl, G. Jianqiang, and Z. Weili. "Cryogenic temperatures as a path towards high-Q terahertz metamaterials". *Appl. Phys. Lett.*, 96:071114, 2010.

[105] M. Lapine, D. A. Powell, M. V. Gorkunov, I. V. Sharidov, R. Marques, and Y. S. Kivshar. "Structural tunability in metamaterials". *Appl. Phys. Lett.*, 95:084105, 2009.

[106] J. Ou, E. Plum, and N. I. Zheludev. "MHz bandwidth electro-optical modulator based on a reconfigurable photonic metamaterial". *CLEO, San Jose, United States*, 2012.

[107] I. Murina, V. Turgaliev, and I. Vendik. "Tunable terahertz metamaterials based on electrically controlled piezoelectric actuators". *Tech. Phys. Lett.*, 38 (6):579, 2012.

[108] O. Buchnev, J. Y. Ou, M. Kaczmarek, N. I. Zheludev, and V. A. Fedotov. "Electro-optical control in a plasmonic metamaterial hybridised with a liquid-crystal cell". *Opt. Express*, 21 (2):1633–1638, 2013.

[109] I. V. Shadrivov, A. B. Kozyrev, D. W. van der Weide, and Y. S. Kivshar. "Nonlinear magnetic metamaterials". *Opt. Express*, 16:20266–20271, 2008.

[110] M. Ricci, N. Orloff, and S. M. Anlage. "Superconducting Metamaterials". *Appl. Phys. Lett.*, 87:034102, 2005.

[111] M. C. Ricci, H. Xu, R. Prozorov, A. P. Zhuravel, A. V. Ustinov, and S. M. Anlage. "Tunability of Superconducting Metamaterials". *IEEE Trans. on Appl. Supercon.*, 17:918–921, 2007.

[112] R. Singh, J. Xiong, A. K. Azad, H. Yang, S. A. Trugman, Q. X. Jia, A. J. Taylor, and H.-T. Chen. "Optical tuning and ultrafast dyanmics of high-temperature superconducting terahertz metamaterials". *Nanophotonics*, 1:117–123, 2012.

[113] V. Savinov, V. A. Fedotov, S. M. Anlage, P. A. J. de Groot, and N. I. Zheludev. "Modulating sub-THz radiation with current in superconducting metamaterial". *Phys. Rev. Lett.*, 109:243904, 2012.

[114] D. E. Oates, M. A. Hein, P. J. Hirst, R. G. Humphreys, G. Koren, and E. Polturak. "Nonlinear microwave surface impedance of YBCO films: latest results and present understanding". *Physica C*, 372:462–468, 2002.

[115] N. Klein. "High-frequency applications of high-temperature superconductor thin films". *Rep. Prog. Phys.*, 65:1387–1425, 2002.

[116] N. Lazarides and G. P. Tsironis. "RF supercoducting quantum interference device metamaterials". *Appl. Phys. Lett.*, 90:163501, 2007.

[117] P. Jung, S. Butz, V. Shitov, and A. V. Ustinov. "Low-loss tunable metamaterials using superconducting circuits with Josephson junctions". *Appl. Phys. Lett.*, 102:062601, 2013.

[118] V. A. Fedotov, A. Tsiatmas, J. H. Shi, R. Buckingham, P. de Groot, Y. Chen, S. Wang, and N. I. Zheludev. "Temperature control of Fano resonances and transmission in superconducting metamaterials". *Opt. Express*, 18:9015–9019, 2010.

[119] A. Tsiatmas, A. R. Buckingham, V. A. Fedotov, S. Wang, Y. Chen, P. A. J. de Groot, and N. I. Zheludev. "Superconducting plasmonics and extraordinary transmission". *Appl. Phys. Lett.*, 97:111106, 2010.

[120] V. Savinov, A. Tsiatmas, A. R. Buckingham, V. A. Fedotov, P. A. J. de Groot, and N. I. Zheludev. "Flux exclusion superconducting quantum metamaterial: towards quantum-level switching". *Sci. Rep.*, 2:450, 2012.

[121] J. Gu, R. Singh, Z. Tian, W. Cao, Q. Xing, M. He, J. W. Zhang, J. Han, H. T. Chen, and W. Zhang. "Terahertz superconductor metamaterial". *Appl. Phys. Lett.*, 97:071102, 2010.

[122] Z. Tin, R. Singh, J. Han, J. Gu, Q. Xing, J. Wu, and W. Zhang. "Terahertz superconducting plasmonic hole array". *Opt. Lett.*, 35:3586–3588, 2010.

[123] N. Papasimakis, V. A. Fedotov, N. I. Zheludev, and S. L. Prosvirnin. "Metamaterial Analog of electromagnetically induced transparency". *Phys. Rev. Lett.*, 101:253903, 2008.

[124] S. Zhang, D. A. Genov, Y. Wang, M. Liu, and X. Zhang. "Plasmon-induced transparency in metamaterials". *Phys. Rev. Lett.*, 101 (4):047401, 2008.

[125] B. Lahiri, A. Z. Khokhar, R. M. De La Rue, S. G. McMeekin, and N. P. Johnson. "Asymmetric split ring resonators for optical sensing of organic materials". *Opt. Express*, 17 (2):1107–1115, 2009.

[126] F. Gao, Kruse J. W., C. E. Platt, M. Feng, and M. V. Klein. "Microwave surface impedance at 10GHz and quasiparticle scattering in $YBa_2Cu_3O_7$ films". *Appl. Phys. Lett.*, 63:2274–2276, 1993.

[127] *www.theva.com.*

[128] V.A. Fedotov, N. Papasimakis, E. Plum, A. Bitzer, M. Walther, P. Kuo, D. P. Tsai, and N. I. Zheludev. "Spectral collapse in ensembles of metamolecules". *Phys. Rev. Lett.*, 104:223901, 2010.

[129] H. A. Bethe. "Theory of diffraction by Small Holes". *Phys. Rev.*, 66:163, 1944.

[130] T. W. Ebbesen, H. J. Lezec, H. F. Ghaemi, T. Thio, and P. A. Wolff. "Extraordinary optical transmission through sub-wavelength hole arrays". *Nature*, 391:667–669, 1998.

[131] L. Martin-Moreno, F. J. Garcia-Vidal, H. J. Lezec, K. M. Pellerin, T. Thio, J. B. Pendry, and T. W. Ebbesen. "Theory of Extraordinary Optical Transmission through Subwavelength Hole Arrays". *Phys. Rev. Lett.*, 86:1114, 2001.

[132] M. Sun, J. Tian, Z.-Y. Li, B.-Y. Cheng, D.-Z. Zhang, A.-Z. Jin, and H.-F. Yang. "The Role of Periodicity in Enhanced Transmission through Subwavelenght Hole Arrays". *Chin. Phys. Lett.*, 23:486, 2006.

[133] F. Przybilla, C. Genet, and T. W. Ebbesen. "Enhanced transmission through Penrose subwavelength hole arrays". *Appl. Phys. Lett.*, 89:121115, 2006.

[134] N. Papasimakis, V. A. Fedotov, A. S. Schwanecke, F. J. Garcia de Abajo, and N. I. Zheludev. "Enhanced microwave transmission through quasicrystal hole arrays". *Appl. Phys. Lett.*, 91:081503, 2007.

[135] H. F. Ghaemi, T. Thio, D. E. Grupp, T. W. Ebbesen, and H. J. Lezec. "Surface plasmons enhance optical transmission through subwavelength holes". *Phys. Rev. B*, 58:6779, 1998.

[136] M. M. J. Treacy. "Dynamical diffraction in metallic optical gratings". *Appl. Phys. Lett.*, 75:606, 1999.

[137] H. E. Went, A. P. Hibbins, J. R. Sambles, C. R. Lawrence, and A. P. Crick. "Selective transmission through very deep zero- order metallic gratings at microwave frequencies". *Appl. Phys. Lett.*, 77:2789, 2000.

[138] F. J. G. de Abajo and J. J. Saenz. "Electromagnetic Surface Modes in Structured Perfect-Conductor Surfaces". *Phys. Rev. Lett.*, 95:233901:254, 2005.

[139] S. Riikonen, I. Romero, and F. J. Garcia de Abajo. "Plasmon tunability in metallodielectric metamaterials". *Phys. Rev. B*, 71:235104, 2005.

[140] M. Staffaroni, E. Yablonovitch, and J. Conway. "Metal Optics as a Circuit Problem: Reaviling the Possibility of an Optical Voltage Transformer". *Conference on Lasers and Electro-Optics (CLEO) 2010 CFB, CFB6*, 2010.

[141] C. Du, H. Chen, and S. Li. "Stable and bistable SQUID metamaterials". *J. Phys. Condens. Matter*, 20:345220, 2008.

[142] T. Van Duzer and C. W. Turner. *Principles of Superconductive Devices and Circuits*. Edward Arnold (Publishers), 1981.

[143] S. A. Maier, P. G. Kik, H. A. Atwater, S. Meltzer, E. Harel, B. E. Koel, and A. G. Requicha. "Local detection of electromagnetic energy transport below the diffraction limit in metal nanoparticle plasmon waveguides". *Nat. Materials*, 2:229–232, 2003.

[144] L. Wendler and R. Haupt. "Long-range surface plasmon-polaritons in asymmetric layer structures". *J. Appl. Phys.*, 59:3289–3291, 1986.

[145] P. Drude. "Zur Elektronentheorie der metalle". *Annalen der Physik*, 306:566, 1900.

[146] J. N. Israelachivili. *Intermolecular and Surface Forces*. New York: Academic, 1992.

[147] J. Takahara, S. Yamagishi, H. Taki, A. Morimoto, and T. Kobayashi. "Guiding of a one-dimensional optical beam with nanometer diameter". *Opt. Lett.*, 22:475–477, 1997.

[148] E. Moreno, F. J. Garcia-Vidal, S. G. Rodrigo, L. Martin-Moreno, and S. I. Bozhevolnyi. "Channel plasmon-polaritons: Modal shape, dispersion, and losses". *Opt. Lett.*, 31:3447–3449, 2006.

[149] R. F. Oulton, V. J. Sorger, D. A. Genov, D. F. P. Pile, and X. Zhang. "A hybrid plasmonic waveguide for subwalength confinement and long-range propagation". *Nat. Photonics*, 2:496–500, 2008.

[150] K. V. Nerkararyan. "Superfocusing of a surface polariton in a wedge-like structure". *Phys. Lett. A*, 237:103–105, 1997.

[151] S. I Bozhevolnyi, V. S Volkov, E. Devaux, J. Y. Laluet, and T. W. Ebbesen. "Channel plasmon subwavelenght waveguide components including interferometers and ring resonators". *Nature*, 440:508–511, 2006.

[152] V. S. Volkov, S. I. Bozhevolnyi, E. Devaux, J.-Y. Laluet, and T. W. Ebbesen. "Wavelength selective nanophotonic components utilizing channel plasmon polaritons". *Nano Lett.*, 7:880–884, 2007.

[153] A. Rusina, M. Durach, and M. I. Stockman. "Theory of spoof plasmons in real metals". *Appl. Phys. A*, 100:375–378, 2010.

[154] C. Soukoulis and M. Wegener. "Optical Metamaterials-More Bulky and Less Lossy". *Science*, 330:1633, 2010.

[155] I. De Leon and P. Berini. "Amplification of long-range surface plasmons by a dipolar gain medium". *Nat. Photonics*, 4:382–387, 2010.

[156] A. Boltasseva and H. A. Atwater. "Low-Loss Plasmonic Metamaterials". *Science*, 331:290, 2010.

[157] A. A. Fedotov, T. Uchino, and J. Y. Ou. "Low-loss plasmonic metamaterial based on epitaxial gold monocrystal film". *Opt. Express*, 20 (9):9545, 2010.

[158] K. F. MacDonald, Z. L. Samsón, M. I. Stockman, and N. I. Zheludev. "Ultrafast active plasmonics". *Nat. Photon.*, 3:55–58, 2009.

[159] D. Pacifici, H. J. Lezec, and H. A. Atwater. "All-optical modulation by plasmonic excitation of CdSe quantum dots". *Nat. Photonics*, 1:402–406, 2007.

[160] A. L. Falk, H. L. Koppens, C. L. Yu, K. Kang, N. de Leon Snapp, A. V. Akimov, M.-H. Jo, M. D. Lukin, and H. Park. "Near-field electrical detection of optical plasmons and single-plasmons sources". *Nat. Physics*, 5:475–479, 2009.

[161] A. Tsiatmas, V. A. Fedotov, F. J. G. de Abajo, and N. I. Zheludev. "Low-loss terahertz superconducting plasmonics". *New J. Phys.*, 14:115006, 2012.

[162] J. E. Mooij and G. Schon. "Propagating plasma mode in thin superconducting filaments". *Phys. Rev. Lett.*, 55:114–117, 1985.

[163] H. A. Fertig and S. Das Sarma. "Collective modes in layered superconductors". *Phys. Rev. Lett.*, 65:1482–1485, 1990.

[164] V. A. Golick, D. V. Kadygrob, V. A. Yampol'skii, A. L. Rakhmanov, B. A. Ivanov, and F. Norri. "Surface Josephson Plasma Waves in Layered Superconductors above the Plasma Frequency: Evidence for a Negative Index of Refraction". *Phys. Rev. Lett.*, 104:187003, 2010.

[165] J. S. Swihart. "Field-Solution for a Thin-Film Superconducting Strip Transmission Line". *J. Appl. Phys.*, 32:461–469, 1961.

[166] O. Buisson, P. Xavier, and J. Richard. "Observation of Propagating Plasma Modes in a Thin Superconducting Film". *Phys. Rev. Lett.*, 73:3153–3156, 1994.

[167] S.-O. Katterwe, H. Motzkau, A. Rydh, and V. M. Krasnov. "Observation of polaritons in Bi2Sr2CaCu2O8+x single crystals". *arXiv:1010.6172*, 2010.

[168] J. Bardeen, L. N. Cooper, and J. R. Schrieffer. "Theory of superconductivity". *Phys. Rev. B*, 108:162–164, 1957.

[169] A. H. Majedi. "Theoretical Investigations on THz and Optical Superconductive Surface Plasmon Interface". *IEEE Trans. Appl. Supercond.*, 19:907–910, 2009.

[170] A. S. Mosquera, D. A. Landinez Tellez, and J. Roa-Rojas. "Application of a phenomenological model for the surface impedance in high temperature superconducting films". *Phys. Stat. Sol. C*, 4 (11):4298–4305, 2007.

[171] R. D. Kekatpure, A. C. Hryciw, E. S. Barnard, and M. L. Brongersma. "Solving dielectric and plasmonic waveguide dispersion relations on a pocket calculator". *Opt. Express*, 17:24112–24119, 2009.

[172] K. F. MacDonald and N. I. Zheludev. "Active Pasmonics: current status". *Laser Photon. Rev.*, 4 (4):562–567, 2010.

[173] R. W. McGowan, G. Gallot, and D. Grischkowsky. "Propagation of ultrawideband short pulses of terahertz radiation through submillimeter-diameter circular waveguides". *Opt. Lett.*, 24 (20):1431–1433, 1999.

[174] T. Akalin, A. Treizebre, and B. Bocquet. "Single-wire transmission lines at terahertz frequencies". *IEEE Trans. Microw. Theory Tech.*, 54 (6):2762–2767, 2006.

[175] E. D. Palik. *Handbook of Optical Constants of Solids vol 3*. New York: Academic, 1998.

[176] L. Ju, B. Geng, J. Horng, C. Girit, M. Martin, Z. Hao, H. A. Bechtel, X. Liang, A. Zettl, Y. R. Shen, and F. Wang. "Graphene plasmonics for tunable terahertz metamaterials". *Nat. Nanotechnology*, 6:630–634, 2011.

[177] M. Jablan, H. Buljan, and M. Soljacic. "Plasmonics in graphene at infrared frequencies". *Phys. Rev. B*, 80:245435, 2009.

[178] Z. Lin, L. V. Zhigilei, and V. Celli. "Electron-phonon coupling and electron heat capacity of metals under conditions of strong electron-phonon nonequilibrium". *Phys. Rev. B*, 77:075133, 2008.

[179] J. Huang, Y. Zhang, and J. K. Chen. "Ultrafast solid liquid vapor phase change of a gold film induced by pico- to femtosecond lasers". *Appl. Phys. A*, 95:643, 2009.

[180] D. R. Lide. *CRC Handbook Chemistry and Physics*. CRC Press: Boca Raton, FL, 2005.

[181] N. W. Aschroft and N. D. Mermin. *Solid State Physics*. Harcourt College Publishers: New York, 1976.

[182] J. K. Chen, W. P. Latham, and J. E. Bearaun. "The role of electronphonon coupling in ultrafast laser heating". *J. Laser Appl.*, 17:63, 2005.

[183] D. S Ivanov and L. V. Zhigilei. "Combined atomistic-continuum modeling of short-pulse laser melting and disintegration of metal films". *Phys. Rev. B*, 68:064114, 2003.

[184] P. E. Hopkins, M. L. Bauer, J. C. Duda, J. L. Smoyer, T. S. English, P. M. Norris, T. E. Beechem, and D. A. Stewart. "Ultrafast thermoelectric properties of gold under conditions of strong electron-phonon nonequilibrium". *J. Appl. Phys.*, 108:104907, 2010.

[185] J. D. Jackson. *Classical Electrodynamics*. Wiley: New York, 1999.

[186] S. Karim, K. Maaz, G. Ali, and W. Ensinger. "Diameter dependent failure current density of gold nanowires". *J. Phys. D*, 42:185403, 2009.

[187] H. Yao, J. Duan, D. Mo, H. Y. Gunel, Y. Chen, J. Liu, and T. Schapers. "Optical and electrical properties of gold nanowires synthesized by electrochemical deposition". *J. Appl. Phys.*, 110:094301, 2011.

[188] S. Inasawa, M. Sugiyama, and Y. Yamaguchi. "Laser-Induced Shape Transformation of Gold Nanoparticles below the Melting Point: The Effect of Surface Melting". *J. Phys. Chem. B*, 109:3104, 2005.

[189] D. Y. Petrovykh, K. N. Altmann, H. Hochst, M. Laubscher, S. Maat, G. J. Mankey, and F. J. Himpsel. "Spin-dependent band structure, Fermi surface, and carrier lifetime of permalloy". *Appl. Phys. Lett.*, 73:3459, 1998.

[190] C. Kittel. *Introduction to Solid State Physics*. Wiley, 2004.

[191] W. Meissner and R. Ochsenfeld. "Ein neuer Effekt bei Eintritt der Supraleitfahigkeit". *Naturwissenschaften*, 21 (44):787–788, 1933.

[192] F. London and H. London. "The Electromagnetic Equations of the Superconductor". *Proc. Roy. Soc. (London)*, A149:77, 1935.

[193] L. Cooper. "Bound electron pairs in a degenerate Fermi gas". *Phys. Rev.*, 104 (4):1189–1190, 1956.

[194] B. D. Josephson. "Possible new effects in superconductive tunneling". *Phys. Lett.*, 1:251, 1962.

[195] P. W. Anderson and J. M. Rowell. "Probable Observation of the Josephson Tunnel Effect". *Phys. Rev. Lett.*, 10:230, 1963.

[196] M. K. Wu, J. R. Ashburn, C. J. Torng, P. H. Hor, R. L. Meng, L. Gao, Z. J. Huang, Y. Q. Wang, and C. W. Chu. "Superconductivity at 93K in a New Mixed-Phase Y-Ba-Cu-O Compound System at Ambient Pressure". *Phys. Rev. Lett.*, 58 (9):908–910, 1987.

[197] M. Tinkham. *Introduction to Superconductivity*. Dover, 1996.

[198] C. J. Gorter and H. B. G. Casimir. *Phys. Z*, 35:963, 1934.